universität wien

DISSERTATION | DOCTORAL THESIS

Titel | Title

Machine-Learned Anharmonic Phonons and Their Impact on Electron-Phonon Coupling

verfasst von | submitted by

Dott. Dott. mag. Luigi Ranalli

angestrebter akademischer Grad | in partial fulfilment of the requirements for the degree of

Doktor der Naturwissenschaften (Dr.rer.nat.)

Wien | Vienna, 2025

Studienkennzahl lt. Studienblatt | Degree programme code as it appears on the student record sheet:	UA 796 605 411
Dissertationsgebiet lt. Studienblatt | Field of study as it appears on the student record sheet:	Physik
Betreut von | Supervisor:	Univ.-Prof. Dr.techn. Cesare Franchini

Cosa vuoi? Siamo scimmie terrestri.
Cosa sei, se non polvere nel vento?

What do you want? We are earthbound apes.
What are you, if not dust in the wind?

— Verdena, *Loniterp* e *Chaise Lounge*

Acknowledgements

First, I would like to express my deepest gratitude to Cesare Franchini, for the invaluable guidance, support, and encouragement throughout this journey. It was an adventure of growth and good memories. I will never forget your support when coming to Vienna was at stake. I'm still sorry for that call you got—when one of your students (yes, me) entered Sensengasse 8 to download some data. He probably didn't deserve your respect that day.

An enormous thanks, of course, to Carla. You are an incredible person, and I've learned so many things from you—though I'd need to write a whole separate dissertation just to list a few. Chicago was a blast. I wish you the most prosperous of things possible.

After Cesare, the first person I met at the CMP was Michele. The first of many coffees and lunches was with you. We got Chinese nearby. You were a linchpin in and out of academia, from the early days of my project until your last days in Vienna. I only regret that we've *never* had a beer together.

Thank you, Feliciano, for helping me with the bike-gate, and for offering me one of the best opportunities of my life. Thanks, Annecy, for the bike. Thanks to all the amazing young researchers in Austin. Thanks, Sabya. I've loved Austin as much as it has "warmly" welcomed me.

Thanks to everyone at the VDSP. Thanks to tireless Christiane, and to all the students who joined the VDSP lunches—even though I always brought the same sweets for you.

Thank you Carolin, Dario, Firat, Florian, Georg, Giorgio, Johanna, Joseph, Lorenzo, Marco C., Markus, Matthias, Michael P., Michael W., Panu, Stefano, Taikang, Viktor, Yu and everyone who joined the quantum materials seminars (thanks, Caroline!). In particular, thanks to those who came to our dinners afterward. Thanks also to Christine and Doris.

Thanks to my *compari*—I'm happy that life is starting to pay us back, and I wish the best for you from the bottom of my heart. Thanks to the friends of a lifetime, standing proud and tall, no matter what. I am sure—forever.

Thanks to Ioana, for meeting so early in Vienna. Thanks for turning life into a Ghibli film.

Thanks to my mum, my dad, and my grandma—for being tough, and for making me the annoying man that I am. Thank you from the bottom of this heart that often doesn't speak too much.

Thanks to Teramo, Bologna, Vienna, Austin, and Turin—these giants I have been honoured to dwell.

Zusammenfassung

Phononische Anharmonizität und Nullpunktsquantenfluktuationen in der Gitterdynamik werden bei *ab initio*-Simulationen aufgrund der erheblichen Rechenkosten übersehen. In dieser Arbeit entwickeln wir einen Arbeitsablauf unter Verwendung von maschinell lernenden Kraftfeldern (MLFF) in Kombination mit der stochastischen selbstkonsistenten harmonischen Annäherung (SSCHA), um Phonon-Anharmonizität und Quantendynamik zu modellieren. Wir liefern genaue temperaturabhängige Phononendispersionen für $KTaO_3$ und $SrTiO_3$ im anharmonischen Softmodegetriebenen quantenparaelektrischen Regimen und darüber hinaus und demonstrieren damit die Effizienz und Genauigkeit unseres Ansatzes. Dieser Arbeitsablauf kann für die Einbeziehung anharmonischer Phononeffekte in die Berechnung von ElektronPhonon Kopplungselementen genutzt werden. Wir berechnen die Elektronenmobilität in $KTaO_3$ und $SrTiO_3$ unter Verwendung der BoltzmannTransportgleichung BoltzmannTransportgleichung (BTE), wobei wir die Gitterstörung und die Renormierung der Bandstruktur mit der ZGMethode berücksichtigen. Wir stellen eine 300%ige Überschätzung der Mobilität im Vergleich zu experimentellen Daten fest und führen dies auf die Einschränkungen des Quasiteilchenmodells zurückzuführen. Dementsprechend zeigen unsere weiteren Ergebnisse die Bildung von großen Elektronenpolaronen, was auf ein polaronisches Transportregime hindeutet. Außerdem berechnen wir die temperaturabhängige Bandlückenrenormierung in Diamant, indem wir unseren Arbeitsablauf zur Berechnung von anharmonischen dynamischen Matrizen mit der ZG SupercellVerschiebungsmethode, wobei die Ergebnisse eng mit experimentellen Beobachtungen übereinstimmen. Diese Ergebnisse validieren die MLFF+SSCHAMethode zur Untersuchung der Quanten und anharmonischen Phononendynamik und ihrer Auswirkungen auf die ElektronPhononKopplung.

Abstract

Phonon anharmonicity and zero-point quantum fluctuations in lattice dynamics are often overlooked in *ab initio* simulations due to significant computational costs. In this thesis, we develop a computational workflow using machine learning force fields (MLFF) combined with the stochastic self-consistent harmonic approximation (SSCHA) to model phonon anharmonicity and quantum dynamics. We provide accurate temperature dependent phonon dispersions for $KTaO_3$ and $SrTiO_3$ in the anharmonic soft-mode driven quantum paraelectric regimes and beyond, demonstrating the efficiency and accuracy of our approach. This workflow can be exploited for the inclusion of anharmonic phonon effects in the calculation of electron-phonon coupling elements. We compute electron mobility in $KTaO_3$ and $SrTiO_3$ using the Boltzmann transport equation (BTE), incorporating lattice disorder and bandstructure renormalization via the ZG method. We identify a 300% overestimation of mobility compared to experimental data, attributing this to the limitations of the quasiparticle model. Accordingly, our further findings reveal the formation of large electron polarons, suggesting a polaronic transport regime. Additionally, we compute temperature-dependent bandgap renormalization in diamond combining our workflow to compute anharmonic dynamical matrices with the ZG supercell displacements method, with results closely aligned with experimental observations. These outcomes validate the MLFF+SSCHA method for investigating quantum and anharmonic phonon dynamics and its effects on electron-phonon coupling.

Contents

Abstract **11**

Contents **13**

Acronyms **17**

1 Introduction **21**

1.1 Overview 22

2 Many body Hamiltonian **25**

2.1 Born-Oppenheimer Approximation 26

2.2 Density Functional Theory 28

2.3 Ionic Hamiltonian 30

2.4 Quasi Harmonic Approximation 35

3 Assessing phonon anharmonicity **39**

3.1 Stochastic Self-Consistent Harmonic Approximation (SSCHA) . . 40

3.2 Machine Learned Force-Field (MLFF) 43

4 Phonon Anharmonicity in $KTaO_3$ **47**

4.1 Introduction 49

4.2 SSCHA+MLFF workflow 50

4.3 Quantum Paraelectric state 53

4.3.1 Comparison with $SrTiO_3$ 59

4.3.2 Preliminary results on strained $KTaO_3$ 59

5 Electron-phonon coupling with phonon anharmonicity **63**

5.1 Electron-Phonon Coupling 65

5.2 Boltzmann transport equation 68

5.3 Special Displacements Methods 70
5.4 Polarons in density functional perturbation theory (DFPT) 71

6 Bandgap Renormalization in Diamond **73**
6.1 Introduction 74
6.2 Methods 76
6.3 Volume Expansion and Phonon Dispersions 77
6.4 Bandgap renormalization 78

7 Mobility and phonon anharmonicity **83**
7.1 Introduction 85
7.2 Methods 87
7.2.1 Training and validation of MLFFs 88
7.2.2 MLFF+SSCHA calculations 91
7.2.3 Renormalization of the Electron-Phonon Matrix Elements and Mobility Calculations 92
7.2.4 Mass Enhancement and Inclusion of Local Disorder 96
7.3 Results and discussion 98

8 Polarons in $KTaO_3$ and $SrTiO_3$ **111**
8.1 Introduction 112
8.2 Methods 113
8.2.1 Electron Polaron 113
8.2.2 Hole Polaron 116

9 Summary and Outlook **119**
9.1 Summary 119
9.2 Outlook 120

Bibliography **123**

List Of Publications **137**

Acronyms

BEC Born effective charge. 18

BO Born-Oppenheimer. 9, 11, 12, 14, 28, 29, 46

BTE Botlzmann transport equation. 8, 48

BvK Born-von-Kármán. 46

BZ Brillouin-zone. 48

DBW Debye-Waller. 46

DFPT density functional perturbation theory. 17, 18, 46, 49, 51

DFT density functional theory. 9, 12, 14, 15, 17, 36, 46, 47, 49, 51, 54, 56, 57

DM dynamical matrix. 17, 18, 26

FC force constant. 15, 16, 18, 26

FD finite differences. 17, 35

FE ferroelectric. 31, 32, 34

GGA generalized gradient approximation. 36

HA harmonic approximation. 6, 7, 9, 18–20, 30, 45, 46, 49, 52

KS Kohn-Sham. 47, 50

BM-EoS Birch-Murnaghan equation of state. 9, 21, 54, 56

MC Monte Carlo. 29, 33, 35, 45, 50

MD molecular dynamics. 15, 27–29, 32, 33, 35, 54

ML machine learning. 27

MLFF machine-learned force field. 7, 8, 23, 26, 27, 29, 30, 32, 33, 35, 36, 45, 52, 54, 56, 57, 59, 62

MLWF maximally localized Wannier functions. 48

PAW projector augmented wave. 36

PE paraelectric. 32

PES potential energy surface. 9, 15, 18–20, 30

PPs pesudopotentials. 36

QCP quantum critical point. 31, 34

QHA Quasi Harmonic Approximation. 9, 20, 54, 56, 57

QP quasi-particle. 59

QPE quantum paraelectric. 7, 31, 32, 34

RMSE root mean square error. 29

SCAN Strongly Constrained and Appropriately Normed. 36

SCHA self-consistent harmonic approximation. 24–26

SSCHA stochastic self-consistent harmonic approximation. 7, 8, 23, 26, 27, 30, 32–36, 45, 52–55, 59, 63

TO transversal optical. 30, 31

VASP Vienna *ab initio* simulation package. 27, 36

ZPE zero point energy. 6, 7, 19, 31

ZPR zero point renormalization. 20, 50

CHAPTER 1

Introduction

Modelling the atomic vibrations in condensed matter systems requires the accurate description of the electronic and ionic potential with respect to the atomic displacements. The most common approach relies on the harmonic approximation (HA) of the lattice dynamics. In this approximation the ions are treated as classical point particles subject to a position dependent scalar electronic potential acting on the atoms in their equilibrium positions and a static Coulomb potential mediated by their ionic charges. The electronic potential is thus expanded up to second order. The HA is remarkably successful since most materials show a parabolic electronic potential near equilibrium. Furthermore, the vibrational energy at room temperature is usually way higher than the zero point energy (ZPE) of the bosonic ensemble, which signals a mostly classical regime for the ionic motion.

The HA however fails in various scenarios cases. The most obvious case manifests for any material at very high temperatures: ions travel big distances with respect to their equilibrium positions, thus breaking the validity of the second order Taylor expansion for small ionic displacements. Another example could be the intense quantum vibrations in light atoms, which often overcome the thermal energy even at temperatures far from the absolute zero. Furthermore, when approaching a phase transition, the electronic potential profile 'flattens-out' for certain collective displacements, thus weakening the potential well the atoms are embedded in. This means that the potential does not show its characteristic parabolic behavior, and vibrations are more likely to be anharmonic. At the

same time, the ZPE becomes very relevant with respect to the thermally-driven vibrational energy, effect that is not captured in the HA.

The spirit of this dissertation consists in tackling cases in which phonon anharmonicity plays a crucial role and modifies both the lattice dynamics and the intensity of the electron-phonon coupling, which is usually treated in the HA for lattice dynamics. We furthermore propose the use of machine-learned force field (MLFF) to accelerate calculations performed in the stochastic self-consistent harmonic approximation (SSCHA), a state-of-the-art approach for modeling anharmonic lattice dynamics with the inclusion of quantum vibrations.

1.1 Overview

Chapter 2 offers a an essential review of the theory underlying first-principles calculations in solid-state Physics, which usually leverage a density functional theory (DFT) approach to the Born-Oppenheimer (BO) Hamiltonian. This framework allows for the determination of the ground state energy of the system and its spatial electronic density. Furthermore, it allows for the modeling of the atomic vibrations, usually in the HA.

Chapter 3 introduces the SSCHA method. We propose a scheme for speeding up the SSCHA calculations through the use of a MLFF. The MLFF proves to be particularly suitable since it allows for an accurate and fast prediction of the system energy and interatomic forces in large supercells.

Chapter 4 is a case study. It offers a historically relevant example of phase transition in bulk $KTaO_3$, where the interplay of phonon anharmonicity and ZPE generates an exotic state of matter called "quantum paraelectricity", where the material is on the verge of a ferroelectric (FE) phase transition from the cubic paraelectric (PE) to the tetragonal FE phase. The behavior of the ionic vibrations as a function of temperature in the PE, quantum paraelectric (QPE) and FE phases is accurately described with the use of the SSCHA+MLFF framework, thus offering an interesting test case.

Accounting for phonon anharmonicity is expected to also generate an effect on the electron-phonon coupling. Chapter 5 sums up the standard treatment

of the electron-phonon interaction in the HA approximation for the nuclei, and explains its relevance in the prediction of the various electronic properties. In particular, the determination of the electron-phonon matrix elements opens the path for the calculation of carrier mobilities through the Botlzmann transport equation (BTE) and to the exploration of a possible polaron formation in the materials under investigation. Thus, we propose the integration of the temperature dependent anharmonic phonons in a "renormalized" electron-phonon tensor. Furthermore, the anharmonic dynamical matrix (DM)s can be used to compute the ZG displacements, thus offering a handy way of including lattice anharmonicity in the vibrational average of the electronic eigenvalues.

Chapter 6 is a case study, and it somewhat departs from the main line of investigation focusing on oxide perovskites. Nonetheless, it offers a clear example of how phonon anharmonicity can play an important role in electron-phonon coupling, even for a largely harmonic compound, such as diamond. We calculate the indirect bandgap renormalization due to electron-phonon coupling and lattice expansion in diamond. The electronic eigenvalues renormalization is obtained through the use of the aforementioned ZG displacements method, by employing both the harmonic and the anharmonic DMs.

Chapter 7 is the most dense part of this dissertation, and it connects with the study presented in Chapter 4. It deals with the electron mobility in $KTaO_3$ and $SrTiO_3$ as calculated in the standard BTE formalism but with the inclusion of phonon anharmonicity in the renormalized electron-phonon coupling tensor. The use of temperature dependent dispersions is necessary in case of strongly anharmonic compounds. The mobility trend as a function of temperature obtained for both the compounds agrees with the experimental data, but the values are massively overestimated in $SrTiO_3$ with respect to $KTaO_3$. order to explain the discrepancy, we consider the effect of lattice disorder in $SrTiO_3$ on the electronic bandstructure, and we employ these eigenvalues in the BTE equations. We calculate the renormalization of the electronic effective masses at the conduction band bottom for both $KTaO_3$ and $SrTiO_3$ through the ZG method, starting from the respective anharmonic dynamical matrices. We estimate how the electron mobility is affected by the mass rescaling, and obtain a final overestimation of

the experimental mobility of the 300% for both compounds.

The origin of this remaining discrepancy is also discussed. As a consequence of the puzzling picture that Chapter 7 leaves behind, in Chapter 8 we investigate the formation of polarons in these materials. We show the formation of a large electron polaron and a small hole polaron in $KTaO_3$ and $SrTiO_3$, which could be an explanation for the failure of the BTE approach to carrier mobility in both materials. These polaron calculations can also be performed with the inclusion of phonon anharmonicity.

In Chapter 9 we draw our final remarks and suggest future explorations of the anharmonic phonon dynamics through the MLFF+SSCHA approach and of their effect on the electron-phonon mediated quantities.

CHAPTER 2

Many body Hamiltonian

This chapter condenses the standard treatment of the many-body Hamiltonian which forms the theoretical backbone for understanding condensed matter systems with translational symmetry.

Section 2.1 introduces the BO approximation of the many body Hamiltonian, which allows for the separate treatment of the electronic and ionic degrees of freedom. Even if the BO eigenvalue problem is still computationally expensive, it lays the basis for more advanced theory frameworks.

Section 2.2 delves into DFT, which is based on the BO approximation and consists in a variational approach for the total energy of the system that shifts the problem from the determination of the many-body wavefunction to the determination of the single particle electronic density.

Section 2.3 provides a deeper exploration of the ionic Hamiltonian as arising from the BO approximation, and establishes the link between the second derivative of the potential energy surface (PES) and the force constant matrix which described the ionic motion at equilibrium. This treatment takes the name of HA approximation, and its limits are highlighted in the final remarks.

Section 2.4 explains how lattice expansion in temperature can be calculated in the Quasi Harmonic Approximation (QHA) by combining the HA and the the Birch-Murnaghan equation of state (BM-EoS). The limits of this rough approach are exposed, along with the need for a more advanced treatment of the ionic vibrations that takes into consideration the anharmonic effects.

2.1 Born-Oppenheimer Approximation

The computational condensed matter physics community employs a well-known arsenal of codes which aim at solving the Schröedinger equation of N electrons on a periodic lattice of M ions, where M and N are virtually infinite. The Hamiltonian is composed of five contributions:

$$\hat{H} = -\sum_{i=1}^{N} \frac{\hbar^2 \nabla_i^2}{2m_e} - \frac{1}{2}\sum_{j\neq i}^{N} \frac{e^2}{|\mathbf{r}_{ij}|} + \sum_{I=1}^{M} \frac{\hbar^2 \nabla_I^2}{2M_I} - \frac{1}{2}\sum_{J\neq J}^{M} \frac{Z_I Z_J e^2}{|\mathbf{R}_{IJ}|} + \sum_{i=1}^{N}\sum_{I=1}^{M} \frac{Z_I e^2}{|\mathbf{r}_i - \mathbf{R}_I|}, \tag{2.1}$$

where, M_I is the mass of the atom I, m_e is the electron mass, e is the elementary electronic charge, Z is the atomic number, $\mathbf{r}_{ij}$ is the distance between the electrons in positions $\mathbf{r}_i$ and $\mathbf{r}_j$, $\mathbf{R}_{IJ}$ is the distance between the atoms in positions $\mathbf{R}_I$ and $\mathbf{R}_J$. The first term in Eq. (2.1) is the electronic kinetic energy operator $\hat{T}_e$, the second is the Coulombic electron-electron repulsion $\hat{U}_{ee}$, the third is the ionic kinetic energy $\hat{T}_n$, the fourth is the Coulombic ion-ion repulsion $\hat{U}_{nn}$ and the fifth is the electron-ion attractive potential energy $\hat{U}_{en}$.

For convenience, we thus rewrite Eq. (2.1) as:

$$\hat{H} = \hat{T}_e + \hat{U}_{ee} + \hat{T}_n + \hat{U}_{nn} + \hat{U}_{en}. \tag{2.2}$$

The Hamiltonian in Eq. (2.1) is able to describe a huge variety of collective states of matter, but what we are interested in here is the crystal phase, where the kinetic terms $\hat{T}_e$ and $\hat{T}_n$ are small with respect to $\hat{U}_{en}$. The most peculiar and mathematically useful feature of the crystal phase is that the equilibrium positions of the ions are periodically distributed in space, and follow those crystallographic structures that result from the translational symmetry groups. The Hamiltonian can thus be solved for an irreducible set of atoms living in a spatial area called unit cell (UC), which reproduces the whole lattice by translational symmetry. This description may however be problematic when the material actually shows long range orderings, impurities, and, in general, effects that cannot be described by the UC picture.

From a computational standpoint, the numerical solution of Eq. (2.1) is a rather impractical road, since it requires the sampling of the spatial 3D coordinates associated to each electron and ion of the many-body wavefunction $\Psi(\mathbf{r}_1, ..., \mathbf{r}_N, \mathbf{R}_1, ...\mathbf{R}_M)$.

A tractable Hamiltonian can be obtained by using the BO approximation [1], which is also called of the "fixed nuclei", or "adiabatic", since it assumes that the electronic and ionic motions can be decoupled. The *geist* of this approach can be intuited by a rather simple argument. In an isolated system, in the reference frame of the center of mass, the impulses related to the involved particles sum to zero. Thus, in this case $p_{ion} = M_{ion} v_{ion} \approx p_{el} = m_{el} v_{el}$ (neglecting the relativistic effects: electrons and ions velocities are far lower than the speed of light), that is, the impulse of whatsoever ion is comparable to that of whatsoever electron. This implies that $v_{ion} \approx (m_{el}/M_{ion}) v_{ion}$, and since the ratio of the electronic and the ionic mass is smaller than one thousandth, the ionic velocities is far less than those of the electrons, and the ions can be considered to be fixed.

The ansatz for the total wavefunction Ψ consists in the product of the electronic and ionic wavefunctions:

$$\Psi(\mathbf{r}_1, ..., \mathbf{r}_N, \mathbf{R}_1, ...\mathbf{R}_M) = \Psi(\mathbf{r}_1, ..., \mathbf{r}_N)\chi(\mathbf{R}_1, ...\mathbf{R}_M). \tag{2.3}$$

By fixing the nuclear coordinates $\mathbf{R} = \{\mathbf{R}_1, ...\mathbf{R}_M\}$, Eq. (2.1) develops the BO eigenvalue problem for the electronic part:

$$\left[-\sum_i \frac{\nabla_i^2}{2} + \sum_i U_{en}(\mathbf{r}_i, \mathbf{R}) + \frac{1}{2} \sum_{i \neq j} \frac{1}{|\mathbf{r}_i - \mathbf{r}_j|} \right] \Psi_{\mathbf{R}} = E_{\mathbf{R}} \Psi_{\mathbf{R}}. \tag{2.4}$$

By using equations. 2.3 and 2.4 in Eq. (2.1), we find:

$$E_{\mathbf{R}} \Psi_{\mathbf{R}} \chi + \left[-\sum_I \frac{\nabla_I^2}{2M_I} + \frac{1}{2} \sum_{I \neq J} \frac{Z_I Z_J}{|\mathbf{R}_I - \mathbf{R}_J|} \right] \Psi_{\mathbf{R}} \chi = E_{tot} \Psi_{\mathbf{R}} \chi. \tag{2.5}$$

After multiplying both side of Eq. (2.5) by $\Psi_{\mathbf{R}}^*$ and integrating over $\int d\mathbf{r}_1 ... d\mathbf{r}_N$, we obtain:

$$\left[-\sum_I \frac{\nabla_I^2}{2M_I} + \frac{1}{2}\sum_{I\neq J}\frac{Z_I Z_J}{|\mathbf{R}_I - \mathbf{R}_J|} + E_{\mathbf{R}}\right]\chi = E_{tot}\chi. \tag{2.6}$$

Eq. (2.6) describes a system of nuclei interacting through a Coulomb potential and affected by the electron cloud through its total energy $E_{\mathbf{R}}$ as function of the nuclear coordinates,

Finding $\Psi_{\mathbf{R}}(\mathbf{r}_1, ..., \mathbf{r}_N)$ and $E_{\mathbf{R}}$ is, however, still a computationally intractable problem in most of condensed matter systems, due to the high number of electrons to be considered.

2.2 Density Functional Theory

In a nutshell, DFT shifts the attention from the many-body electronic wavefunction of N interacting electrons $\Psi(\mathbf{r}_1, ..., \mathbf{r}_N)$ to the electron density

$$n(\mathbf{r}) = N\int d\mathbf{r}_2 ... d\mathbf{r}_N \Psi(\mathbf{r}, \mathbf{r}_2, ..., \mathbf{r}_N)|^2. \tag{2.7}$$

The advantage comes from two theorems laid out by Hohenberg and Kohn [2]. Let's imagine that the N interacting electrons are subject to a potential $V_{ext}(\mathbf{r})$. The first theorem states that $V_{ext}(\mathbf{r})$ is uniquely defined by the ground state density $n_0(\mathbf{r})$, while the second theorem states that the energy of the system is a unique functional of its density, and has the form:

$$E[n] = F[n] + \int V_{ext}(\mathbf{r})n(\mathbf{r})d\mathbf{r}, \tag{2.8}$$

where $F[n]$ does not depend on V_{ext}. Furthermore, the ground sate energy $E_0(\mathbf{R})$ is the global minimum of the energy functional $E[n]$ and $n_0(\mathbf{r})$ minimizes it. In general, there is no analytic expression for $F[n]$.

At this point the Kohn-Sham (KS) scheme [3] suggests to map the N interacting electrons system to an auxiliary system of N independent electrons developing the same spatial ground-state density $n_0(\mathbf{r})$ as the original interacting system. This system is described by single-particle orbitals $\psi_i(\mathbf{r})_{i=1,2,...,N}$ and

subject to the same external potential $V_{ext}(\mathbf{r})$. We first rewrite the energy of the interacting system as:

$$E[n] = T^{int}[n] + E_{ext}[n] + E_H[n] + E_{xc}^{int}[n], \tag{2.9}$$

where $T^{int}[n]$ is the kinetic energy functional of the interacting electrons, $E_{ext}[n]$ can be thought of as the electron-ion interaction, $E_H[n]$ is the Hartree functional (Coulomb interaction) and $E_{xc}^{int}[n]$ is the exchange-correlation energy of the interacting system. The only terms than we can write down analytically as density functionals are the Hartree energy:

$$E_H[n] = \frac{e^2}{2} \int \frac{n(\mathbf{r})n(\mathbf{r}')}{|\mathbf{r} - \mathbf{r}|} d\mathbf{r}d\mathbf{r}' \tag{2.10}$$

and the external field acting on the electron density:

$$E_{ext}[n] = \int V_{ext}(\mathbf{r})n(\mathbf{r})\mathbf{r}. \tag{2.11}$$

The kinetic $T^{int}[n]$ and the exchange-correlation $E_{xc}^{int}[n]$ energy functionals do not have a simple analytic expression. The KS approach, however, suggests that we can write an analogous energy functional for the system of independent electrons:

$$E[n] = T^{ip}[n] + E_{ext}[n] + E_H[n] + E_{xc}^{ip}[n], \tag{2.12}$$

where $T^{ip}[n]$ has analytical expression since it represents the kinetic energy for a system of independent particles, and $E_{xc}^{ip}[n]$ incorporates both the exchange-correlation energy and the correction to the kinetic energy:

$$E_{xc}^{ip}[n] = (T^{int}[n] - T^{ip}[n]) + E_{xc}^{int}[n]. \tag{2.13}$$

Now, $E_{xc}^{ip}[n]$ can be written as:

$$V_{xc}^{ip}[n](\mathbf{r}) = \frac{\partial E_{xc}^{ip}}{\partial n(\mathbf{r})}. \tag{2.14}$$

This allows us to define an effective potential, the KS potential, as:

$$V_{KS}[n](\mathbf{r}) = V_{ext}(\mathbf{r}) + V_H(\mathbf{r}) + V_{xc}^{ip}[n](\mathbf{r}). \tag{2.15}$$

We can now write down the set of N independent Schröedinger equations:

$$\hat{H}_{KS}\psi_i(\mathbf{r}) = \left(-\frac{\hbar^2\nabla^2}{2m_e} + V_{KS}[n](\mathbf{r})\right)\psi_i(\mathbf{r}) = \varepsilon_i\psi_i(\mathbf{r}) \tag{2.16}$$

which can be solved self-consistently by starting from a guess for the electronic density, computing the KS orbitals $\psi_i(\mathbf{r})$ and KS eigenvalues ε_i, and updating the density $n(r)$ for the next iteration until convergence. Finally, once the self-consistent density has been obtained, the total energy of the electronic system is given by:

$$E[n] = \sum_{i=1}^{N}\varepsilon_i - \frac{e^2}{2}\int\frac{n(\mathbf{r})n(\mathbf{r}')}{|\mathbf{r}-\mathbf{r}'|}d\mathbf{r}d\mathbf{r}' + E_{xc}^{ip}[n] - \int V_{xc}(\mathbf{r})n(\mathbf{r})d\mathbf{r}. \tag{2.17}$$

Typically, the KS scheme is performed at fixed ionic positions, as per the BO approximation introduced in Section 2.1. We thus have a framework for computing the electronic ground state energy $E_{\mathbf{R}}$ in Eq. (2.6), paving the way for the study of the ionic properties in the BO approximation.

2.3 Ionic Hamiltonian

Once $E_{\mathbf{R}}$ is known, Eq. (2.6) is well defined. Nevertheless, in line with the BO approximation, the nuclei can be considered as classical particles. By substituting the quantum mechanical momentum in Eq. (2.6) with the classical one:

$$-i\nabla_I = i\frac{\partial}{\partial\mathbf{R}_I} \rightarrow \mathbf{P}_I, \tag{2.18}$$

the following classical Hamiltonian for the nuclei is obtained:

$$\hat{H}_n^{class} = \sum_I\frac{\mathbf{P}_I^2}{2M_I} + U(\mathbf{R}_1, \mathbf{R}_2, ..., \mathbf{R}_M), \tag{2.19}$$

where $U(\mathbf{R}_1, \mathbf{R}_2, ..., \mathbf{R}_M)$ is the PES and it is defined as:

$$U(\mathbf{R}_1, \mathbf{R}_2, ..., \mathbf{R}_M) = \frac{1}{2} \sum_{I \neq J} \frac{Z_I Z_J}{|\mathbf{R}_I - \mathbf{R}_J|} + E_{\mathbf{R}}. \tag{2.20}$$

The equation of motion associated to the Hamiltonian in Eq. (2.19) then reads:

$$M_I \frac{d^2 \mathbf{R}_I}{dt^2} = -\frac{\partial U}{\partial \mathbf{R}_I}, \tag{2.21}$$

where $-\frac{\partial U}{\partial \mathbf{E}_I}$ is the force $\mathbf{F}_I$ acting on the ion I of mass M_I. The equilibrium structure of the material can thus be found by minimizing the forces acting on each atom of the system: we determine the PES and resulting forces at each step of the structural minimization. On a side note, Eq. (2.21) is also the basis for molecular dynamics (MD) calculations. The instantaneous forces acting on the ions are computed as the sum of the ion-ion Coulomb force and the derivative of the potential as obtained in DFT through the Hellman-Feynman theorem [4, 5].

If such global energy minimum exists, then it can be found at a finite set of atomic coordinates $\mathbf{R^0}_1, \mathbf{R^0}_2, ..., \mathbf{R^0}_M$. We can Taylor-expand $U(\mathbf{R}_1, \mathbf{R}_2, ..., \mathbf{R}_M)$ as:

$$U(\mathbf{R}_1, \mathbf{R}_2, ..., \mathbf{R}_M) = U(\mathbf{R}^0_1, \mathbf{R}^0_2 x, ..., \mathbf{R^0}_M) + \frac{\partial U}{\partial R_{I\alpha}} u_{I\alpha} + \frac{1}{2} \frac{\partial^2 U}{\partial R_{I\alpha} R_{J\beta}} u_{I\alpha} u_{J\beta}, \tag{2.22}$$

where α and β are cartesian coordinates and the second partial derivatives are referred to as the Born-von-Karman force constants (FCs) [6, 7]:

$$K_{I\alpha, J\beta} = \frac{\partial^2 U}{\partial R_{I\alpha} \partial R_{J\beta}}. \tag{2.23}$$

Since at equilibrium the forces acting on the ions are zero, we can combine Equations. 2.22 and 2.23 to obtain the expression for the PES in the HA:

$$U = U_0 + \frac{1}{2} \sum_{I\alpha} \sum_{K\beta} K_{I\alpha, J\beta} u_{I\alpha} u_{J\beta}. \tag{2.24}$$

The equation of motion in Eq. (2.21) can be then casted via Eq. (2.23) as:

$$M_I = \frac{d^2 u_{I\alpha}}{dt^2} = -K_{I\alpha,J\beta} u_{J\beta}. \tag{2.25}$$

Periodic systems are composed of many UCs l; it is convenient to make this information explicit by a different labeling:

$$\mathbf{R}_I = \mathbf{R}_l + \tau_s, \tag{2.26}$$

where $\mathbf{R}_l$ is the position of the UC l in the virtually infinite supercell and τ_s indicates the position of a nucleus within the UC l. The Born-von-Karman FC can be then written as:

$$K_{ls\alpha,l's'\beta} = \frac{\partial^2 U}{\partial(R_{l\alpha} + \tau_{s\alpha})\partial(R_{l'\beta} + \tau_{s'\beta})}, \tag{2.27}$$

and the equation of motion is recasted as:

$$M_s = \frac{d^2 u_{ls\alpha}}{dt^2} = -K_{ls\alpha,J\beta} u_{l's'\beta}. \tag{2.28}$$

The solution of Eq 2.28 can be written as:

$$u_{ls\alpha}(\mathbf{q}, t) = u^0_{s\alpha} e^{i[\mathbf{q}\cdot(\mathbf{R_l}+\tau_s)-\omega t]}. \tag{2.29}$$

By replacing Eq 2.29 in Eq 2.28 and exploiting the invariance of the FC with respect to translations of a reciprocal lattice vector, we obtain the eigenvalue equation:

$$\sum_{s'\beta} D_{s\alpha,s'\beta}(\mathbf{q}) v^0_{\mathbf{q},s'\beta} = \omega^2(\mathbf{q}) v^0_{\mathbf{q},s\alpha}, \tag{2.30}$$

with $v^0_{d\alpha} = M_s^{\frac{1}{2}} u^0_{s\alpha}$, and

$$D_{s\alpha,s'\beta}(\mathbf{q}) = \frac{1}{(M_s M_{s'})^{\frac{1}{2}}} \sum_l e^{i\mathbf{q}\cdot\mathbf{R}_l} e^{i\mathbf{q}\cdot(\tau_{s'}-\tau_s)} K_{0s\alpha,ls'\beta} \tag{2.31}$$

is the DM. Here, s and s' indicate a pair of atoms in the UC. The eigenvalues problem of Eq. (2.30) consists in a system of $s \cdot \alpha$ equations, to be solved for each $\mathbf{q}$ point of the reciprocal space. When considered continuously in the reciprocal space, we call these solutions "phonon branches". Obtaining the phonon frequencies as a function of the wavevector $\mathbf{q}$ requires either the direct calculation and diagonalization of the DM in the unit cell by DFPT approach [8], or the calculation of the FC matrix on a supercell through DFT and finite differences (FD) [9], with subsequent Fourier interpolation at a reciprocal $\mathbf{q}$-point in the $1^{st}BZ$ through Eq 2.31. The DFT-FD approach consists, indeed, in the calculation of the second derivative of the BO with respect to two consecutive atomic displacements. For computational setups of equivalent precision, after Fourier interpolation, the DFT-FD approach obtains the same branch frequencies $\omega(\mathbf{q})$ of DFPT when the supercell is "commensurate" with the wavevector $\mathbf{q}$ [10]. That is, when the cartesian components of $\mathbf{q}$ express a multiple of the ratio between the UC size and the supercell size. For example, a supercell of size $4 \times 4 \times 4$ is commensurate with $\mathbf{q}^* = (0.5, 0.0, 0.25)$. In this case, the minimal commensurate supercell would have dimensions $2 \times 1 \times 4$. The concept of commensurate supercell will be echoed in the next chapters, and in general, it is useful both in phonon calculations and linear-response theories based on DFT-FD, even if outside of the scope of this dissertation.

The direct calculation of $\omega(\mathbf{q})$ on a dense reciprocal space sampling is a rather complicated task for which Fourier interpolation is the most common solution, but not without some precaution. Whether in FD-DFT or DFPT, one needs to pass through the FC. When interpolating around the Γ point ($\mathbf{q} = (0, 0, 0)$), the long range components of the FC are not correctly accounted for, mostly in these materials where these interactions are strong, like in polar semiconductors. A common strategy consists in subtracting the long range contribution to the FC before Fourier interpolation, and then adding it back to the DM around the Γ-point:

$$D_{s\alpha,s'\beta}(\mathbf{q}\to\mathbf{0}) = D_{s\alpha,s'\beta}(\mathbf{q}=\mathbf{0}) \tag{2.32}$$

$$+\frac{1}{\sqrt{M_s M_s'}}\frac{4\pi}{\Omega_0}\frac{[\sum_\gamma q_\gamma Z^*_{s,\gamma\alpha}][\sum'_\gamma q'_\gamma Z^*_{s',\gamma'\beta}]}{\sum_{\alpha\beta} q_\alpha \epsilon^\infty_{\alpha\beta} q_\beta}. \tag{2.33}$$

Eq. (2.32) is called non-analytical term correction (NAC) and represents the long range dipole-dipole interaction [11–13]. Z^* is the Born effective charge (BEC) tensor, ϵ^∞ the electronic contribution to the dielectric tensor, Ω_0 the UC volume, s the atomic index and γ, α and β cartesian indexes. This correction may not be enough to reproduce the phonon dispersion around the Γ-point, but this would be outside of the scope of this dissertation.

Despite its great success in reproducing the vibrational frequencies of molecules and solids as measured by Raman spectroscopy, inelastic neutron scattering, infrared spectroscopy, inelastic X-ray scattering, electron energy-loss spectroscopy and inelastic electron tunneling, the HA has some severe limitations. First of all, the equipartition theorem predicts a mean square ionic displacement proportional to the temperature $\langle u^2\rangle_T \propto K_B T$, with K_B being the Boltzmann constant. This means that at 0 K the lattice should be completely still, while vibrational frequencies show a well defined peak intensity near the absolute thermal zero. Luckily enough, a full quantum treatment of the bosonic function, keeping the second order of expansion of the PES in Eq. (2.22), predicts a zero-point amplitude for the mode ν at wavevector $\mathbf{q}$ expressed as:

$$l_\nu(\mathbf{q}) = \sqrt{\frac{\hbar}{2m_{eff}\omega_{\mathbf{q}\nu}}}, \tag{2.34}$$

where m_{eff} is the effective mass associated to the particular vibrational mode ν. The ZPE is expressed as:

$$E_{ZPE} = \sum_\nu \int \frac{d\mathbf{q}}{\Omega_{BZ}} \frac{\hbar\omega_{\mathbf{q}\nu}}{2}. \tag{2.35}$$

The total bosonic energy, including the minimum of the PES and the thermodynamical occupancy, is:

$$E_{tot} = U_0 + E_{ZPE} + \sum_{\nu} \int \frac{d\mathbf{q}}{\Omega_{BZ}} n_{\mathbf{q}\nu} \hbar\omega_{\mathbf{q}\nu}, \tag{2.36}$$

where ω_{BZ} is the volume of the Brillouin-zone (BZ) and $n_{\mathbf{q}\nu}$ is the Bose-Einstein distribution, defined as:

$$n_{\nu}(\mathbf{q}) = \frac{1}{e^{\hbar\omega_{\mathbf{q}\nu}/k_B T} - 1}. \tag{2.37}$$

Eq. (2.34), (2.35) and (2.37) are then valid exclusively at the HA, for independent oscillators.

The quantum adjustment to the classical limit of the HA allows for a comparison with the intensity of the experimental vibrational peaks. This treatment, however, cannot describe phenomena like thermal expansion and the temperature dependence of the phonon frequencies. Importantly, phonon-phonon scattering is not present at the HA level, since it deals with independent oscillators, thus the phonon linewidth and lifetime are not defined, and their effect on vibrationally-derived properties are not accessible.

2.4 Quasi Harmonic Approximation

The HA models the vibrational properties of a crystal by assuming that atomic displacements around the equilibrium positions are small and the PES can be approximated as a quadratic function. While accurate at low temperatures, this approximation fails at higher temperatures where anharmonic effects become significant. The QHA tries to describe the volume-dependent thermal effects, such as the thermal expansion. It holds on the assumption that the HA is valid for any lattice constant. In the QHA, the free energy $F(V,T)$ of a crystalline solid at a given volume V and temperature T is composed of two terms, the electronic energy $E_{DFT}(V)$ and the vibrational energy $F_{HA}(V)$ in the HA:

$$F(V,T) = E_{\mathrm{DFT}}(V) + F_{\mathrm{HA}}(V,T), \tag{2.38}$$

where in turn $F_{\mathrm{HA}}(V,T)$ is the sum of the ZPE E_{ZPE} of Eq. 2.35 and the temperature dependent vibrational energy (classic, or thermal contribution):

$$F_{\mathrm{HA}}(V,T) = k_B T \sum_{\mathbf{q},\nu} \ln\left[2\sinh\left(\frac{\hbar\omega_{\mathbf{q},\nu}(V)}{2k_B T}\right)\right]. \tag{2.39}$$

At low temperatures, where the phonon occupation numbers are small, $F_{\mathrm{HA}}(V,T)$ simplifies to E_{ZPR}, but as temperature increases, the phonon thermal excitation may become significant.

The temperature dependence of the equilibrium volume can be calculated by minimizing Eq. 2.39 at each temperature. The equilibrium volume $V_{\mathrm{eq}}(T)$ satisfies the following condition:

$$\left(\frac{\partial F(V,T)}{\partial V}\right)_T = 0. \tag{2.40}$$

Suppose, for example, that we want to find the equilibrium volume $V_{\mathrm{eq}}(T^*)$ that minimizes the free energy in Eq. 2.39 at a certain temperature T^*. We can start from a reasonable guess for the equilibrium volume by performing a structural relaxation in DFT, and then we need to choose a set of N nearby volume points around this estimate. The idea is reconstructing the free-energy profile by calculating the free energy in Eq. 2.39 for this set of volumes, and then using an appropriate fitting function to extract $V_{\mathrm{eq}}(T^*)$. In order to do that, we calculate the electronic contribution at each volume $E_{\mathrm{DFT}}(V_1,...,V_N)$ (in DFT or DFPT) and perform the respective phonon calculations in the HA in order to obtain $F_{\mathrm{HA}}(V_1,...,V_N,T^*)$.

As said before, we need an analytic fitting function that allows us to capture $V_{\mathrm{eq}}(T^*)$. We employ the BM-EoS, which is a widely used model to describe the relationship between volume and energy under isotropic compression or expansion. It is particularly suitable for solid materials and it is often used to fit the calculated total energies from first-principles calculations at different volumes to extract the bulk modulus and its derivatives. The BM-EoS, in its third-order form, is given by:

$$E(V) = E_0 + \frac{9V_0B_0}{16}\left\{\left[\left(\frac{V_0}{V}\right)^{2/3} - 1\right]^3 B_0' + \left[\left(\frac{V_0}{V}\right)^{2/3} - 1\right]^2 \times \left[6 - 4\left(\frac{V_0}{V}\right)^{2/3}\right]\right\}, \tag{2.41}$$

where V_0 is the equilibrium volume, B_0 is the bulk modulus, and B_0' is its first derivative with respect to pressure. At each temperature, the equilibrium volume is determined by a BM-EoS fit of the free energy profile, as constructed by computing the electronic energy and the vibrational energy.

This combined approach allows for a detailed prediction of the temperature-dependent expansion of the lattice. As the temperature increases, the minimization process shifts the equilibrium volume, simulating the thermal expansion of the material. This approach is adopted in the case of Carbon in the diamond cubic structure in Chapter 6, and discussed in light of a more complete anharmonic theory.

CHAPTER 3

Assessing phonon anharmonicity

This Chapter introduces the idea behind the MLFF+SSCHA workflow.

In Section 3.1 we present the the SSCHA theory. The effective anharmonic FC matrix of a system can be estimated by minimizing the free energy of the ionic system in a self-consistent loop. The bottleneck of the procedure is the large amount of DFT calculation on large supercells required for the free energy minimization. Thus, we devise a workflow for integrating MLFF predictions and the SSCHA algorithm, in order to speed up the energy convergence and bypassing expensive DFT calculations.

Section 3.2 presents the MLFF model chosen in this dissertation and thus employed in the subsequent case studies.

The practical workflow is presented in Section 4.2.

3.1 Stochastic Self-Consistent Harmonic Approximation (SSCHA)

The SSCHA methods finds its implementation in the homonymous code [14–18]. We will dive into its premises and central algorithms in order to explain its scope and limitations.

A system of interacting atoms in the BO approximation is described by the Hamiltonian in Eq. (2.19). The associated free energy at fixed temperature is then expressed as:

$$F_{\hat{H}} = tr(\rho_{\hat{H}}\hat{H}) + \frac{1}{\beta}tr(\rho_{\hat{H}}\ln\rho_{\hat{H}}) \tag{3.1}$$

where $\rho_{\hat{H}}$ is the ionic density matrix of the system, which in turn can be expressed as:

$$\rho_{\hat{H}} = \frac{e^{-\beta\hat{H}}}{\mathrm{tr}\left(e^{-\beta\hat{H}}\right)}. \tag{3.2}$$

The clear problem here is that it is not clear how to diagonalize the Hamiltonian in Eq. (3.2), since it offers a cumbersome many many problem for a system of interacting oscillators. The idea would then be leveraging the analytical expression of Eq. (3.2) in the HA: we replace the true density matrix ρ with a trial one $\tilde{\rho}$, and write Eq 3.1 in functional form:

$$F[\tilde{\rho}] = tr[\tilde{\rho}H] + \frac{1}{\beta}tr[\tilde{\rho}\ln\tilde{\rho}]. \tag{3.3}$$

At this point, the Gibbs-Bogoliubov variational principle [19] states that:

$$F \leq \mathscr{F}[\tilde{\rho}], \tag{3.4}$$

where the equality holds for $\tilde{\rho} = \rho$. That is, the free energy of the ionic system can be found by minimization of the free energy functional. The self-consistent harmonic approximation (SCHA) consists in restricting the possible trial density

matrices to the equilibrium one obtained in the HA. This Hamiltonian is, in practical calculations, parametrized in terms of the vector $\mathcal{R}$ of dimension $3N_a$ and the FC matrix Φ_{IJ} of dimension $3N_a \times 3N_a$, where N_a is the number of atoms:

$$\tilde{H}_{\mathcal{R},\mathbf{\Phi}} = \sum_I \frac{p_I^2}{2M_P} + \tilde{V}_{\mathcal{R},\mathbf{\Phi}}, \tag{3.5}$$

where the potential is obviously:

$$\tilde{V}_{\mathcal{R},\mathbf{\Phi}} = \frac{1}{2}\sum_{IJ} \Phi_{IJ}(R-\mathcal{R})^I(R-\mathcal{R})^J. \tag{3.6}$$

The SCHA free energy can then be recasted as:

$$\mathcal{F}(\mathcal{R},\mathbf{\Phi}) = F_{\mathbf{\Phi}} + \langle V - \mathcal{V}_{\mathcal{R},\mathbf{\Phi}} \rangle_{\rho_{\mathcal{R},\mathbf{\Phi}}}, \tag{3.7}$$

where V is the BO energy and $\mathcal{V}_{\mathcal{R},\mathbf{\Phi}}$ is the harmonic potential in Eq. (3.6). The difference of these two quantities must be averaged over the probabilistic configuration space described by the rather practical ionic density matrix in the HA:

$$\tilde{\rho}_{\mathcal{R},\mathbf{\Phi}}(\mathbf{R}) = A_H \exp\left(-\sum_{IJ} \frac{\sqrt{M_I M_J}}{2a_\mu^2} \epsilon_\mu^I \epsilon_\nu^J (R-\mathcal{R})^I (R-\mathcal{R})^J\right). \tag{3.8}$$

Eq. (3.8) describes a Gaussian in the atomic position $\mathbf{R}$, with centroid $\mathcal{R}$, where $a_{\mu H} = \sqrt{\frac{1+2n_\mu}{2\omega_\mu}}$, ω_μ^2 and ϵ_μ^I are the phonon frequency and eigenenvector related to mode ν and atom I, of the trial FC matrix $\Phi_{IJ}/\sqrt{M_I M_J}$, n_ν is the Bose-Einstein distribution (Eq. (2.37)) and A_H is a renormlization factor. Then, $F_{\mathbf{\Phi}}$ is simply the free energy of the harmonic Hamiltonian at fixed temperature:

$$F_\Phi(T) = \sum_{\mu=1}^{3N} \left[\frac{\hbar\omega_\mu}{2} + \frac{1}{\beta}\ln\left(1 - e^{-\beta\hbar\omega_\mu}\right)\right]. \tag{3.9}$$

In order to numerically minimize the SCHA free energy in Eq. (3.7), it is of key importance to know its gradients with respect to the centroid position and FC matrix, respectively:

$$\nabla^{\alpha}_{\mathcal{R}_s} \mathcal{F}(\vec{\mathcal{R}}, \Phi, \{\vec{a}_i\}) = -\left\langle f_s^{\alpha} - f_{\mathcal{H}}^{\alpha_s} \right\rangle_{\rho_{\vec{\mathcal{R}},\Phi}}. \tag{3.10}$$

$$\nabla_{\Phi} \mathcal{F}(\vec{\mathcal{R}}, \Phi, \{\vec{a}_i\}) = -\sum_{st\alpha\beta\mu} \sqrt{\frac{M_t}{M_s}} \left(e_{\mu}^{\alpha_s} \nabla_{\Phi} \ln a_{\mu} + \nabla_{\Phi} e_{\mu}^{\alpha_s} \right) \tag{3.11}$$

$$\times \left\langle \left[f_s^{\alpha}(\vec{u}) - f_{\mathcal{H}}^{\alpha_s}(\vec{u}) \right] u_t^{\beta} \right\rangle_{\rho_{\vec{\mathcal{R}},\Phi}} e_{\mu}^{\beta_t}. \tag{3.12}$$

Eqs. 3.10 and 3.11 are of particular convenience, since they are function of quantities coming from the diagonalization of the harmonic FC matrix (eg. $e^{\alpha}_{\mu_s}$ and a_{μ}) and, in analogy with Eq. (3.7), function of averages of the BO forces f_s^{α} and of the harmonic forces $f_{\mathcal{H}}^{\alpha_s}$. By deriving Eq. (3.6) with respect to the atomic positions, the harmonic forces can be computed simply via:

$$f_{\mathcal{H}}^{\alpha_n} = -\frac{\partial \mathcal{V}_{\mathcal{R},\Phi}}{\partial R_n^{\alpha}} = -\sum_{m=1}^{N} \sum_{\beta=1}^{3} \Phi_{nm}^{\alpha\beta} u_m^{\beta}. \tag{3.13}$$

It is convenient to point out that the key ingredients for the calculation of the SCHA free energy and its gradients in Eqs. 3.7, 3.10 and 3.11 are the BO energies $\mathcal{V}_{\mathcal{R},\boldsymbol{\Phi}}$ and forces f_s^{α} over the configuration space, since they make up for the most computationally expensive part of procedure. Indeed, while he centroids $\mathcal{R}$ are defined in the UC, the trial FC matrix Φ is defined on a supercell. The averages over the configuration space can be calculated by performing *ab initio* calculations on various supercells as generated via Monte Carlo (MC) sampling of the trial ionic distribution in Eq. (3.8). The name "SSCHA" derives from the fact that the self-consistent problem is indeed solved by a stochastic approach.

On a final note, the SSCHA FC matrix at convergence can be Fourier interpolated on the reciprocal space in order to obtain the DMs and their associated frequencies through the Dyson equation (Eq. (2.30)). However, these frequencies are not physical, since they do not represent the curvature of the free energy of the real system. The SSCHA-package implements what we will refer to as

the "Bubble" correction to the self-consistent frequencies, which has non negligible contributions in strongly anharmonic materials [14] like $KTaO_3$ and $SrTiO_3$, while it is negligible in "harmonic" compounds as C-diamond, at least far from phase transitions. This correction recovers the proper physical significance of the SSCHA FC and its associated eigenvalues as the observable frequencies.

The SSCHA code evaluates the MC averages through direct *ab initio* supercell calculations. To alleviate this huge computational cost a reweighting technique is introduced (importance sampling), that allows for the simultaneous execution of several minimization steps with the same ensemble, with the price of a statistical degradation. Despite this speed-up, the computational cost of reaching well-converged results easily becomes prohibitive for systems requiring large supercells, posing a limit for large-scale samplings. Usually, and according to the goodness of the trial harmonic guess, several thousands of calculations are required in order to reach the minimum of the free energy. This poses the real bottleneck in the self-consistency loop, while the gradient descent calculations, although possibly time-consuming, are quite rapid when considering small supercells. What if the energies and interatomic forces for thousands of large supercells could be calculated by employing a machine learning (ML) model?

3.2 Machine Learned Force-Field (MLFF)

In Section 3.1 we anticipated how the SSCHA method can be sped up by the use of ML methods for the prediction of BO energies and on forces on large supercells. ML algorithms have proved to be capable of efficiently accelerating *ab initio* calculations, while preserving accuracy [20–22]. The Vienna *ab initio* simulation package (VASP) has recently implemented an on-the-fly MLFF for the execution of MD simulations, which has been proven to speed the calculation of around two orders of magnitude [23–25]. It has the advantage of performing, at the same time, the learning and training steps by targeting energy, forces and stress at each MD step. This ensures the automatized capturing of the meaningful details of the configurational space, while it is being explored during the dynamics. While useful in itself, at the end of this "on-the-fly" MD simulation,

we obtain a set of only the most representative structures, that can be used for the training of a completely different ML method. We also obtain the MLFF model itself which can be employed for any further purpose, like, in our case, the sped up of the SSCHA procedure.

It is worth to briefly describe the specifics of this particular MLFF, since it will help in the discussion of the next chapters and sections.

We first define the probability of finding an atom j at a relative position $\mathbf{r}$ from atom i as:

$$\tilde{\rho}_{ij}(\mathbf{r}) = f_{\text{cut}}(|\mathbf{r}_j - \mathbf{r}_i|)g(\mathbf{r} - (\mathbf{r}_j - \mathbf{r}_i)), \tag{3.14}$$

where f_{cut} is cut-off function which smoothly goes to zero after a certain cut-off radius R_{cut}, and g is a smoothened delta function. The probability to find any atom in $\mathbf{r}$ is thus:

$$\rho_i(\mathbf{r}) = \sum_{j \neq i}^{N_a} \tilde{\rho}_{ij}(\mathbf{r}), \tag{3.15}$$

where N_a is the number of atoms inside the sphere defined by R_{cut}. We can now define the (two-body) radial distribution function for the atom i by integrating Eq. (3.15) over the two angular coordinates:

$$\rho_i^{(2)}(r) = \frac{1}{4\pi} \int \rho_i(r\hat{\mathbf{r}})\, d\hat{\mathbf{r}}. \tag{3.16}$$

Likewise, a (three-body) angular distribution function $\rho_i^{(3)}(r, s, \theta)$, defined as the probability of finding an atom $j \neq i$ at a distance r from an atom i and another atom $k \neq j, i$ at a distance s from the same atom i, spanning an angle θ with vertex in i. At this point, $\rho_i^{(2)}(r)$ and $\rho_i^{(3)}(r, s, \theta)$ are expanded in Legendre polynomials and spherical Bessel functions in order to treat the problem in the expansion coefficients:

$$\mathbf{x}_i^{(2)^T} = (c_1^i, c_2^i, \ldots) \tag{3.17}$$

$$\mathbf{x}_i^{(3)^T} = (p^i_{110}, p^i_{111}, \ldots, p^i_{120}, p^i_{121}, \ldots), \tag{3.18}$$

$$\mathbf{x}_i^T = \left(\mathbf{x}_i^{(2)^T}, \mathbf{x}_i^{(3)^T}\right). \tag{3.19}$$

The total BO energy of the system of N_a atoms is then approximated as a sum over the local energy U_i:

$$U = \sum_{i=1}^{N_a} U_i[\rho_i^{(2)}, \rho_i^{(3)}] \rightarrow \sum_{i=1}^{N_a} F(\mathbf{x}_i). \tag{3.20}$$

At this point, $F(\mathbf{x}_i)$ is approximated as a weighted sum of Gaussian Kernel functions $K(\mathbf{x}_i, \mathbf{x}_{i_B})$ centered at reference points $\{\mathbf{x}_{i_B} | i_B = 1, ..., N_B\}$:

$$F(\mathbf{x}_i) = \sum_{i_B=1}^{N_B} w_{i_B} K(\mathbf{x}_i, \mathbf{x}_{i_B}). \tag{3.21}$$

.

the reference configurations $\mathbf{x}_{i_B}$ are chosen from ab initio MD calculations, and the weights w_{i_B} optimized in order to reproduce the target BO energies, forces and stress tensor components, extracted from the same MD simulations.

In a concrete scenario, the MD executes its first time steps by *ab initio* calculations. After a certain number of gathered local configurations, the forces and energies are predicted, along with the associated Bayesian errors (more info in Ref. [23]). If the uncertainties fall above a certain threshold, an *ab initio* calculation is performed, and forces and energies for that configuration are stored, thus moving to the next time frame; otherwise, the predicted energies and forces are taken for good and used to generate the next positions in the simulation. The name "on-the-fly MD" comes from the choice of handling the learning and training phases simultaneously. In that, the MLFF method implemented in VASP differs from the other ML methods adopted in solid state Physics. The most common workflows rely on pre-existing datasets for the learning phase, but in most cases a new dataset has to be generated (mostly from MD runs) in order to have control on the precision on energies and forces at the *ab initio* level. In that,

an "on-the-fly" approach is particularly suitable, since it drastically reduces the time for dataset creation, while keeping its quality.

The weights gathered at the end of a successful simulation, define a MLFF model that can be applied to problems beyond the mere MD. A MLFF trained at a suitable supercell volume can indeed be applied to the problem of finding the BO energies and forces in the SSCHA free energy and associated gradients of Eqs. 3.7, 3.10 and 3.11, as long as the configurational space spanned during the MD simulation is comparable to the one required by the SSCHA. The MC configuration sampling at a certain target temperature and supercell dimension defined by the ionic density distribution can be covered by running an on-the-fly MD around the temperatures of interest. Anyways, a validation check can be performed, for example, by calculating the root mean square error (RMSE) on the energies predicted *ab initio* E^{DFT} and by MLFF E^{MLFF} on N_V randomly extracted configurations, via:

$$\text{RMSE} = \sqrt{\frac{1}{N_V}\sum_{i=1}^{N_V}(E_i^{DFT} - E_i^{MLFF})^2}. \tag{3.22}$$

At the price of a few hundred *ab initio* supercell calculations during the on-the-fly MD, we can spare several thousands of calculations in SSCHA. The integration described in this chapter has been adopted from the first stages of the dissertation work and used for obtaining the results reported and discussed in the following chapters.

CHAPTER 4

Phonon Anharmonicity in $KTaO_3$

In this chapter we delve into the nature of the QPE state of $KTaO_3$, which exhibits notable lattice anharmonicity even close to the absolute zero temperature. Much of the discussion and analysis presented in this chapter are derived and condensed from the manuscript and supplementary materials of my published work [26].

Section 4.1 exposes the problem of quantum paraelectricity and how it is related a suppressed phase transition mediated by a specific transversal optical (TO) phonon mode. The necessity of a full quantum and anharmonic treatment is required in order to predict the stability of $KTaO_3$ at low temperatures, and in order to predict the temperature evolution of its sensible vibrations.

The MLFF+SSCHA workflow and its practical implementation in the case of $KTaO_3$ is explained in Section 4.2, where the technical details of the *ab initio* calculations are described.

In Section 4.3 we argue the goodness of the MLFF by reporting its suitability in describing the PES and in recovering the phonon dispersion both at the HA level and at the SSCHA level on small supercells. The calculations can then be attempted on bigger supercells in order to obtain better prediction of the temperature evolution of the soft TO mode.

The modeling of the antiferrodistortive (AFD) phase transition and the low temperature QPE state in $SrTiO_3$ is finally presented in Section 4.3.1, in order to prove the validity of the workflow and shine a light on the similarities between the two materials. Furthermore, in Section 4.3.2 we present some preliminary

results on the FE phase transition in $KTaO_3$ as a function of uniaxial strain.

Most of the results reported in this Chapter have been published as:
[26]: L. Ranalli, C. Verdi, L. Monacelli, G. Kresse, M. Calandra and C. Franchini, "Temperature Dependent Anharmonic Phonons in Quantum Paraelectric $KTaO_3$ by First Principles and Machine Learned Force-Fields", Advanced Quantum Technologies, 6, 2200131 (2023).
Conception, execution and analysis done independently and under guidance of my supervisor C. Franchini and C. Verdi, and technical support of M. Calandra and L. Monacelli for the SSCHA calculations in DFT.

In Section 4.3.1 we summarize a portion of the study published as:
[27]: C. Verdi, L. Ranalli, C. Franchini, G. Kresse , "Quantum paraelectricity and structural phase transitions in strontium titanate beyond density functional theory", Physical Review Materials, 7, L030801 (2024).
Conception, analysis and execution done by C. Verdi. Technical workflow developed by L. Ranalli.

4.1 Introduction

The QPE phase emerges due to the suppression of the FE transition at low temperatures, driven by quantum fluctuations. This phenomenon is exemplified in materials like $KTaO_3$ and $SrTiO_3$, where the frequency of the polar TO soft phonon mode does not become imaginary as the temperature decreases, contrary to the behavior observed in typical FE systems such as $BaTiO_3$. Instead, the phonon frequency stabilizes at a finite value [28, 29]. This behavior correlates with an anomalous temperature dependence of the inverse dielectric constant at low temperatures, deviating from the classical Curie-Weiss law [30–32] (see **Figure 4.1a**).

$SrTiO_3$ and $KTaO_3$, which are situated at the boundary of the FE phase near the so-called quantum critical point (QCP)[32, 33], can be induced to enter the FD region through minimal external perturbations such as strain[34], hydrostatic pressure [35, 36], or isotopic substitution [37] (see Figure 4.1b). For this reason, these materials are also known as incipient FDs. The precise mechanism behind the stabilization of the long-wavelength **q**=0 FE TO phonon mode (ω_{FE}) remains an open question [38]. However, it is generally agreed that the anharmonic coupling between ωFE and the quantum lattice oscillations at low temperatures plays a key role in stabilizing ω_{FE} at helium temperatures in QPE systems [39–41].

According to the Landau model of displacive phase transitions, the QPE phase represents a crossover state between the conventional FE regime, which is associated with a double-well PES, and the standard parabolic PE behavior. This transition introduces quartic contributions [42] that flatten the free energy profile (Figure 4.1c). In QPE materials, quantum fluctuations and low-temperature anharmonic effects stabilize the QPE phase, establishing it as the system's true ground state, which is highly susceptible to perturbations. The phonon and dielectric response in $SrTiO_3$ and $KTaO_3$ have been extensively documented [32, 43], and the data has been interpreted through various phenomenological models. These models include adaptations of Slater's classical framework [44], such as the Barrett [39] and Vendik [45] models [31], as well

as models inspired by the Ginzburg-Landau-Wilson framework, such as the ϕ^4 quantum field model [46, 47]. Computationally, path-integral MC simulations using model Hamiltonians have shed light on the role of quantum fluctuations and nonlinear response functions in suppressing the FE transition [48–50]. A microscopic understanding of the FE soft mode and its nonlinear dielectric susceptibility at low temperatures remains a challenging goal.

This Chapter introduces an efficient protocol for calculating the temperature-dependent frequency $\omega_{FE}(T)$ of the soft phonon mode and its associated dielectric response using first-principles methods that fully incorporate quantum and anharmonic effects. The case of $KTaO_3$ is chosen as a representative system because it retains the ideal cubic perovskite structure over a wide temperature range down to the QPE regime, thereby avoiding the complexities introduced by structural phase transitions. A summary of the more intricate case of $SrTiO_3$ is provided in Section 4.3.1.

To incorporate quantum and thermal ionic fluctuations, we employ the SSCHA method, which was introduced in Section 3.1. This approach is combined with the on-the-fly MLFF method presented in Section 3.2 to efficiently and rapidly explore the stochastic space. This approach offers a significant advantage over other methods, such as inferring effective FCs from *ab initio* MD trajectories [51].

4.2 SSCHA+MLFF workflow

The approach hereby described employs the SSCHA framework, which necessitates ground state energies and interatomic forces calculated on a supercell of the material under investigation. The specific procedure for $KTaO_3$ is organized into the following steps:

1. The trial harmonic DM (refer to Section 2.3) is determined using a $2\times2\times2$ supercell derived from the cubic UC of $KTaO_3$, with the experimental lattice parameter set to 3.9842 Å [41].

2. *Ensembles generation* and the self-consistent SSCHA loop are carried out

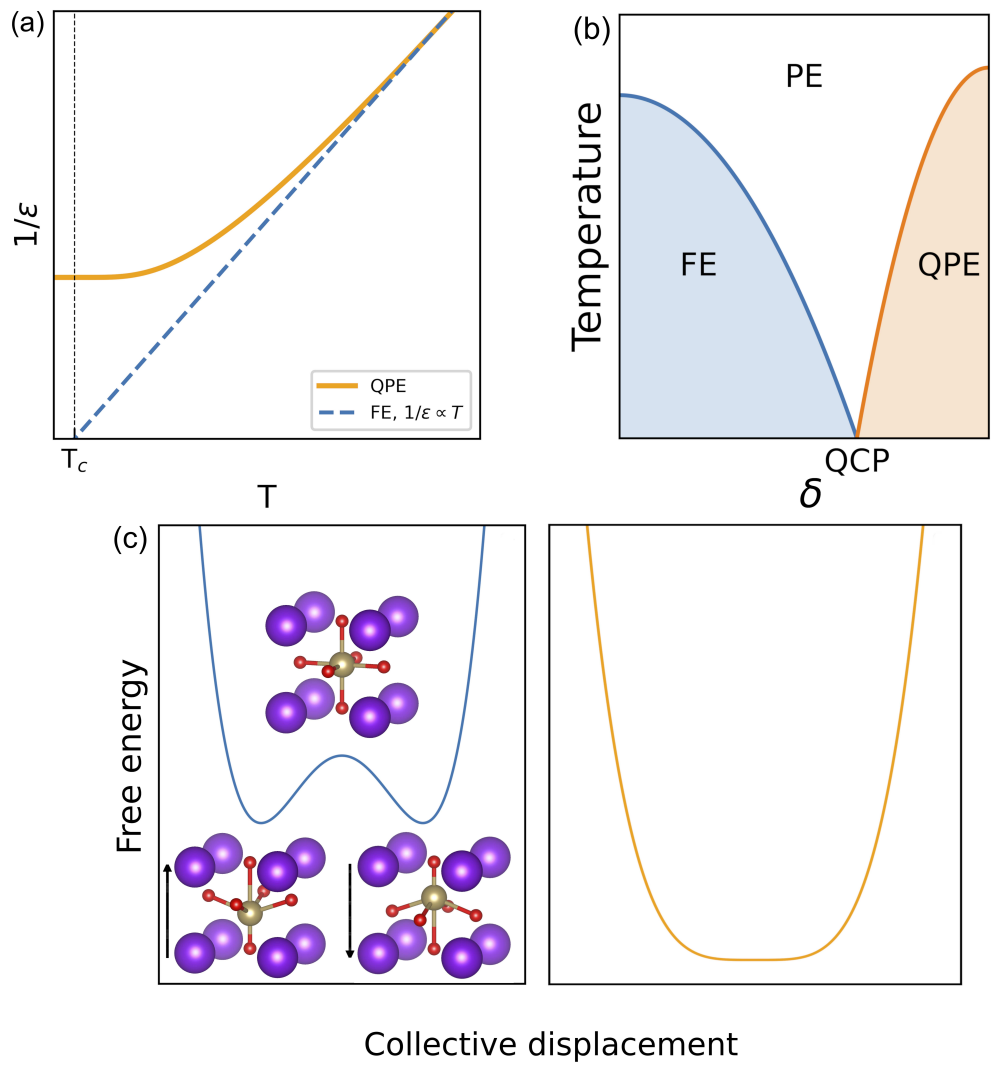


Figure 4.1. (a) Schematic trend of the inverse dielectric constant as a function of temperature in the FE and QPE phase. In the FE phase $1/\epsilon$ follows the characteristic linear behavior (dashed blue line) leading to a divergence of ϵ at a critical temperature T_c where the FE transition occurs. In a QPE (orange solid line), in the proximity of T_c the onset of quantum anharmonicity breaks down the linear regime establishing the QPE state. (b) Qualitative phase diagram of the crossover between the FE and QPE phases as a function of a quantum tuning parameter δ; above a certain critical temperature, marked by the thick lines, the system lies in the PE region. At 0 K, variations of the quantum tuning parameter (due, for example, to strain, hydrostatic pressure or isotopic substitution) drive the FE-to-QPE transition across the QCP. (c) Quantum free energy as a function of a collective atomic displacement in FE (left) and QPE (right) regimes in an ABO_3 crystal. The soft FE phonon induces a FE displacement of the BO_6 octahedron (insets) which lowers the quantum free energy forming the typical double-well profile (left). In a QPE regime (right), the FE transition is inhibited due to quantum fluctuations and phonon anharmonicity. The inclusion of the anharmonic self-energy contributions at 0 K in the SSCHA calculations flatten the free energy removing the FE minima and establishing the QPE state.

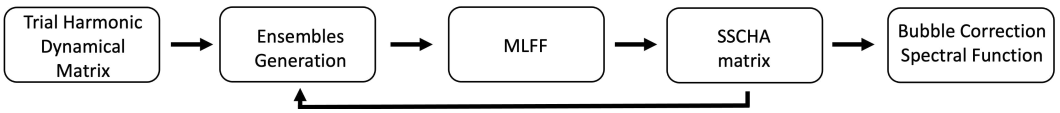


Figure 4.2. Sketch of the MLFF+SSCHA workflow. A first guess of the harmonic DM is calculated at the DFT level or using the MLFF and employed by SSCHA in the generation of the first population (ensembles generation). The energies and forces for the displaced ensemble are computed employing the MLFF, and the gradient of the free energy is minimized in SSCHA (SSCHA matrix). The obtained SSCHA dynamical matrices are subsequently employed for the generation of the second population and the loop continues until convergence (arrow). After reaching convergence, the bubble correction at both static and dynamical levels can be calculated.

through free energy minimization using a FC gradient descent approach, where both the atomic positions and volume remain constant. The self-consistency loop at 0K, illustrated in Fig.4.3, employs 15000 ensembles, with the final 5000 of these also utilized for calculating the bubble correction.

3. The acceleration of the stochastic MC sampling is achieved through the implementation of the MLFF, which serves as the central component of the methodology. The MLFF is trained dynamically via MD simulations conducted on a $3\times3\times3$ Monkhorst-Pack k-point grid. These MD runs are performed at progressively higher temperatures, with each temperature step involving 50000 sampling steps and a time increment of 2 fs. The final atomic configuration at each temperature serves as the initial structure for the subsequent, higher-temperature run. A Langevin thermostat with a friction coefficient of $10\,\mathrm{ps}^{-1}$ is applied to each atomic species [52]. For the descriptors capturing the local atomic environments within the MLFF, the cut-off radius for two- and three-body atomic density distributions is set to 6 Å, with a Gaussian broadening parameter of 0.3 Å (see Section 3.2 for further details). Equal weight is assigned to both descriptors.

An visual schematics of the workflow is shown in Figure 4.2.

The computational workflow integrates VASP[53, 54] with SSCHA and the PHONOPY phonon package [55, 56]. All DFT calculations are carried out at the meta-generalized gradient approximation (GGA) level, employing the Strongly Constrained and Appropriately Normed (SCAN) functional [57] along with

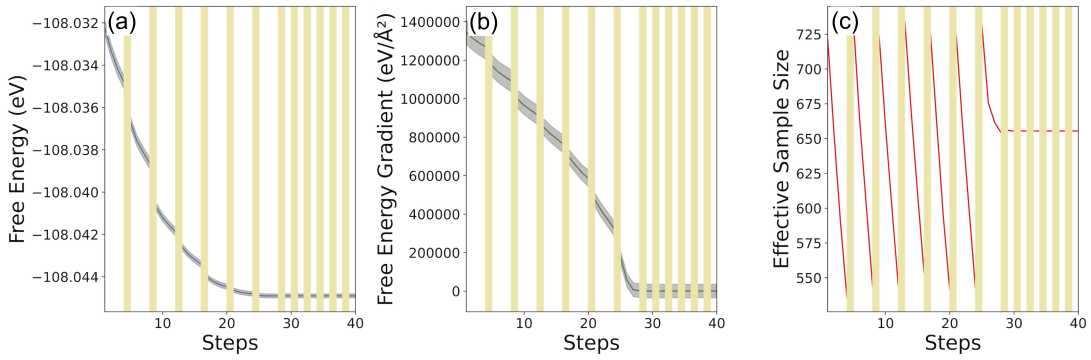


Figure 4.3. Convergence of the SSCHA minimization for a 2×2×2 supercell of $KTaO_3$ at 0K. (a) Free energy per unitcell during the minimization. The grey shaded area denotes the stochastic error associated. (b) Free energy gradient with respect to the FC. (c) Effective sample size degradation with respect to the 800 ensembles used at the start of the minimization of each population. In this example, the effective sample size approached its lower limit of 500 ensembles, and thus 13 populations were needed (yellow bands).

projector augmented wave (PAW) pesudopotentials (PPs) [58]. A plane-wave energy cutoff of 800 eV is used for all calculations.

The computational pipeline establishes a seamless interface between VASP, PHONOPY, and SSCHA, enabling an efficient workflow. Additionally, a MLFF is employed to compute the energies and forces of the ensembles generated within the SSCHA framework [26].

4.3 Quantum Paraelectric state

To evaluate the accuracy of our MLFF, we examine the ground-state energy as a function of the FE displacement, comparing it to the results of direct DFT calculations. The corresponding results are presented in Figure 4.4a. As anticipated, within the HA framework, DFT identifies the cubic structure as a saddle point, exhibiting meta-stability with respect to opposite polar displacements of the O and Ta ions within the TaO_2 plane, as illustrated in the inset of Figure 4.1c.

This behavior arises from the omission of anharmonic effects linked to the O-Ta-O polar vibration, a point that will be addressed in the subsequent section. More specifically, this instability is governed by two degenerate modes at the Γ point, namely TO_1 and TO_2. The TO_1 soft mode corresponds to a vibrational motion along the crystallographic x-axis, while the TO_2 mode is symmetry-equivalent, describing displacements along the z-axis.

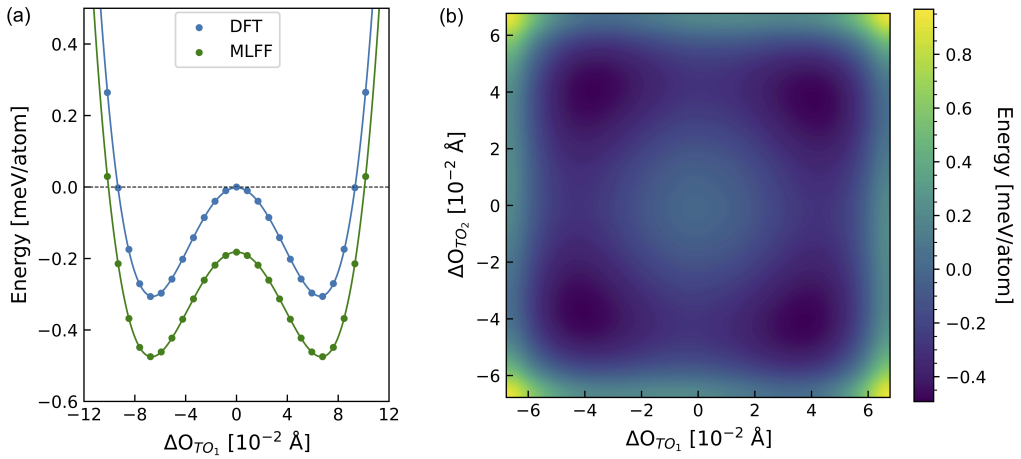


Figure 4.4. Calculated FE instability. (a) Electronic ground state energy as a function of the O displacement from the equilibrium position along the TO_1 unstable soft mode. The saddle point in the DFT calculation corresponds to the ideal cubic structure and represents the reference zero. The MLFF prediction is in very good agreement with the *ab initio* results. (b) MLFF prediction of the 2D energy landscape as a function of the displacements involved in both the TO_1 and TO_2 degenerate modes. Calculations performed on a $3\times3\times3$ supercell.

The double-well energy profile depicted in Figure 4.4a demonstrates that the displacive nature of the spurious FE phase transition in $KTaO_3$ is accurately reproduced by the MLFF, both in qualitative and quantitative terms. According to DFT calculations, the energy barrier reaches $-0.306\,\mathrm{meV/atom}$ at an O displacement of 0.059 Å along the TO_1 direction. In comparison, the MLFF predicts a similar energy barrier of $-0.293\,\mathrm{meV/atom}$ at a slightly larger displacement of 0.068 Å.

Due to the degeneracy of the TO_1 and TO_2 modes, any linear combination of their corresponding eigenvectors forms a valid solution for the non-FE phase. This symmetry is illustrated in Figure 4.4b, which presents a 2D map of the ground-state energy resulting from the combined influence of both FE modes, as computed using the MLFF. The 2D map reveals the presence of a 4-fold degenerate energy minimum at $-0.493\,\mathrm{meV/atom}$, relative to the saddle point at (0,0).

After verifying the MLFF's precision in reproducing the energy-displacement profile, we shift our focus to its capability to accurately compute the free energy Hessian with respect to atomic positions. This Hessian is a crucial quantity, as it enables the extraction of anharmonic contributions to the phonon frequencies.

The onset of a FE transition as a function of temperature can be identified by monitoring the eigenvalues of the free energy Hessian, normalized by the square root of the mass matrix — a quantity referred to as the positional free energy Hessian (see Equation 51 in Ref. [14]). The presence of an imaginary eigenvalue in this positional free energy Hessian serves as a clear indicator of a FE transition.

Figure 4.5a presents the anharmonic phonon dispersions, which are derived from the eigenvalues of the positional free energy Hessian within the SSCHA at 0 K. These calculations are performed using DFT on a 2×2×2 supercell, incorporating the self-energy correction in the free energy Hessian [14]. The phonon self-energy is evaluated using the Bubble approximation, which captures the dominant three-phonon scattering processes. For comparison, the harmonic phonon dispersion obtained from DFT is also shown.

Consistent with the energy profile in Figure 4.4a, the lowest-energy TO phonon mode, corresponding to the degenerate FE modes TO_1 and TO_2 at the Γ point, exhibits instability across a significant portion of the BZ, which is at odds with experimental observations [43]. When quantum anharmonicity is introduced through the SSCHA method, this 0 K FE instability is eliminated. Notably, the anharmonic correction has a negligible effect on all other phonon modes.

For the TO_1 mode at the Γ point, the computed eigenvalue of the positional free energy amounts to 38.1 cm^{-1}. The contribution of the bubble term to the fully converged self-consistent DM is $-40.3\,cm^{-1}$.

To further enhance the calculation of phonon renormalization and improve the stochastic sampling of the configuration space, we integrate the MLFF with the SSCHA in an on-the-fly manner. The structure and technical specifics of this protocol are outlined in Section 4.2.

The results are illustrated in Figure 4.5b, which compares the phonon dispersion obtained from DFT+SSCHA with that from MLFF+SSCHA. For this specific comparison, the MLFF is trained on a compact 2 × 2 × 2 supercell — the same supercell size used for the DFT+SSCHA calculations. For the computation of finite-temperature properties, however, a larger 3×3×3 supercell is utilized

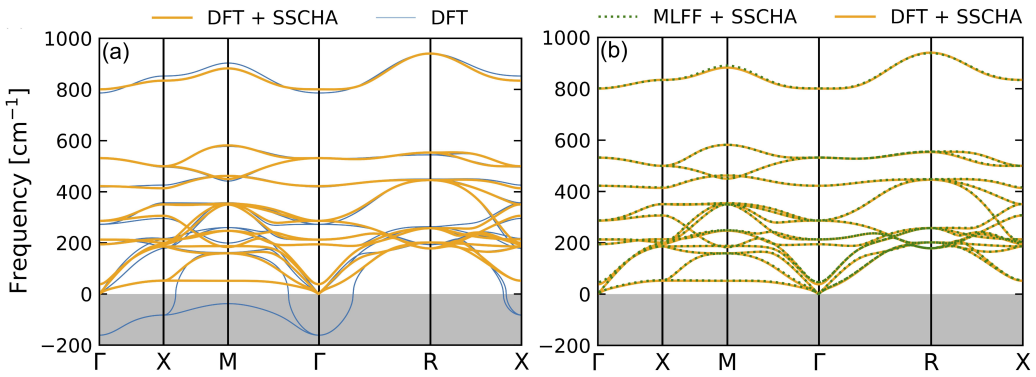


Figure 4.5. Calculated 0 K harmonic and anharmonic phonon dispersion. (a) In DFT (blue lines), the harmonic phonon dispersion exhibits unstable FE TO_1 and TO_2 degenerate phonon modes at Γ. Within DFT+SSCHA (solid orange lines), the inclusion of the bubble term (anharmonic effects) renormalizes the unstable modes, while keeping the other branches unaffected. (b) Comparison between DFT+SSCHA and MLFF+SSCHA (green dotted lines) anharmonic phonon spectra. Calculations performed on a 2×2×2 supercell.

along with an MLFF trained on larger supercells, as detailed in Section 4.2.

The agreement between the DFT+SSCHA and MLFF+SSCHA results is excellent across the entire phonon spectrum. This includes the TO_1 mode at the Γ point, where the computed frequency is 46.6 cm^{-1}, and the bubble correction is $-37.2\,cm^{-1}$. These values are very close to those obtained using the DFT+SSCHA method. For comparison, experimental neutron scattering data at 20 K yield a lower TO_1 mode frequency of 24.9 cm^{-1} at Γ [43], which is consistent with our static dispersion calculations.

To introduce a higher level of complexity, we now incorporate finite temperature effects, which play a crucial role in describing temperature-driven phase transitions and present a significant challenge for first-principles approaches. Investigating the temperature dependence of the soft mode using *ab initio* SSCHA calculations is computationally demanding, as it requires the use of numerous supercells to obtain well-converged results over a range of temperatures.

To overcome this challenge, we utilize a $3 \times 3 \times 3$ supercell and train a corresponding MLFF to efficiently sample the configuration space up to 700 K. This approach results in a higher bubble-term corrected soft mode frequency of 59.6 cm^{-1}, compared to 46.6 cm^{-1} for the smaller 2×2×2 supercell. The bubble self-energy correction, which acts antagonistically, introduces a smaller correction of $-11.2\,cm^{-1}$ to the virtual phonons calculated via SSCHA. Moreover,

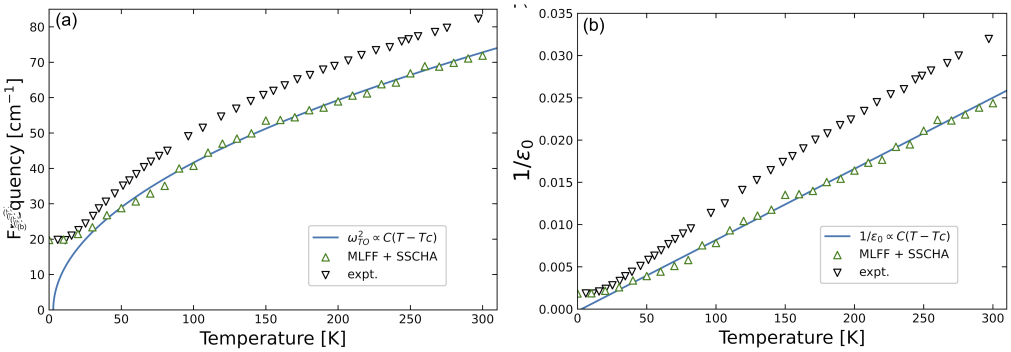


Figure 4.6. Temperature evolution of the TO_1 Γ-point frequency (a) and of the inverse of the dielectric constant (b). In (a), inelastic neutron scattering measurements [59] (black empty triangles) and MLFF+SSCHA calculations with the inclusion of the bubble term are shown. The computed frequencies are shifted down by 34.7 cm^{-1} to match the experimental low temperature soft mode frequency.

the bubble term correction applied to the converged DM yields a negative shift of 15.5 cm^{-1} for the soft mode at 300 K. Notably, this contribution remains almost independent of temperature.

The temperature dependence of the soft mode, as predicted by the MLFF, is displayed in Figure 4.6, alongside low-temperature experimental data from Ref. [59]. The MLFF predictions accurately capture the experimental trend, underscoring the capability of the computational framework. This integrated approach — combining electronic structure methods, MC sampling, and ML — offers a powerful means to access thermodynamic regimes that were previously beyond reach for conventional first-principles calculations.

Our results successfully reproduce the characteristic plateau observed below 30 K, consistent with the theoretical trend presented in Figure 4.1a. This agreement highlights the framework's capacity to capture the essential role of anharmonic effects in establishing the QPE state.

Using the Lydanne-Sachs-Teller (LST) relation [60], expressed as $\frac{\omega^2_{\mathrm{LO}}}{\omega^2_{\mathrm{TO}}} = \frac{\epsilon_0}{\epsilon_\infty}$ which links the optical phonon frequencies to the static (ϵ_0) and high-frequency (ϵ_∞) dielectric constants (above phonon but below electronic energy scales), we analyze the temperature dependence of the dielectric constant. Assuming that the temperature dependence of ϵ_0 arises solely from the temperature dependence of the TO mode, we plot the inverse dielectric constant $1/\epsilon_0$ as a function of temperature in Figure 4.6b. This plot is presented alongside experimental data for comparison.

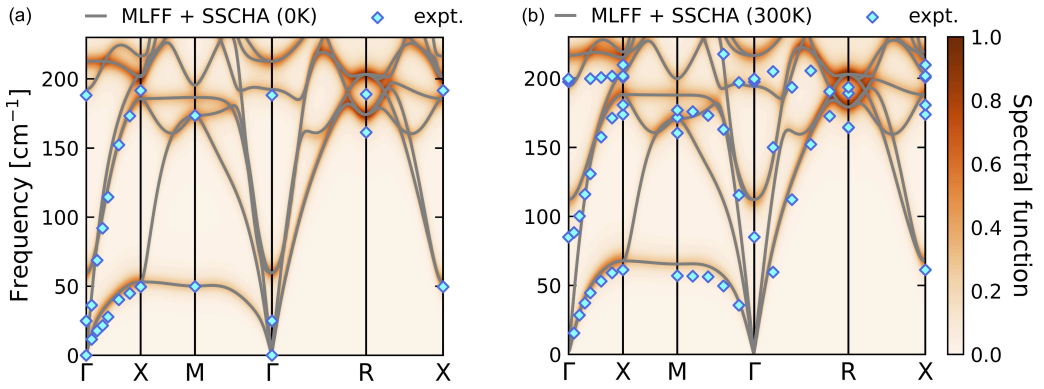


Figure 4.7. Color plot of the normalized phonon spectral function along the high symmetry path at (a) 0 K and (b) 300 K. In both cases the maxima of the spectral function in darker red coincide with the static dispersion (full lines). The results are compared with the experimental data at 20 K and 296 K [43] (diamonds). Calculations performed on a 3×3×3 supercell.

For the calculations, we employ values of 4.64 for ϵ_∞ and 212.7 cm^{-1} for the longitudinal optical (LO) phonon mode ω_{LO}. The frequency data are fit using a square-root function, which corresponds to a linear fit of the temperature-dependent inverse dielectric constant. This fit clearly illustrates the breakdown of the classical regime below 30 K, where quantum nuclear motion, coupled with anharmonic effects, becomes the dominant factor governing the system's behavior.

To conclude, we compute the phonon spectral function, which incorporates dynamical effects not captured by the static phonon spectra displayed in Figure 4.5. The spectral function's peaks correspond to the phonon quasi-particle (QP) observable in inelastic neutron scattering experiments.

Figures 4.7a and 4.7b display the phonon spectral function at 0 K and 300 K, respectively, calculated for a $3 \times 3 \times 3$ supercell along a high-symmetry k-path. The computed results are compared with experimental data from Ref. [43] as well as with the corresponding static dispersions.

It is observed that the maxima of the spectral function align with the static dispersions for the 3×3×3 supercell at both temperatures. In this scenario, the dynamical Bubble correction does not significantly alter the static dispersions, nor does it give rise to additional satellite excitations. The agreement with experimental measurements is notably good, although, as mentioned earlier, the

soft TO mode is slightly overestimated by a few tens of cm^{-1}.

4.3.1 Comparison with $SrTiO_3$

The workflow proposed in Section 4.2 is also suitable for describing the QPE state and the phase transition temperature in $SrTiO_3$. Details on this study can be assessed in Ref. [27]. Here, a summary of the results is presented for completeness and in preparation for the mobility calculations of Chapter 7.

As anticipated in Section 4.1, $SrTiO_3$ is cubic down to 105 K, at which temperature it transitions to the tetragonal phase: while approaching the critical temperature, the so called AFD mode softens progressively around the $R = (0.5, 0.5, 0.5)$ point in reciprocal space. By lowering the temperature down to 0 K experimental data show a softening of yet another TO mode, the Γ-point FE mode. As in $KTaO_3$, a frequency plateau is observed, thus signaling the presence of a QPE incipiency.

In Figure 4.8, the AFD and FE mode temperature behavior is calculated using SSCHA and MLFFs trained with on-the-fly MDs at the Perdew-Burke-Ernzerhof revised for solids (PBEsol), regularized Strongly Constrained and Appropriately Normed (rSCAN) and Random phase approximation (RPA) level. rSCAN has the best performance in predicting the frequency of the AFD mode and thus phase transition critical temperature, while RPA excels on the Γ-point FE mode. Predictably, and in line with literature results for $KTaO_3$ and $SrTiO_3$, PBEsol tends to predict very hard phonon frequencies thus being not suitable in strongly anharmonic materials. In view of the mobility calculations for the cubic phase of $SrTiO_3$ (above 105 K) reported in Chapter 7, the phonon dispersion predicted by RPA is deemed to be the most suitable.

4.3.2 Preliminary results on strained $KTaO_3$

The workflow exposed in this Chapter can be swiftly extended to materials under varying pressure/strain conditions. In Section 4.3 we have seen how the QPE state of $KTaO_3$ is very delicate and can be easily overcame in favour of a FE phase transition and the development of a net lattice polarization. Predicting the

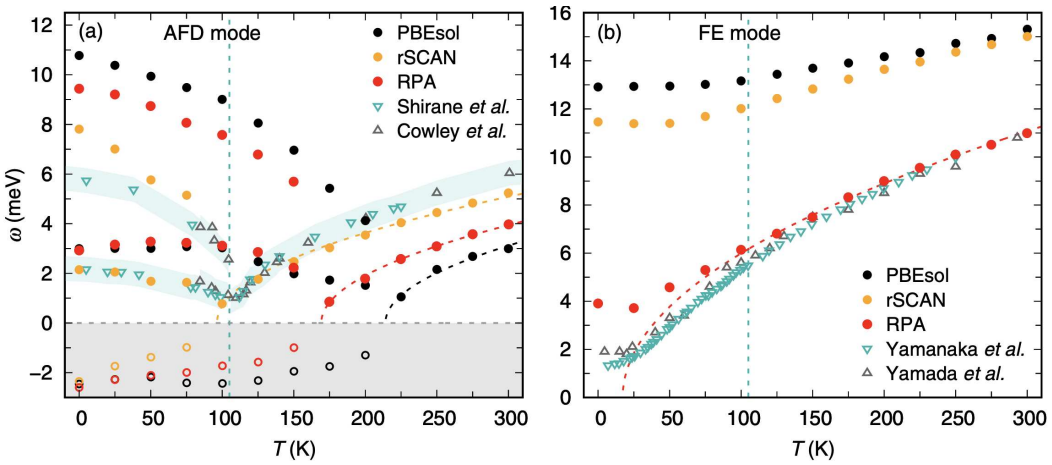


Figure 4.8. AFD phase transition and quantum paraelectrcity in $SrTiO_3$. (a) Temperature dependence of the AFD mode calculated using MLFFs trained on PBEsol (black), rSCAN (orange) and RPA (red). The empty symbols in the negative frequency region represent imaginary phonons obtained when the symmetry of the structure is kept cubic at each temperature, and the shaded regions are a guide to the eye. (b) Temperature dependence of the FE mode calculated using the same MLFFs. In (a) and (b), experimental measurements are also reported. The dashed vertical lines indicate the experimental AFD transition temperature, and the dashed curves are Curie-Weiss fits.

critical strain at which $KTaO_3$ enters the FE state can be indeed be attempted in the HA, but, as noted in the previous sections, could lead to remarkable errors due to the inability, first of all, to capture the QPE state.

The SSCHA+MLFF workflow is indeed a viable solution to these limitations, offering the opportunity of calculating both the critical strain at varying temperatures and, vice versa, the critical temperature T_C at varying strain conditions. In the collaborative work currently curated by MSc. Zhu Yu, we aim at accurately modeling the critical conditions for phase transition in $KTaO_3$, and the precise FE displacements developed, along wih the associated polarization profile, for uniaxial and biaxial strain conditions. The first step requires the enrichment of the MLFF dataset previously acquired on cubic $KTaO_3$, by running additional MD simulations under strain.

We find that an uniaxial strain induces polarization along the axis of strain via inversion symmetry breaking: the Ta and O atoms displace vertically but in opposite directions, thus developing a net dipole. In Figure 4.9a we report trend for the FE distortion intensity for fixed temperatures and as a function of uniaxial strain.

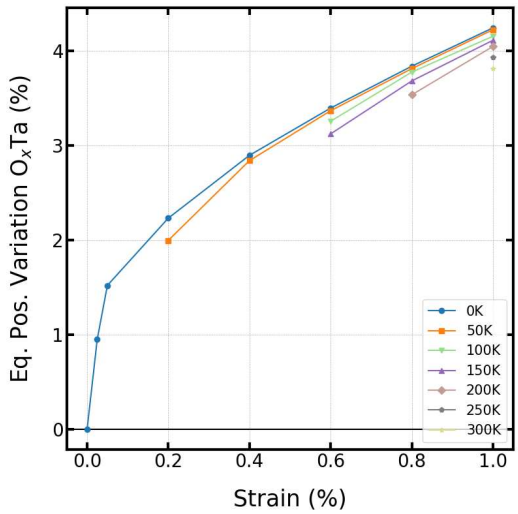


Figure 4.9. Evolution of the FE phase transition in $KTaO_3$ as a function of uniaxial strain (left), for temperatures between 0 K and 300 K. The intensity of the FD distortion is quantified as the increase in distance between one of the two O atoms along the x-axis and the Ta atom. The percentile increase is to be taken with respect to the distance in the PE state (inversion center) which is half strained lattice parameter.

CHAPTER 5

Electron-phonon coupling with phonon anharmonicity

In Chapter 3 we have proposed a workflow for assessing phonon anhamonicity through the use of the SSCHA accelerated by MLFFs for the calculations. In this chapter, we take a step back and recall how electron-phonon mediated phenomena are treated in the standard theory, which leverages the use of the HA approximation for the ionic motion.

In Section 5.1 we sum up the base of the theory of electron-phonon coupling from first principles and its successes in predicting macroscopic properties. I describe the practical implementation of the theory in most state-of-the-art codes, which limits the treatment to the first order of interaction and employs Wannier interpolation in order to reach accurate results. At the end of the section, we explain when these approaches can fail due to the effect of anharmonic lattice vibrations, and thus propose its integration in the linear electron-phonon coupling theory.

In Section 5.2 the main concepts behind the BTE for modeling charge carrier transport are introduced, since they will later be employed for mobility calculations in Chapter 7.

In Section 5.3 we briefly introduce the concept of thermodynamic averages for the calculation of electronic observables through MC sampling over the bosonic configurational space. In particular, we describe the recently proposed method of the "ZG displacements" (special displacement method (SDM)), which

allows for a one-shot calculation of the thermodynamic observables, in a "mean value theorem" fashion. This method is employed in the work presented in Chapter 6 and Chapter 7.

Finally, in Section 5.4 we report the main ideas and pivotal quantities in the DFPT treatment of the polaron problem, which will be useful in Chapter 8.

5.1 Electron-Phonon Coupling

The concept of "electron-phonon" coupling dates back to 1929, when Bloch discussed the solution of the Schröedinger equation in a periodic potential. The standard Hamiltonian for a coupled electron-phonon system relies on three important assumptions: i) the electronic system can be described as in terms of well-defined quasi-particle excitations, ii) lattice vibrations can be treated in the HA, and iii) the adiabatic approximation (what we have previously called BO approximation) holds. Said Hamiltonian takes the form [61]:

$$\hat{H} = \sum_{n\mathbf{k}} \epsilon_{n\mathbf{k}} \hat{c}^{\dagger}_{n\mathbf{k}} \hat{c}_{n\mathbf{k}} + \sum_{\mathbf{q}\nu} \hbar\omega_{\mathbf{q}\nu} (\hat{a}^{\dagger}_{\mathbf{q}\nu} \hat{a}_{\mathbf{q}\nu} + 1/2) \tag{5.1}$$

$$+ N_p^{-1/2} \sum_{\substack{\mathbf{k},\mathbf{q} \\ mn\nu}} g_{mn\nu}(\mathbf{k},\mathbf{q}) \hat{c}^{\dagger}_{m\mathbf{k}+\mathbf{q}} \hat{c}_{n\mathbf{k}} (\hat{a}_{\mathbf{q}\nu} + \hat{a}^{\dagger}_{-\mathbf{q}\nu}) \tag{5.2}$$

$$+ [N_p^{-1} \sum_{\substack{\mathbf{k},\mathbf{q},\mathbf{q}' \\ mn\nu\nu'}} g^{DW}_{mn\nu\nu'}(\mathbf{k},\mathbf{q},\mathbf{q}') \hat{c}^{\dagger}_{m\mathbf{k}+\mathbf{q}+\mathbf{q}'} \hat{c}_{n\mathbf{k}} \tag{5.3}$$

$$\times (\hat{a}_{\mathbf{q}\nu} + \hat{a}^{\dagger}_{-\mathbf{q}\nu})(\hat{a}_{\mathbf{q}'\nu'} + \hat{a}^{\dagger}_{-\mathbf{q}'\nu'})], \tag{5.4}$$

where the first and second terms describe the separate electron and phonon systems, the third term describes the electron-phonon coupling at the first order in the atomic displacements [61] and the fourth term (Debye-Waller (DBW) term) is the second order one. $\epsilon_{n\mathbf{k}}$ is the single-particle eigenvalue of an electron of band index n and momentum $\mathbf{k}$, $\omega_{\mathbf{q}\nu}$ is the frequency for phonon branch ν and momentum $\mathbf{q}$, N_p is the number of UCs in the Born-von-Kármán (BvK) supercell. Lastly, $g_{mn\nu}$ and $g^{DW}_{mn\nu\nu'}$ represent the coupling strength (electron phonon matrix elements).

While the first two terms of Eq. (5.1) can be readily computed in DFT/DFPT, the real complexity comes from the electron-phonon coupling tensors. First things first, it is possible to establish a connections between the Kohn-Sham operator of Eq. (2.16) and Eq. (5.1):

$$\hat{H}_e = \sum_{n\mathbf{k},n'\mathbf{k}'} \langle \psi_{n\mathbf{k}} | \hat{H}^{KS} | \psi_{n'\mathbf{k}'} \rangle \hat{c}^{\dagger}_{n\mathbf{k}} \hat{c}_{n'\mathbf{k}'} = \sum_{n\mathbf{k}} \epsilon_{n\mathbf{k}} \hat{c}^{\dagger}_{n\mathbf{k}} \hat{c}_{n\mathbf{k}}. \tag{5.5}$$

The third term in Eq. (5.1), which we will refer to as $\hat{H}_{ep}$, is related to the first order expansion of the KS potential V^{KS} in the atomic displacements $\Delta\tau_{\kappa\alpha p}$ from their equilibrium positions $\Delta\tau_{\kappa\alpha p}$:

$$V^{KS}(\{\tau_{\kappa p}\}) = V^{KS}(\{\tau^0_{\kappa p}\}) + \sum_{\kappa\alpha p} \frac{\partial V^{KS}}{\partial \tau_{\kappa\alpha p}} \Delta\tau_{\kappa\alpha p}, \tag{5.6}$$

thus taking the shape:

$$\hat{H}_{ep} = \sum_{n\mathbf{k},n'\mathbf{k}'} \langle \psi_{n\mathbf{k}} | \sum_{\kappa\alpha p} \frac{\partial V^{KS}}{\partial \tau_{\kappa\alpha p}} \Delta\tau_{\kappa\alpha p} | \psi_{n'\mathbf{k}'} \rangle \hat{c}^{\dagger}_{n\mathbf{k}} \hat{c}_{n'\mathbf{k}'}. \tag{5.7}$$

In normal mode coordinates this KS operator takes the form:

$$\sum_{\kappa\alpha p} \frac{\partial V^{KS}}{\partial \tau_{\kappa\alpha p}} \Delta\tau_{\kappa\alpha p} = N_p^{-1/2} \sum_{\mathbf{q}\nu} e^{i\mathbf{q}\cdot\mathbf{r}} \Delta_{\mathbf{q}\nu} v^{KS} (\hat{a}_{\mathbf{q}\nu} + \hat{a}^{\dagger}_{-\mathbf{q}\nu}), \tag{5.8}$$

with:

$$\Delta_{\mathbf{q}\nu} v^{KS} = l_{\mathbf{q}\nu} \sum_{\kappa\alpha} \left(\frac{M_0}{M_\kappa} \right)^{1/2} e_{\kappa\alpha,\nu}(\mathbf{q}) \left(\sum_p e^{-i\mathbf{q}\cdot(\mathbf{r}-\mathbf{R}_p)} \left. \frac{\partial V^{KS}}{\partial \tau_{\kappa\alpha}} \right|_{\mathbf{r}-\mathbf{R}_p} \right), \tag{5.9}$$

Combining Eqs. 5.7 and 5.8, and writing the electronic wave functions in Bloch form as $\psi_{nk}(\mathbf{r}) = N_p^{-1/2} u_{nk}(\mathbf{r}) e^{i\mathbf{k}\cdot\mathbf{r}}$, we can obtain:

$$\hat{H}_{ep} = N_p^{-1/2} \sum_{\mathbf{k},\mathbf{q}} \sum_{mn\nu} g_{mn\nu}(\mathbf{k}+\mathbf{q})\, \hat{c}^{\dagger}_{m\mathbf{k}+\mathbf{q}} \hat{c}_{n\mathbf{k}} (\hat{a}_{\mathbf{q}\nu} + \hat{a}^{\dagger}_{-\mathbf{q}\nu}), \tag{5.10}$$

where the electron phonon coupling tensor is given by:

$$g_{mn\nu}(\mathbf{k},\mathbf{q}) = \langle u_{m\mathbf{k}+\mathbf{q}} | \Delta_{\mathbf{q}\nu} v^{KS} | u_{n\mathbf{k}} \rangle_{uc} \tag{5.11}$$

Eq. (5.10) allows for the treatment of the electron-phonon coupling at linear order in the DFT formalism. A great advantage comes from the fact it can be solved in the UC, by computing the Bloch wavefunctions and the phonon quantities in the 1^{st} BZ. $g_{mn\nu}(\mathbf{k},\mathbf{q})$ is needed for the evaluation of the electron and phonon

self-energies and linewidths, temperature dependence of carrier lifetimes, direct and indirect phonon-assisted optical absorption spectra, anisotropic Eliashberg spectral function and, and importantly for the scope for this dissertation, carrier drift and Hall mobilities through the BTE (see Section 5.2).

In order to obtain properly converged results for mobility calculations, it is necessary to obtain $g_{mn\nu}(\mathbf{k},\mathbf{q})$ on dense meshes. For this purpose an interpolation scheme has been proposed, which relies on maximally localized Wannier functions (MLWF) [62, 63]. In general, Wannier functions are defined as

$$\mathrm{w}_{mp}(\mathbf{r}) = N_p^{-1} \sum_{n\mathbf{k}} e^{i\mathbf{k}\cdot(\mathbf{r}-\mathbf{R}_p)} \mathrm{U}_{nm\mathbf{k}} u_{n\mathbf{k}}(\mathbf{r}), \tag{5.12}$$

where $\mathrm{U}_{nm\mathbf{k}}$ is a unitary matrix in m and n. Given its freedom, it can be chosen so as to make Wannier functions real and maximally localized, precisely in real space. The inverse transformation of Eq. (5.12) reads

$$u_{n\mathbf{k}}(\mathbf{r}) = \sum_{mp} e^{-i\mathbf{k}\cdot(\mathbf{r}-\mathbf{R}_p)} U^{\dagger}_{mn\mathbf{k}} \mathbf{w}_{mp}(\mathbf{r}) \tag{5.13}$$

In practice, the standard procedure consists of calculating $g^{coarse}_{mn\nu}(\mathbf{k},\mathbf{q})$ on a coarse grid in reciprocal space, and then rotating it to real space via

$$\begin{aligned} g_{mnk\alpha}(\mathbf{R}_p,\mathbf{R}_{p'}) = \frac{1}{N_p N_{p'}} \sum_{\mathbf{k},\mathbf{q}} e^{-i(\mathbf{k}\cdot\mathbf{R}_p+\mathbf{q}\cdot\mathbf{R}_{p'})} \\ \times \sum_{m'n'\nu} \mathrm{u}^{-1}_{\kappa\alpha,\mathbf{q}\nu} \mathrm{U}^{\dagger}_{mm'\mathbf{k}+\mathbf{q}} \mathrm{g}^{coarse}_{m'n'\nu}(\mathbf{k},\mathbf{q}) \mathrm{U}_{n'n\mathbf{k}} \quad , \end{aligned} \tag{5.14}$$

where $\mathrm{u}_{\kappa\alpha,\mathbf{q}\nu} = \left(\frac{\hbar}{2M_\kappa \omega_{\mathbf{q}\nu}}\right)^{1/2} e_{\kappa\alpha,\nu}(\mathbf{q})$, and $e_{\kappa\alpha,\nu}(\mathbf{q})$ are the vibrational eigenmodes defined in Eq. (2.30).

At this point, an inverse interpolation to a fine reciprocal grid can be performed through the inverse transform:

$$g^{fine}_{mn\nu}(\mathbf{k},\mathbf{q}) = \sum_{pp'} e^{i(\mathbf{k}\cdot\mathbf{R}_p+\mathbf{q}\cdot\mathbf{R}_{p'})} \tag{5.15}$$

$$\times \sum_{m'n'\kappa\alpha} \mathrm{U}_{mm'\mathbf{k}+\mathbf{q}} \mathrm{g}_{m'n'\kappa\alpha}(\mathbf{R}_p,\mathbf{R}_{p'}) U^{\dagger}_{n'n\mathbf{k}} \mathrm{u}_{\kappa\alpha,\mathbf{q}\nu} \quad , \tag{5.16}$$

It should be evident, at this point, that the electron phonon coupling matrix relies on both the electronic and ionic ground state at 0 K. The electronic ground state is indeed broadly temperature independent, but the same can't be said for lattice vibrations. In a broad class of materials, the HA fails in case of a strong temperature dependence of the atomic vibrations, or, more seriously, it predicts imaginary phonons. In this case, Eq. (5.9) is not well defined for these imaginary frequencies $\omega_{\mathbf{q}\nu}$, and the associated electron-phonon elements show artificial divergencies.

We thus propose a strategy for mitigating this problem. We compute the derivatives of the Kohn-Sham potential in Eq. (5.9) at the DFPT level, but introduce the anharmonic phonon eigenfrequencies $\omega_{\mathbf{q}\nu}$ and eigenvectors $e_{\kappa\alpha,\nu}$ in the expression. This manipulation renormalizes the electron-phonon matrix elements, and introduces a temperature dependence in the coupling. The details of this approach are explored in Section 7.2.3, where the case of electronic transport in $KTaO_3$ in the presence of anharmonic phonons is examined.

5.2 Boltzmann transport equation

As explained in Section 5.1, the $g_{mn\nu}$ tensor is a central quantity in the determination of carrier transport in doped semiconductors. Let's briefly go through the steps required for obtaining a practical expression that can be tackled in an *ab initio* approach.

The equilibrium electric current $\mathbf{J}$ in a semiconductor is related to the external electric field $\mathbf{E}$ via:

$$J_\alpha = e(n_e\mu_{e,\alpha\beta} + n_h\mu_{h,\alpha\beta})E_\beta, \tag{5.17}$$

where $\mu_{e,\alpha\beta}$ and $\mu_{h,\alpha\beta}$ are the electron and hole mobility tensors, respectively, and the Greek indices denote Cartesian coordinates. The current density can also be expressed as an integral over the first BZ [64]:

$$J_\alpha = -e\Omega\sum_n \Omega_{BZ}^{-1}\int d\mathbf{k} f_{n\mathbf{k}} v_{n\mathbf{k},\alpha}, \tag{5.18}$$

where Ω and Ω_{BZ} are the unit-cell and BZ volumes respectively, $v_{n\mathbf{k},\alpha} = \hbar^{-1}\partial\epsilon_{n\mathbf{k}}/\partial k_\alpha$ is the band velocity and $f_{n\mathbf{k}}$ is the electronic occupation function, which reduces

to the Fermi-Dirac distribution $f^0_{n\mathbf{k}}$ in the absence of an electric field. By deriving the current with respect to the electric field, the electron mobility is expressed as:

$$\mu_{e,\alpha\beta} = -\frac{\sum_{n\in \mathrm{CB}} \int d\mathbf{k} v_{n\mathbf{k},\alpha} \partial_{E_\beta} f_{n\mathbf{k}}}{\sum_{n\in \mathrm{CB}} \int d\mathbf{k} f^0_{n\mathbf{k}}}, \tag{5.19}$$

where CB indicates the conduction bands. The response $\partial_{E_\beta} f_{n\mathbf{k}}$ can be computed starting from the BTE [64]:

$$\begin{aligned}
&- e\mathbf{E}\cdot\frac{1}{\hbar}\partial_{\mathbf{k}} f_{n\mathbf{k}} = \frac{2\pi}{\hbar}\sum_{m\nu}\int \frac{d\mathbf{q}}{\Omega_{BZ}} |g_{mn\nu}(\mathbf{k},\mathbf{q})|^2 \\
&\times [f_{n\mathbf{k}}(1-f_{m\mathbf{k}+\mathbf{q}})\delta(\epsilon_{n\mathbf{k}} - \epsilon_{m\mathbf{k}+\mathbf{q}} + \hbar\omega_{\mathbf{q}\nu}) n_{\mathbf{q}\nu} \\
&+ f_{n\mathbf{k}}(1-f_{m\mathbf{k}+\mathbf{q}})\delta(\epsilon_{n\mathbf{k}} - \epsilon_{m\mathbf{k}+\mathbf{q}} - \hbar\omega_{\mathbf{q}\nu})(1+n_{\mathbf{q}\nu}) \\
&- f_{m\mathbf{k}+\mathbf{q}}(1-f_{n\mathbf{k}})\delta(\epsilon_{m\mathbf{k}+\mathbf{q}} - \epsilon_{n\mathbf{k}} - \hbar\omega_{\mathbf{q}\nu})(1+n_{\mathbf{q}\nu}) \\
&- f_{m\mathbf{k}+\mathbf{q}}(1-f_{n\mathbf{k}})\delta(\epsilon_{m\mathbf{k}+\mathbf{q}} - \epsilon_{n\mathbf{k}} + \hbar\omega_{\mathbf{q}\nu}) n_{\mathbf{q}\nu}],
\end{aligned} \tag{5.20}$$

where $g_{mn\nu}(\mathbf{k},\mathbf{q})$ is the electron-phonon matrix element [8, 65]. By taking the derivative of Eq. (5.20) with respect to $\mathbf{E}$ the linearized BTE is obtained:

$$\begin{aligned}
&\partial_{E_\beta} f_{n\mathbf{k}} = e\partial_{\epsilon_{n\mathbf{k}}} f^0_{n\mathbf{k}} v_{n\mathbf{k},\beta}\tau^0_{n\mathbf{k}} \\
&+ \frac{2\pi\tau^0_{n\mathbf{k}}}{\hbar}\sum_{m\nu}\int \frac{d\mathbf{q}}{\Omega_{BZ}} |g_{mn\nu}(\mathbf{k},\mathbf{q})|^2 \\
&\times [(1+n_{\mathbf{q}\nu} - f^0_{n\mathbf{k}})\delta(\epsilon_{n\mathbf{k}} - \epsilon_{m\mathbf{k}+\mathbf{q}} + \hbar\omega_{\mathbf{q}\nu}) \\
&+ (n_{\mathbf{q}\nu} + f^0_{n\mathbf{k}})\delta(\epsilon_{n\mathbf{k}} - \epsilon_{m\mathbf{k}+\mathbf{q}} - \hbar\omega_{\mathbf{q}\nu})]\partial_{E_\beta} f_{m\mathbf{k}+\mathbf{q}},
\end{aligned} \tag{5.21}$$

where the relaxation time $\tau^0_{n\mathbf{k}}$ is defined as:

$$\begin{aligned}
\frac{1}{\tau^0_{n\mathbf{k}}} &= \frac{2\pi}{\hbar}\sum_{m\nu}\int \frac{d\mathbf{q}}{\Omega_{BZ}} |g_{mn\nu}(\mathbf{k},\mathbf{q})|^2 \\
&\times [(1-f^0_{m\mathbf{k}+\mathbf{q}} + n_{\mathbf{q}\nu})\delta(\epsilon_{n\mathbf{k}} - \epsilon_{m\mathbf{k}+\mathbf{q}} - \hbar\omega_{\mathbf{q}\nu}) \\
&+ (f^0_{m\mathbf{k}+\mathbf{q}} + n_{\mathbf{q}\nu})\delta(\epsilon_{n\mathbf{k}} - \epsilon_{m\mathbf{k}+\mathbf{q}} + \hbar\omega_{\mathbf{q}\nu})].
\end{aligned} \tag{5.22}$$

Eq. ((5.21)) is valid in the limit of low electric field-induced energy gain with respect to the thermal energy: $eE_\beta v_{n\mathbf{k},\beta}\tau^0_{n\mathbf{k}} << k_B T$. The iterative BTE scheme (IBTE) consists in solving (5.21) self-consistently, while the simpler self-energy relaxation time approximation (SERTA) ignores the integral in $d\mathbf{q}$. In this case, the mobility reduces to:

$$\mu^{\mathrm{SERTA}}_{e,\alpha\beta} = \frac{-e}{n_e\Omega}\sum_{n\in \mathrm{CB}}\frac{d\mathbf{k}}{\Omega_{\mathrm{BZ}}}\partial_{\epsilon_{n\mathbf{k}}} f^0_{n\mathbf{k}} v_{n\mathbf{k},\beta}\tau^0_{n\mathbf{k}}. \tag{5.23}$$

5.3 Special Displacements Methods

The zero-point renormalization of the electronic band gap and its temperature dependence are another notable effect of the electron-phonon coupling. The most common approach employed to obtain the renormalized electronic eigenvalues as a function of temperature and including the zero point renormalization (ZPR) effects is the Allen-Heine-Cardona (AHC) theory [66, 66]. The practical implementation requires the second order variation of the KS potential and it is thus quite expensive.

An alternative approach relies on the use of supercells. The temperature dependence of any electronic observable $O(T)$ can be evaluated through a multivariate Gaussian integral over the normal coordinates x_ν:

$$O(T) = \prod_\nu \int dx_\nu \frac{\exp\left(-\frac{x_\nu^2}{2\sigma_{\nu,T}^2}\right)}{\sqrt{2\pi\sigma_{\nu,T}^2}} O(x_\nu) \tag{5.24}$$

where $\sigma_{\nu,T}$ is the root-mean square displacement of the atoms at temperature T along the phonon mode ν:

$$\sigma_{\nu,T}^2 = \langle x_\nu^2 \rangle_T = (2n_{\nu,T} + 1) l_{\nu,T}^2. \tag{5.25}$$

The quantities in Eq. (5.25) have already showed up in Section 3.1: $n_{\nu,T}$ is the Bose-Einstein distribution of Eq. (2.37), and $l_{\nu,T}$ is the zero-point amplitude of Eq. (2.34). Eq. (5.24) has to be solved for a virtually infinite supercell size, and for a dense sampling of the configuration space, thus making it time consuming in most practical cases.

An alternative approach was proposed by M. Zacharias and F. Giustino [67], where the MC integral is estimated through a "one-shot" evaluation of the argument for a certain "specially displaced" supercell configuration. This approach is commonly known as the Zacharias-Giustino (ZG) displacements method. The displacements from the equilibrium positions of the atoms in the supercell are chosen via:

$$\Delta\tau_{\kappa\alpha} = \left(\frac{M_p}{M_\kappa}\right)^{\frac{1}{2}} \sum_\nu (-1)^{\nu-1} e_{\kappa\alpha,\nu}\sigma_{\nu,T}. \tag{5.26}$$

The method is exact for infinitely large supercells, but it is shown to yield sufficiently accurate results already for moderate-sized supercells. For finite supercells, it is possible to average the electronic eigenvalues obtained for a handful of special displacements. It is worth noting that a reformulation of the method [68] allows for the determination of the ZG configurations in Eq. 5.26 via quantities calculated using DFPT within the UC rather than in the supercell:

$$\Delta\tau_{p\kappa} = \sum_{\mathbf{q}\in\mathcal{B},\nu} S_{\mathbf{q}\nu} \left[\frac{\hbar}{2N_p M_\kappa \omega_{\mathbf{q}\nu}}(2n_{\mathbf{q}\nu,T}+1)\right]^{\frac{1}{2}} \times 2\Re\left[e^{i\mathbf{q}\cdot\mathbf{R}_p} e_{\kappa,\nu}(\mathbf{q})\right], \tag{5.27}$$

thus making it even less time consuming.

5.4 Polarons in DFPT

In order to compute the polaron energy and wavefunction from *ab initio* calculations, we leverage the theory recently developed by W. H. Sio et al [69, 70]. The method is implemented in the Electron-Phonon coupling using Wannier functions (EPW) package and interfaces with Quantum Espresso (QE) as a DFPT engine. An extensive explanation of the derivation can be consulted in these two papers. Here, we report the basic concepts necessary for the interpretation of the results presented in Chapter 8. The method models the polaron as a single charge of wavefunction $\psi(\mathbf{r})$ interacting with the electrons of the hosting material. The wavefunction is expanded in the computed KS states for the n bands on a $\mathbf{k}$-mesh through a set of coefficients $A_{n\mathbf{k}}$:

$$\psi(\mathbf{r}) = \frac{1}{\sqrt{N_p}} \sum_{n\mathbf{k}} A_{n\mathbf{k}}\psi_{n\mathbf{k}}(\mathbf{r}), \tag{5.28}$$

In the case of the electron polaron, n corresponds to conduction band state, and in the case of the hole polaron to valence sates. The expansion in Eq. (5.28) is an approximation which holds on the observation that electron (hole) polarons

have a similar orbital character as the electrons at the conduction band bottom (valence band top), and their energy state lies slightly below (above). On the other hand, the atomic displacements generated in the supercell by the presence of the added electron (or hole) are expanded in set of collective vibrations generated by the phonon modes ν on a $\mathbf{q}$-mesh, through a set of $B_{\mathbf{q}\nu}$ coefficients:

$$\Delta\tau_{\kappa\alpha p} = -\frac{2}{N_p}\sum_{q\upsilon} B^*_{\mathbf{q}\nu}\left(\frac{\hbar}{2M_\kappa\omega_{\mathbf{q}\nu}}\right)^{1/2} e_{\kappa\alpha,\nu}(\mathbf{q})e^{i\mathbf{q}\cdot\mathbf{R}_p}. \tag{5.29}$$

Both the KS wavefunctions in Eq. (5.28) and the phonon quantities in Eq. (5.29) are routinely computed in a DFPT UC treatment. At this point, the $A_{n\mathbf{k}}$ and $B_{\mathbf{q}\nu}$ coefficients can be calculated from the solution of the following system of coupled equations:

$$\frac{2}{N_p}\sum_{qm\upsilon} B_{q\upsilon}g^*_{mn\upsilon}(\mathbf{k},\mathbf{q})A_{m\mathbf{k}+\mathbf{q}} = (\varepsilon_{n\mathbf{k}} - \varepsilon)A_{n\mathbf{k}} \tag{5.30}$$

$$B_{\mathbf{q}\nu} = \frac{1}{N_p}\sum_{mn\mathbf{k}} A^*_{m\mathbf{k}+\mathbf{q}}\frac{g_{mn\nu}(\mathbf{k},\mathbf{q})}{\hbar\omega_{\mathbf{q}\nu}}A_{n\mathbf{k}}, \tag{5.31}$$

where N_p is the number of UCs (determined by the commensurate supercell defined by the reciprocal $\mathbf{k}$- and $\mathbf{q}$ meshes), ε is the polaron eigenvalue, $\varepsilon_{n\mathbf{k}}$ are the Bloch eigenvalues, $\omega_{\mathbf{q}\upsilon}$ the phonon eigenfrequencies and $g_{mn\nu}(\mathbf{k},\mathbf{q})$ are the electron-phonon matrix elements. The system of equations has to be solved on a reciprocal fine grid in the $A_{n\mathbf{k}}$ and $B_{\mathbf{q}\nu}$ expansion coefficients, at which point both the polaron wavefunction and the lattice distortions in the supercell can be defined through Eqs. 5.28 and 5.29. The polaron formation energy can then be calculated as:

$$\Delta E_f = \frac{1}{N_p}\sum_{n\mathbf{k}}|A_{n\mathbf{k}}|^2(\varepsilon_{n\mathbf{k}} - \varepsilon_{\mathrm{CBM}}) - \frac{1}{N_p}\sum_{q\upsilon}|B_{q\upsilon}|^2\hbar\omega_{q\upsilon}. \tag{5.32}$$

Eq. (5.32) interprets the formation energy as the balance of a positive energy contribution needed for the wavefunction localization and a negative contribution coming from the distortion generated for accommodating the polaron.

CHAPTER 6

Bandgap Renormalization in Diamond

In this Chapter, the band gap renormalization in C-diamond is investigated through the SDM.

Section 6.1 offers a review of the methodologies employed for the calculation of renormalized band-gaps in semiconductors and insulators.

Section 6.2 deals with the technical details around the construction of the MLFF in preparation of the SSCHA calculations.

Section 6.3 shows the calculations of the lattice expansion at various levels of approximation, and how they compare to the computational and experimental literature.

In Section 6.4 we show the results for the band-gap renormalization by taking into account lattice expansion and the use of the HA and SSCHA dynamical matrices.

6.1 Introduction

Diamond, a crystalline allotrope of carbon with a cubic structure belonging to the $Fd\bar{3}m$ space group, stands as a paradigmatic material for investigating lattice dynamics and its impact on electronic properties, due to its simplicity and the abundance in literature data. Here, we focus on the indirect band gap renormalization as induced by lattice thermal expansion and electron-phonon scattering, in the temperature range between 0 K and 700 K. In the end, we will compare results as obtained by different combined methods with the experimental data.

The thermal expansion is treated within the framework of QHA, MD and SSCHA, as we will briefly explain in the following. The QHA captures the volume dependence of phonon frequencies to estimate the lattice free energy, offering a computationally efficient approach to modeling thermal expansion in mostly harmonic materials like diamond. The SSCHA, on the other hand, provides a more sophisticated treatment by including higher-order anharmonic effects. MD simulations are also performed, complementing the QHA and SSCHA frameworks. MD allows to include full phonon anharmonicity (unlike the QHA and in analogy with SSCHA), but neglecting quantum effects (unlike the QHA and SSCHA). Consequently, in the MD case, a constant lattice expansion (a linear growth of the lattice parameter) is expected, since the typical low temperature plateau is not captured in the classic approximation for nuclear motion. On the other hand, the QHA is expected to reproduce the low temperature lattice constant plateau but slightly fail at higher temperatures, while SSCHA should be the best method by including both zero-point motion and full anharmonicity. These observations will be confirmed by a comparison with the experimental data.

A cornerstone of this study is the integration of MLFF into all computational frameworks, as it provides a powerful means to model interatomic interactions with high accuracy while significantly reducing computational costs. We achieve consistent and efficient calculations of thermal expansion, phonon properties, and anharmonic effects across QHA, SSCHA, and MD methods. In the MD case the trajectories are calculated directly using VASP and the MLFF. For the QHA,

the MLFF model is used for the PES prediction. The same model is then used in the SSCHA following the workflow explained in Section 4.2.

Building on this foundation, we investigate the electron-phonon coupling and its effect on the temperature-dependent renormalization of diamond's indirect band gap, also including the lattice expansion. Accurate modeling of the electron-phonon interaction is essential for understanding how lattice vibrations influence electronic properties. Several methods have been used in order to estimate the electron-phonon interaction, among which the AHC theory and the use of vibrational averages as computed by MC integration, MD and path-integral molecular dynamics (PIMD). A comprehensive review of these methods is given in Ref. [65].

In this chapter, we calculate the band gap renormalization using the SDM described in Section 5.27 and the harmonic and anharmonic dynamical matrices derived in the QHA and SSCHA respectively, including lattice expansion. The QHA reproduces the temperature-dependent band gap renormalization quite accurately, while SSCHA exhibits excellent agreement with experimental data.

Notably, we find that the band gap renormalization predicted in this work differs from recent literature results [71] where the thermal expansion was overestimated by a factor of two with respect to experimental data. This overestimation led to too strong renormalizations at elevated temperatures, thus underestimating the accuracy of the Perdew-Burke-Ernzerhof (PBE) approximation.

This study also highlights the versatility and utility of MLFFs in enhancing the predictive power of both QHA and SSCHA. By enabling efficient and accurate modeling of anharmonic effects, MLFFs prove to be invaluable tools for studying complex lattice dynamics. On a side note, the agreement between QHA and SSCHA predictions for thermal expansion and phonon spectra demonstrates the utility of the QHA as a computationally efficient method when higher-order anharmonic effects are less pronounced.

6.2 Methods

As described in Section 4.2, the first step to be taken before performing the actual SSCHA calculations is the construction of a MLFF. We run an on-the-fly *a*b initio MD. The MD runs are performed allowing the volume and cell shape fluctuations at fixed 0 kPa pressure and temperature (NPT ensemble) between 1 and 1000- K, every 100 K, with a time step of 1 fs and using the final structure at each temperature as the starting configuration for the higher ones, for a total of around 100000 steps. A Langevin thermostat is employed [52], with a friction coefficient of 10 ps^{-1}. The cut-off radius for both the two- and three-body atomic density distribution descriptors is set to 13 Å, and the Gaussian broadening to 0.3 Å. 1151 *ab initio* training configurations were gathered. The *ab initio* calculations are performed at the GGA level, using the PBE [72] functional and PAW potentials [58], using a plane-wave cutoff of 800 eV. We employ a pseudo-potential that freezes the $1s^2$ core states while treating the $2s^2$ and $2s^2$ states as valence electrons. A cubic $5\times5\times5$ supercell and a single Γ point in reciprocal space are employed. We use the real-space projection scheme that is more computationally efficient for the DFT supercell calculations. We set an electronic convergence threshold of 10^{-7} eV.

We evaluate the volume expansion in temperature by means of various techniques. We employ the QHA and the BM-EoS (see Section 2.4) as implemented in the PHONOPY package [73] both using direct DFT calculations and with the aid of the MLFF for the evaluation of the ground state energy at different volumes and the volume dependent phonon frequencies in Eq. (3.9). We employ 25 volumes for the BM-EoS fit for 11 temperatures, between 0 K and 1000 K with a step of 100 K. To evaluate the volume expansion using the MD simulations, we average the volumes obtained throughout each run. The thermal expansion in SSCHA was obtained running several NPT minimizations at a pressure of 0 kPa.

The Bubble correction to the self-consistent SSCHA frequencies was computed by considering 10000 ensembles, and the interpolation was performed on a $5\times5\times5$ reciprocal space grid.

The special displacement formula of Eq. (5.26) was implemented and vali-

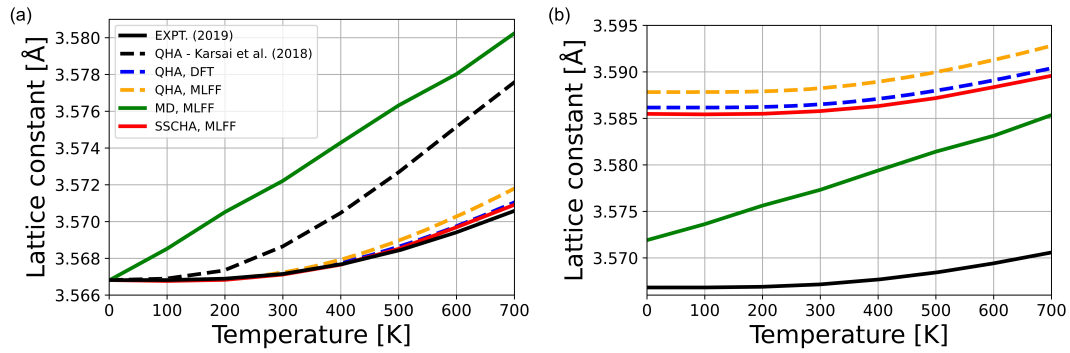


Figure 6.1. Lattice expansion in diamond between 0 K and 700 K calculated using different techniques: the QHA both directly within DFT (blue dashed line) and with the aid of the MLFF (orange dashed line); from the average of the lattice vectors from the MD runs used for constructing the MLFF (green line); and from NPT minimizations in SSCHA to obtain the equilibrium volume at each temperature (red line). The experimental lattice constant (black line) and the QHA calculations from Ref. [71] (black dashed line) are shown for comparison. (a) All the plots are shifted to the experimental lattice constant at 0 K. (b) Data are plotted without shifts.

dated against the routine implemented in VASP. This was necessary in order to interface the method with the SSCHA matrices. A single special displacement was employed, by starting from the pristine $5\times5\times5$ supercell, which is enough to achieve statistical accuracy as showed in literature for C-diamond [71].

The band gap renormalization due to the electron-phonon coupling was computed by subtracting the clamped-nuclei band gap to the one calculated on the specially displaced supercell. In order to deal with the splitting of the degenerate band edges arising from the supercell calculation, we compute the band gap by taking the mean of the three lowest eigenvalues at the conduction band minimum (CBM) (Γ point) and the mean of the six highest eigenvalues at the valence band maximum (X point).

6.3 Volume Expansion and Phonon Dispersions

The QHA results obtained using DFT and the MLFF are in fair agreement and match the experimental data [74, 75], as shown in Figure 6.1a, thus offering an indirect validation of the accuracy of the MLFF. An overview of the BM-EoS fits at different temperatures and the extrapolated volumes (and the associated

volume expansion coefficient trend) is shown in Figure 6.2 for the DFT case.

As expected, the linear expansion obtained from the MD overestimates the experimental one in the low temperature region, where the quantum effects lead to a well-known volume plateau, which is reproduced at the QHA and SSCHA level. The high temperature expansion rate almost matches the one predicted by QHA and SSCHA, but it is still greater at 700 K, thus signaling that the quantum effects keep playing a role in this range. The QHA and SSCHA predict a similar expansion and equilibrium volume at 0K K, as shown in Figure 6.1b, thus proving that C-diamond shows a really moderate phonon anharmonicity.

Rather surprisingly, we find a strong disagreement with a recent QHA calculation from Ref. [71], where the lattice expansion is overestimated by a factor of two with respect to the experiments, using a comparable *ab initio* setup as the one employed in this work. As a result, the linear expansion coefficient is also strongly overestimated, as shown in Figure 6.3. On the other hand, results obtained in this study at the QHA + DFT level reproduce the experimental data fairly well, with the use of the MLFF bringing similar results as the DFT-based approach, thus offering a further indirect validation for the accuracy of the MLFF.

The harmonic phonon spectrum as computed by finite displacements using the MLFF in Figure 6.4 perfectly matches the DFT calculation, thus proving once again the accuracy of the MLFF model. The SSCHA spectrum at 0 K is only slightly different than the harmonic one, as expected for diamond.

6.4 Bandgap renormalization

The band gap renormalization has been calculated using the ZG supercell as constructed by employing the harmonic DM calculated using either DFT and MLFF, or by employing the SSCHA anharmonic DM. Furthermore, different lattice constants have been employed, either experimental or from DFT, MLFF, QHA and SSCHA. All the results for the band gap renormalization are shown in Figure 6.5. Below, we provide a detailed description of the different calculations and brief comparative comments:

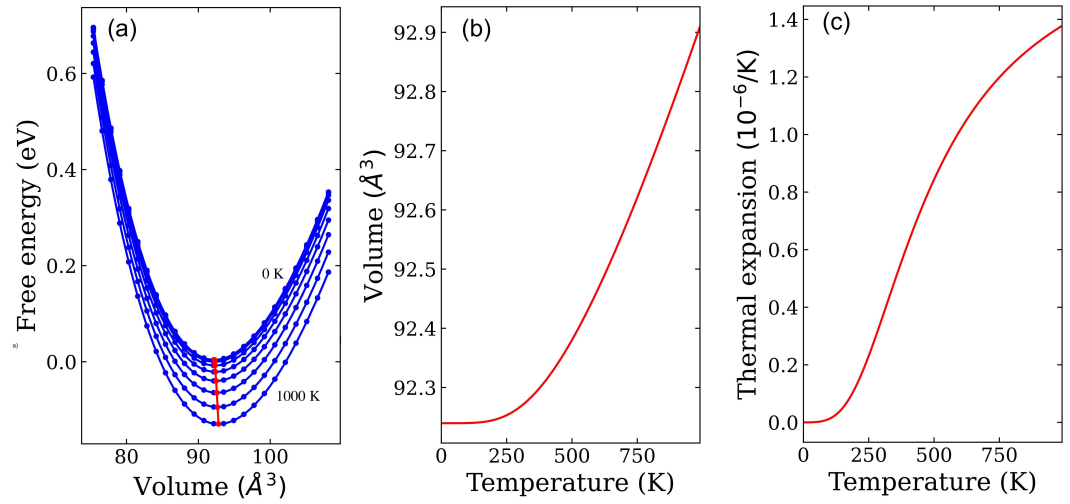


Figure 6.2. (a) BM-EoS fits of the free energies computed between 0 K and 900 K at different volumes, with the equilibrium volumes highlighted in red. (b) Plot of the equilibrium volumes obtain by the BM-EoS fits as function of temperature. (c) Volume expansion coefficient at different temperatures.

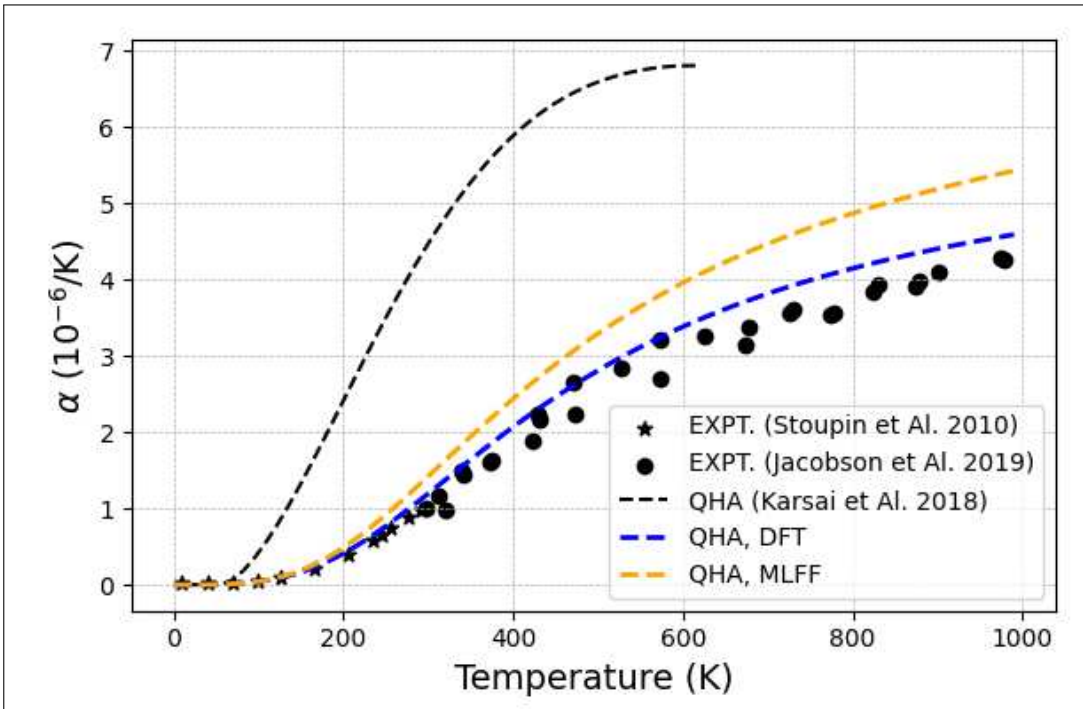


Figure 6.3. Linear expansion coefficient as a function of temperature obtained through the QHA both at DFT level (dashed blue line) and at MLFF level (dashed orange line). The experimental data [74, 75] and previous QHA results [71] are shown for comparison.

1. Using the experimental lattice constant a_{exp}, computing phonons within the HA in DFT or MLFF, and finding the ZG configuration for the a_{exp} supercell at different temperatures. In this case, we obtain very similar results since the DMs are in very close agreement.

2. Using the optimized lattice constant from DFT, a_{DFT}, and MLFF, a_{MLFF},

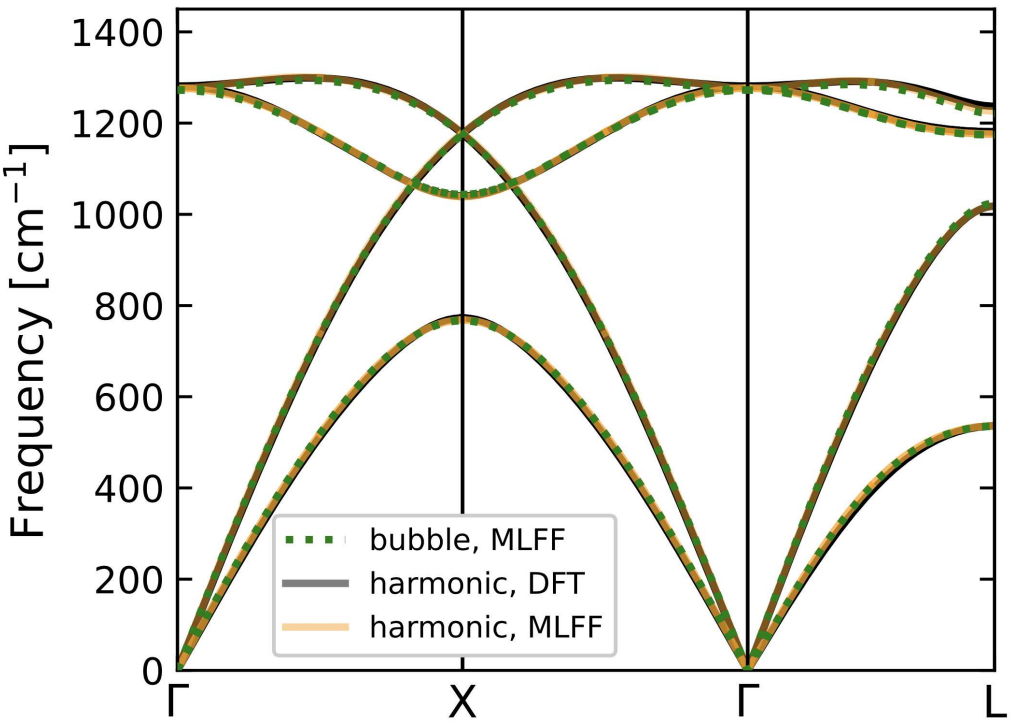


Figure 6.4. Phonon spectrum as calculated by diagonalization of the harmonic dynamical matrices obtained using DFT (black line), MLFF (orange line) and SSCHA at 0 K (dashed green line).

computing phonons in DFT or MLFF, and finding the ZG configuration respectively for the a_{DFT} and a_{MLFF} supercells at different temperatures. Also in this case results are similar, since the predicted lattice constants are in excellent agreement.

3. Using the volume expansions as predicted by performing the QHA and BM-EoS workflow at DFT level, $a_{DFT}(T)$, and at MLFF level, a_{MLFF}(T). Again, we obtain similar renormalizations in temperature, since also the volume expansion is well predicted by the MLFF.

4. Using the experimental lattice constant a_{exp} and the SSCHA dispersion at 0 K in order to find the ZG supercell. In this case, the renormalization is quite stronger than in point (1), even if the anharmonic dispersion differs just slightly from the harmonic case.

5. Using the lattice constant as predicted by SSCHA at 0 K, $a_{SSCHA}(0)$, and the SSCHA dispersion at 0 K in order to find the ZG supercell. In this case, the renormalization is stronger than in point (4), since $a_{SSCHA}(0)$ is greater

than a_{exp}, in analogy with the comparison between points (1) and (1).

6. Using the volume expansions as predicted by performing the SSCHA workflow, $a_{sscha}(T)$, and the temperature dependent SSCHA dynamical matrix. In this case we obtain a stronger renormalization than in point (5) and a very close match with the experimental data.

Summing up, MLFF-predicted volume expansions and phonon dispersion perfectly match the DFT results, thus offering a concrete opportunity of using MLFF for more complex materials, even to compute subtle effects such as the band gap renormalization. Furthermore, we can observe how for a harmonic material like diamond a relatively simple "QHA volume expansion + GGA + ZG displacements" recipe can obtain realistic results for the band gap renormalization. Finally, the addition of the more accurate volume expansion and temperature dependent phonon dispersions as computed by SSCHA can bring an almost complete agreement of the computed indirect band gap with the experimental data.

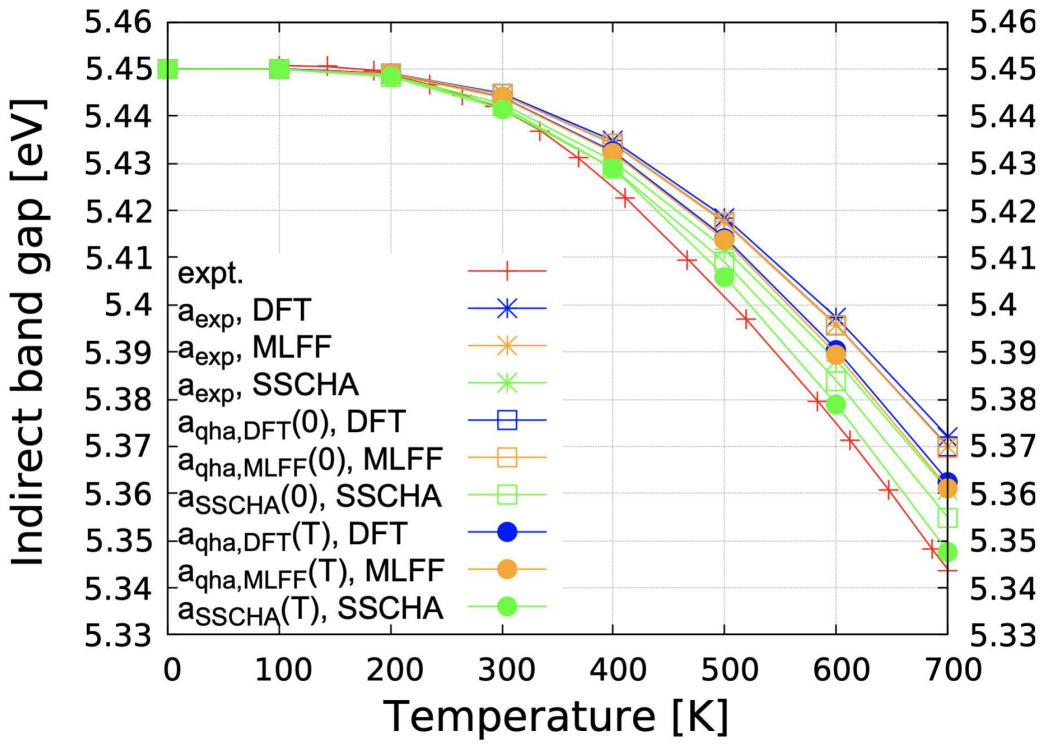


Figure 6.5. Renormalization of the indirect band gap in diamond as computed through the ZG displacements induced by harmonic DFT matrices (blue markers) at three different approximation: fixing experimental lattice constant a_{exp}, using QHA predicted lattice constant at 0 K $a_{QHA}(0)$ and considering the lattice expansion at each temperature $a_{QHA}(T)$. The predictions based on both MLFF dynamical matrices and lattice expansion (orange markers) are in full agreement with the DFT results. The ZG displacements are also generated based on the SSCHA matrices (green markers) using a_{exp}, using the SSCHA predicted lattice constant 0 K $a_{SSCHA}(0)$ and considering the expansion of the lattice as computed in SSCHA $a_{SSCHA}(T)$. All data have been shifted to the 0 K experimental indirect band gap of 5.45 eV (red line) [76].

CHAPTER 7

Mobility and phonon anharmonicity

This Chapter represents the most dense part of the dissertation. Here, we deal with the problem of describing the electronic mobility in two strongly anharmonic materials, $KTaO_3$ and $SrTiO_3$.

In Section 7.1 we describe the successes of the BTE in a wide array of semiconducting materials, and their failure in the prediction of the electronic mobility in case of anharmonic materials and in the case of a broken QP picture.

Section 7.2 reports the technical details of the MLFF+SSCHA scheme employed, described how the electron-phonon matrix elements can be calculated with the inclusion of the anharmonic phonon effects and lattice disorder effects on the band structure and how the mobility results can be re-scaled by taking into account the transport mass renormalization due to disorder and electron-phonon coupling, by leveraging the ZG displacements as computed through the anharmonic matrices.

Section 7.3 discusses the strength of disorder and renormalization effects in $KTaO_3$ and $SrTiO_3$ and their effects on the electron mobility, thus proving how that the BTE are still able to offer a compelling description of these two materials and their departure from the QP picture.

Most of the results reported in this Chapter have been published as:
[77]: L. Ranalli, C. Verdi, M. Zacharias, J. Even, F. Giustino and C. Franchini, "Electron Mobilities in $SrTiO_3$ and $KTaO_3$: Role of Phonon Anharmonicity, Mass Renormalization and Disorder", Physical Review Materials, 8, 104603 (2024).
Conception, execution and analysis done independently and under technical guidance of my supervisor C. Franchini and C. Verdi. M. Zacharias has been of invaluable help in the calculation of electronic mass renormalization due to electron-phonon coupling and local disorder.

7.1 Introduction

Transition-metal oxide perovskites have garnered significant attention due to their diverse range of fascinating physical and chemical properties. These materials exhibit phenomena such as high-temperature superconductivity [78, 79], magnetoresistance [80], ferroelectricity [81], multiferroicity [82, 83], and piezoelectricity [84]. The emergence of these properties is attributed to the structural and chemical flexibility of perovskites, as well as the intricate interplay among their orbital, spin, lattice, and charge degrees of freedom [85–89].

These unique characteristics position perovskites as key materials for cutting-edge technological applications. They are integral to the development of non-volatile memory devices, spintronic systems, and nanoelectronics. Furthermore, they play a pivotal role in energy-related innovations, such as solid oxide fuel cells and metal-air batteries [90–94], offering promising pathways for sustainable energy technologies.

Understanding charge transport in transition-metal oxide perovskites is a fundamental aspect for optimizing their performance in a wide range of applications. Insight into charge transport mechanisms not only clarifies the underlying processes behind experimental observations but also enables the enhancement of carrier mobility. From a computational standpoint, solving the BTE for charge carriers using *ab initio* predicted parameters has emerged as a powerful and increasingly popular approach. This method is favored for its accuracy and has benefited from the development of efficient computational implementations [95–99].

While there is extensive literature focusing on standard semiconductors [100–120], studies on carrier mobility in transition-metal perovskites are relatively scarce [121–125]. This limited coverage highlights the need for more focused computational and theoretical investigations into charge transport in these complex systems, which could unlock further potential in practical applications.

Previous studies [95, 108] have shown that moderate deviations between BTE predictions and experimental carrier mobilities may be attributed to the incomplete treatment of electronic correlations, dielectric screening, or inaccura-

cies in carrier effective masses. Such deviations can often be corrected through semi-empirical rescaling techniques or more precise many-body calculations. However, if a significant mismatch with experimental data persists, it could signal deeper issues, such as the inadequacy of the HA for electron-phonon coupling or a breakdown of the QP approximation, which underpins the BTE framework.

When strong electron-phonon coupling is present, the electronic structure may exhibit satellite features close to the CBM and pronounced broadening of electronic bands, both of which violate the QP picture. This phenomenon has been observed in angle-resolved photoemission spectroscopy (angle-resolved photoemission spectroscopy (ARPES)) studies of $SrTiO_3$ surfaces [126], where polaronic satellites have been proposed as the origin of optical conductivity sub-bands [127, 128] in bulk $SrTiO_3$, as well as the observed reduction in mobility between 150K and 300K [122], based on the Kubo formula.

Interestingly, although the conduction band of $KTaO_3$ shares a similar orbital character with $SrTiO_3$, ARPES spectra of $KTaO_3$ surfaces do not reveal any clear polaronic satellite peaks [129]. Nevertheless, the possibility of significant QP broadening in bulk $KTaO_3$ at room temperature remains an open question. Such effects could impact the accuracy of BTE-based mobility predictions and necessitate the use of more advanced theoretical approaches to fully capture the transport properties of $KTaO_3$ and related materials.

In the electron-phonon scattering regime, the experimental electron mobility in bulk $KTaO_3$ is nearly an order of magnitude higher than that observed in $SrTiO_3$ [130, 131]. To investigate the origin of this unexpected behavior, we perform BTE calculations of electron mobility for both materials over the temperature range of 150 to 300 K.

To accurately capture the strong temperature dependence of the phonon dispersions, we renormalize the electron-phonon matrix elements by incorporating temperature-dependent dynamical matrices. These matrices are computed using the SSCHA [14–18, 132]. Leveraging high-fidelity MLFFs allows us to handle large supercells in SSCHA, following the scheme recently proposed for $KTaO_3$ and $SrTiO_3$ [26, 27]. This approach is essential for $SrTiO_3$, as its harmonic

phonon dispersions exhibit imaginary modes, requiring anharmonic stabilization. Incorporating the temperature-dependent SSCHA dynamical matrices enables a more accurate reproduction of the temperature dependence of the electron mobility in both materials.

Surprisingly, the computed mobilities for $KTaO_3$ and $SrTiO_3$ are comparable across the entire temperature range, and both significantly exceed experimental values — particularly in the case of $SrTiO_3$. To address this discrepancy, we explore several potential factors. We investigate dielectric screening corrections, spin-orbit coupling (SOC), anharmonic phonon effects, and the influence of electronic correlations on the effective masses. Our analysis suggests that the larger renormalization of the effective mass at the CBM in $SrTiO_3$, driven by electron-phonon coupling, is the primary reason for the overestimation.

This enhanced mass renormalization is not captured in standard BTE calculations, where electronic band structures are typically computed using DFT with nuclei clamped to their equilibrium positions. Moreover, the discrepancy is exacerbated by an additional contribution to the mass renormalization in $SrTiO_3$ due to local disorder effects [133], which we predict to be absent in $KTaO_3$.

Finally, we propose that residual overestimation of experimental mobility could be attributed to QP broadening and the limitations of the HA for electron-phonon coupling. Both effects are known to impact transport properties, and their role is particularly pronounced in materials like $SrTiO_3$. This is consistent with earlier reports that have highlighted similar issues with BTE-based mobility predictions for other semiconductors [108].

7.2 Methods

TThis section aims to provide a comprehensive explanation of the steps involved in calculating the electron mobility in $SrTiO_3$ and $KTaO_3$.

A comprehensive explanation of the training and validation procedure for $SrTiO_3$ and $KTaO_3$ MLFFs can be found in Sections 7.2.1. The efficacy of the SSCHA+MLFF methodology is demonstrated in Section 7.2.2. The approach utilized for the renormalization of electron-phonon matrix elements, incorporating

temperature-dependent anharmonic phonon effects, is outlined in Section 7.2.3. Lastly, Section 7.2.4 provides a discussion on how local disorder is accounted for in carrier mobility calculations.

7.2.1 Training and validation of MLFFs

As outlined in Section 4.2, the initial step prior to carrying out SSCHA calculations involves constructing a MLFF for $SrTiO_3$ and $KTaO_3$. The MLFF for $KTaO_3$ is developed using on-the-fly *ab* initio MD simulations. These MD simulations are conducted within an NVT ensemble at fixed volumes and temperatures of 100, 200, 300, and 400 K, with each temperature's final structure serving as the starting configuration for the next. A 2 fs time step is used, and a Langevin thermostat [52] with a friction coefficient of 10 ps^{-1} is employed for the single atomic species. The cutoff radius for two- and three-body atomic density descriptors is set to 13 Å, with a Gaussian broadening of 0.3 Å. Over the course of 500,000 MD steps, 421 training configurations from *ab* initio calculations were collected. These calculations were performed at the meta-generalized gradient approximation (meta-GGA) level using the SCAN functional and PAW potentials [58]. The computational setup includes a plane-wave cutoff of 800 eV, a hard pseudopotential for O atoms, and the inclusion of semicore *s* states for K and *p* states for Ta, ensuring consistency with the QE pseudopotentials (Details on QE calculations in Section 7.2.3). A 4×4×4 cubic supercell with a 2×2×2 Monkhorst-Pack k-point mesh is used for the calculations.

The training data for $SrTiO_3$ are sourced from Ref. [27], where it was shown that data generated at the RPA level accurately capture the temperature-dependent experimental phonon dispersions via SSCHA. In this work, the MLFF is retrained using the same data set and methodology, but with an expanded 13 Å cutoff radius for atomic density distributions, mirroring the approach taken for $KTaO_3$. This refinement ensures the proper reproduction of optical phonon dispersions near the Γ point once the NAC is applied.

In polar materials, a macroscopic electric field arises in the $\mathbf{q} \to 0$ limit due to the long-range nature of the Coulomb interaction. This presents a challenge for the direct Fourier interpolation of the FCs, as it leads to inaccuracies in the

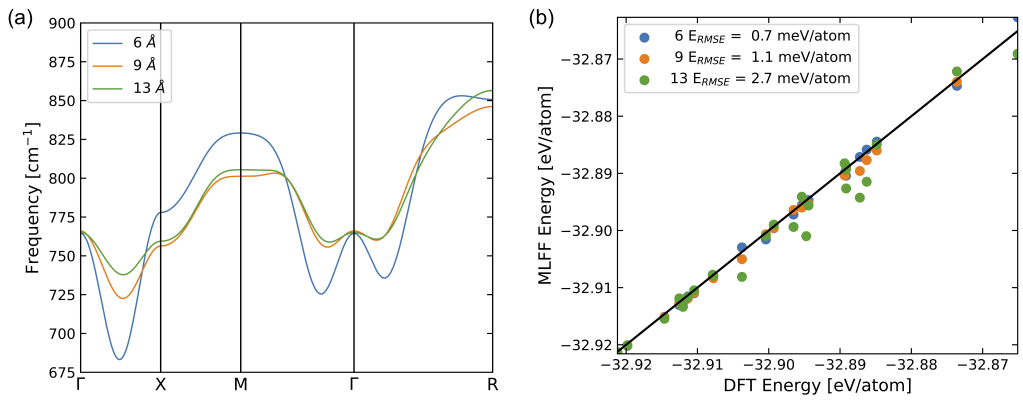


Figure 7.1. Accuracy of the MLFF for SrTiO3. (a) Highest frequency LO branch as computed by MLFF at the harmonic level using FCs interpolated from a 4×4×4 supercell. The artificial wiggling around the Γ-point is cured by increasing the cut-off radius for the radial and angular descriptors. (b) Energy RMSE on the RPA test set using different values for the cut-off radii.

DM $\Phi(\mathbf{q})$ near $\mathbf{q} = 0$. The standard method [13] involves splitting the FCs into short- and long-range components, with only the short-range component being interpolated. The long-range dipole-dipole interaction is subsequently reintroduced for each $\mathbf{q}$-point in the BZ.

When a MLFF is employed to compute interatomic forces, the finite cutoff radius for the radial and angular local descriptors can introduce artificial "wiggles" in the phonon eigenfrequencies near the Γ point. This artifact arises if the cutoff radius is smaller than the size of the supercell used in training. Under such conditions, the dipole-dipole portion of the interatomic FCs, which is subtracted prior to interpolation, may no longer match the effective range of interatomic forces as captured by the MLFF.

Using an extended cutoff radius of 13 Å for the descriptors effectively suppresses this spurious behavior, as illustrated in Fig. 7.1a for the highest frequency LO mode. This choice of cutoff is comparable to the size of the supercell employed in the calculation of the FCs, ensuring consistency and accuracy in the interpolation process.

This adjustment introduces a minor reduction in the accuracy of the MLFF regarding the RMSE of the energies on a test dataset. The test datasets are derived from MD simulations conducted over a temperature range from 0K to 400K. For $SrTiO_3$, 25 structures of 10-atom cells are extracted from an NPT (fixed-pressure) simulation to validate the MLFF's accuracy against RPA data.

In the case of $KTaO_3$, 25 structures from an NVT (fixed-volume) simulation of a larger $4\times4\times4$ supercell are used, as the SCAN functional is computationally feasible within this larger supercell.

For $SrTiO_3$, as shown in Fig.7.1b, the RMSE exhibits a slight increase with larger cutoff radii. Conversely, for $KTaO_3$, the RMSE remains stable even as the cutoff radius increases, as illustrated in Fig.7.2a. However, when test structures are drawn from an NPT simulation — allowing volume to vary under a fixed pressure of 0GPa — the RMSE increases with the cutoff radius, as shown in Fig.7.2b. By expanding the training set to include 677 configurations from an NPT simulation over the 0K to 400K temperature range, the MLFF's performance becomes more consistent across both NVT and NPT datasets, as seen in Figs.7.2c and7.2d. Notably, this expanded NPT training dataset was not utilized for $KTaO_3$ in this study. Instead, the NVT dataset was preferred, as it offers faster computations while maintaining comparable accuracy within the relevant configuration space, as illustrated in Fig. 7.3b.

The expanded NPT training dataset provides a useful proof of concept, demonstrating the robustness of the choice to increase the cutoff radius. This approach offers the potential for broader applicability in future studies.

The larger error in the per-atom energy for $SrTiO_3$ compared to $KTaO_3$ is attributed to standard error propagation with system size, where the RMSE of the energy per atom follows a $1/\sqrt{N}$ scaling, with N representing the system size. This discrepancy arises because the test calculations for $KTaO_3$ are performed using larger supercells. Additionally, it is observed that the RMSE scaling for NPT validation in Fig. 7.2d is superior to that of $SrTiO_3$ in Fig. 7.1b.

A plausible explanation for this difference lies in the methodology used for $SrTiO_3$, where a Δ-ML approach is applied to construct an RPA-level MLFF on top of a baseline DFT model [27]. This approach, while effective, may lead to an increased risk of overfitting to the NPT configuration space as the cutoff radii are increased. This overfitting could explain the observed differences in RMSE behavior for $SrTiO_3$ relative to $KTaO_3$.

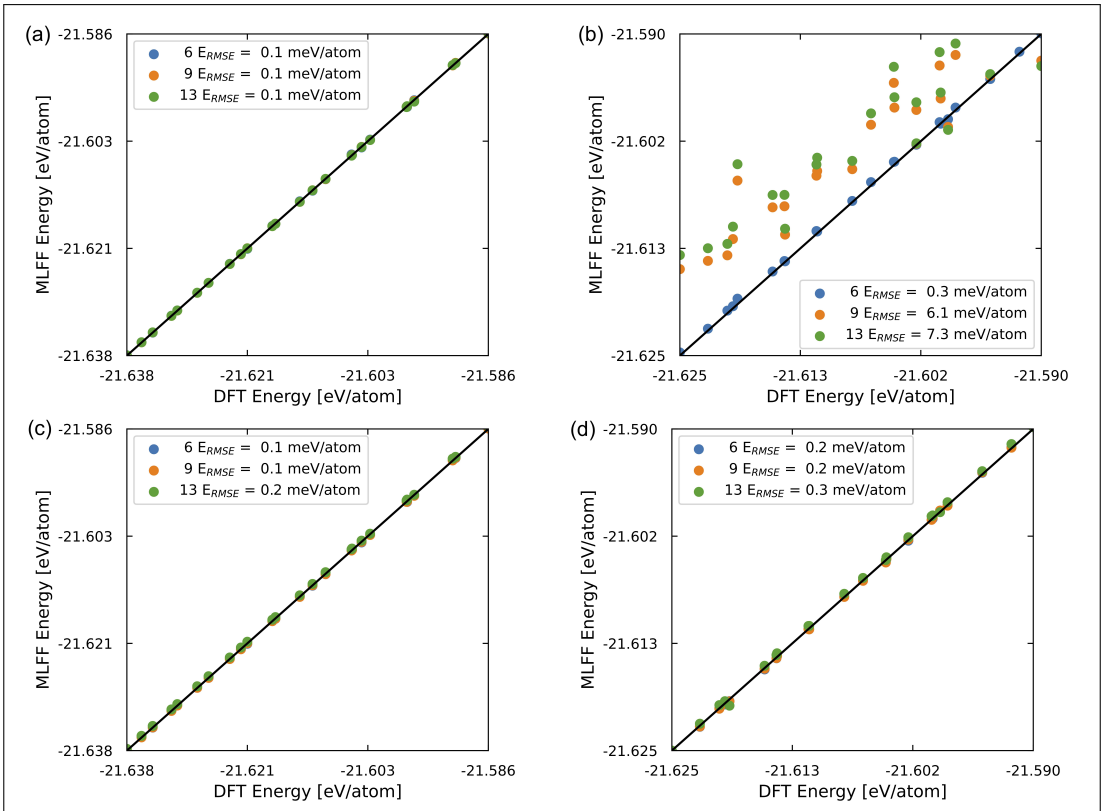


Figure 7.2. Energy RMSE in $KTaO_3$ for 25 test structures of 320 atoms using different values for the cut-off radii of the descriptors. The MLFF trained on structures sampled on the fly during MD in the NVT ensemble is validated on different test sets of random structures sampled from (a) NVT and (b) NPT MD. The MLFF trained on additional 677 structures sampled from the NPT ensemble is validated on the same (c) NVT and (d) NPT random structures, showing a consistent behaviour.

7.2.2 MLFF+SSCHA calculations

The SSCHA calculations in this work were fully automated using the Atomic Simulation Environment (ASE) package [134], which was enhanced with custom modifications to both ASE and SSCHA to streamline the process. This offers a more authomatized procedure when compared to the manual workflow presented in Section 4.2.

The self-consistent loop was executed by generating 800 ensembles for each population. Key parameters included setting the Kong-Liu effective ratio to 0.8, maintaining active preconditioning of the DM, and utilizing the "normal" root representation. To compute the free-energy Hessian at each temperature, which incorporates the static "bubble" correction to the self-consistent SSCHA frequencies [14], an ensemble of 5000 structures was employed.

The frequencies for the temperature-dependent anharmonic FE soft mode

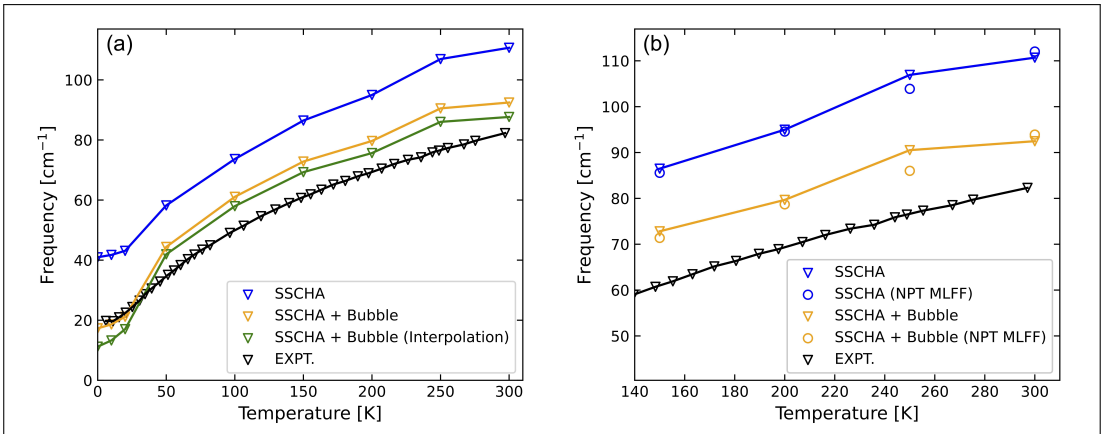


Figure 7.3. Temperature dependence of the FE mode frequency at the Γ-point in $KTaO_3$, together with experimental data [59]. (a) SSCHA frequencies at different levels of approximation, as obtained by employing the NVT MLFF. (b) Comparison between the NVT and NPT MLFF results in the temperature range $150 - 300$ K.

at Γ in $KTaO_3$, calculated using the free-energy Hessian (SSCHA + Bubble), exhibit strong agreement with experimental data [59], as displayed in Fig.7.3a. By interpolating the bubble correction on a $20\times20\times20$ **q**-grid[14], fully converged frequencies are obtained, differing by less than 6 cm^{-1} from the non-interpolated values across the entire temperature range. For computational efficiency, mobility calculations for $SrTiO_3$ and $KTaO_3$ are carried out using bubble-corrected dynamical matrices (free-energy Hessians) without interpolation.

As discussed in Section 7.2.1, validation tests confirm that NVT-MD simulations provide a reliable framework for constructing MLFFs that can be applied to SSCHA at the same fixed volume V. This is demonstrated in Fig. 7.3b, where the temperature dependence of the FE frequency at the Γ-point for $KTaO_3$ is shown. The frequency predictions from the NPT MLFF and the NVT MLFF are nearly identical within the temperature range relevant to mobility calculations, reinforcing the robustness of the NVT-based approach.

7.2.3 Renormalization of the Electron-Phonon Matrix Elements and Mobility Calculations

The electron mobilities are calculated using the BTE formalism as implemented in the EPW code [135–138], following the theoretical framework outlined in Section 5.2. As described in Section 5.1, this process requires the calculation of

electron-phonon matrix elements on coarse **k**- and **q**-point grids within the BZ (BZ):

$$g_{mn\nu}(\mathbf{k},\mathbf{q}) = \langle u_{m\mathbf{k}+\mathbf{q}} | \Delta_{\mathbf{q}\nu} v^{KS} | u_{n\mathbf{k}} \rangle_{uc}. \tag{7.1}$$

Here, $u_{n\mathbf{k}}$ represents the Bloch-periodic part of the KS electron wavefunction, and the integral is carried out over the UC. The $u_{n\mathbf{k}}$ wavefunctions are computed within the DFT framework using QE [139, 140]. The operator $\Delta_{\mathbf{q}\nu} v^{KS}$ denotes the variation of the KS potential with respect to the collective atomic displacement corresponding to a phonon mode ν with wavevector **q**. This operator can be further expressed as:

$$\Delta_{\mathbf{q}\nu} v^{KS} = l_{\mathbf{q}\nu} \sum_{\kappa\alpha} (M_0/M_\kappa)^{1/2} e_{\kappa\alpha,\nu}(\mathbf{q}) \partial_{\kappa\alpha,\mathbf{q}} v^{KS} \tag{7.2}$$

where $l_{\mathbf{q}\nu} = \left[\hbar/(2M_0\omega_{\mathbf{q}\nu})\right]^{1/2}$ represents the zero-point displacement amplitude, where M_0 is a reference mass that cancels out in Eq. (7.2), M_κ denotes the mass of atom κ, $\omega_{\mathbf{q}\nu}$ is the phonon eigenfrequency corresponding to branch ν, and $e_{\kappa\alpha,\nu}$ refers to the eigenvector in the Cartesian direction α. When $\omega_{\mathbf{q}\nu}$ is imaginary, as is the case for $SrTiO_3$, the operator $\Delta_{\mathbf{q}\nu} v^{KS}$ becomes ill-defined. As a result, the calculated electron-phonon matrix elements and the corresponding mobilities exhibit unphysical, spurious behavior.

Moreover, in the framework of the standard HA, the temperature dependence of phonon frequencies is neglected. This omission leads to an incomplete characterization of $\Delta_{\mathbf{q}\nu} v^{KS}$ in strongly anharmonic systems like $KTaO_3$ and $SrTiO_3$. To address these issues, we compute $\partial_{\kappa\alpha,\mathbf{q}} v^{KS}$ using standard DFPT as implemented in QE, employing a 4×4×4 reciprocal **q**-grid. However, instead of relying on harmonic phonon properties, we substitute $e_{\kappa\alpha,\nu}(\mathbf{q})$ and $\omega_{\mathbf{q}\nu}$ as obtained from the diagonalization of the anharmonic dynamical matrices, which are calculated on the same 4×4×4 reciprocal **q**-grid (as described in Section 6.2).

With this approach, we compute $g_{mn\nu}(\mathbf{k},\mathbf{q})$ for each temperature of interest, explicitly incorporating the temperature-dependent anharmonic $e_{\kappa\alpha}(\mathbf{q}\nu)$ and $\omega_{\mathbf{q}\nu}$. This method ensures a more accurate representation of the electron-phonon

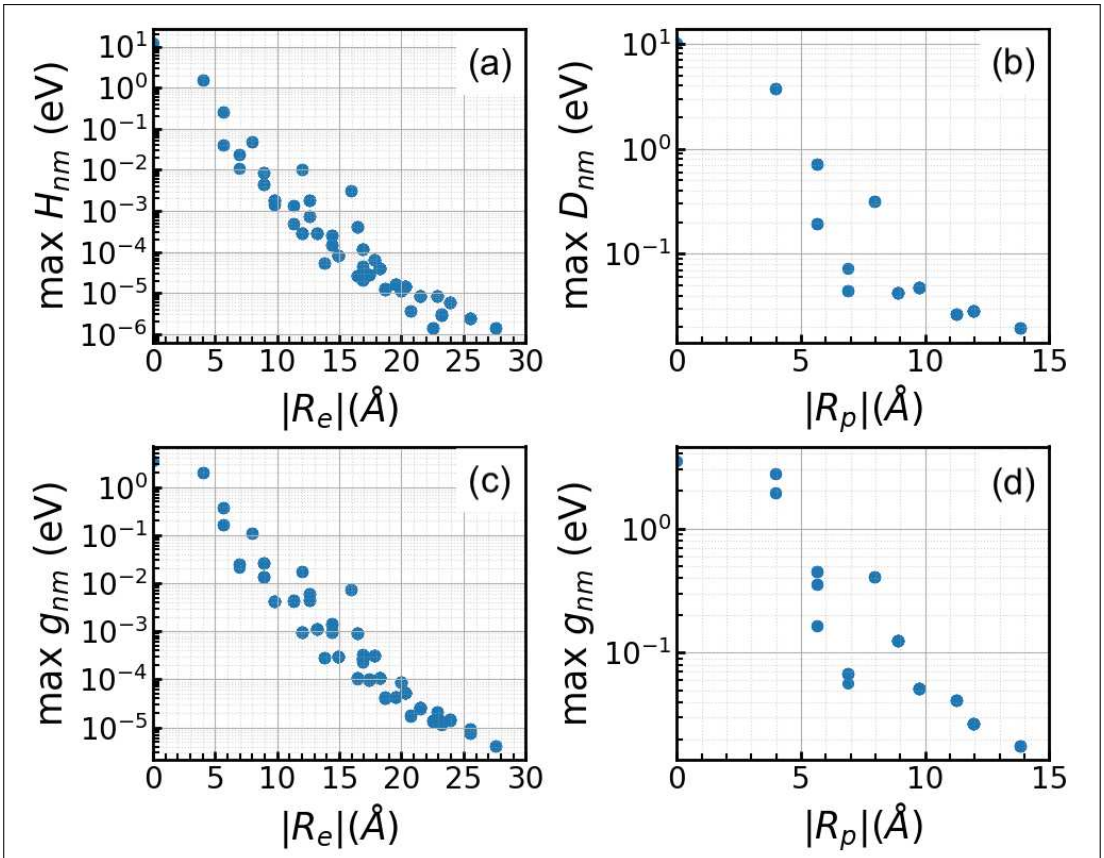


Figure 7.4. Decay of the real space tensors on the commensurate 4×4×4 supercell of $KTaO_3$, as a function of the distance of the Wannier center from the origin R_e or as a function of the distancd of the atoms from the origin R_p. In particular, the electronic term H_{nm} (a), the DM D_{nm} (b) and the electron-phonon matrix elements g_{nm} (c,d). Just the highest tensor element is plotted, for each distance.

interaction in anharmonic systems.

Lastly, the standard Wannier rotations are carried out to interpolate the electron Hamiltonian, the phonon DM, and the electron-phonon matrix elements from the coarse **k**- and **q**-grids to the fine reciprocal-space grids required for achieving convergence in the mobility calculations [65]. The equations governing this interpolation are detailed in Section 5.2. To facilitate this process, EPW employs the Wannier90 package [141], which generates maximally localized Wannier functions in real space [62, 63]. The real space tensors generated by WANNIER90 on the commensurate supercell as in intermediate step can be plotted in order to check for convergence with respect to the coarse BZ grids employed for the DFPT calculations. In Figure 7.4 and 7.4 we show such plots for $KTaO_3$ and $SrTiO_3$ respectively, without the inclusion of SOC.

The electron mobility for $KTaO_3$ and $SrTiO_3$ is computed both with and without SOC using the relaxation time approximation (RTA) and iterative Boltz-

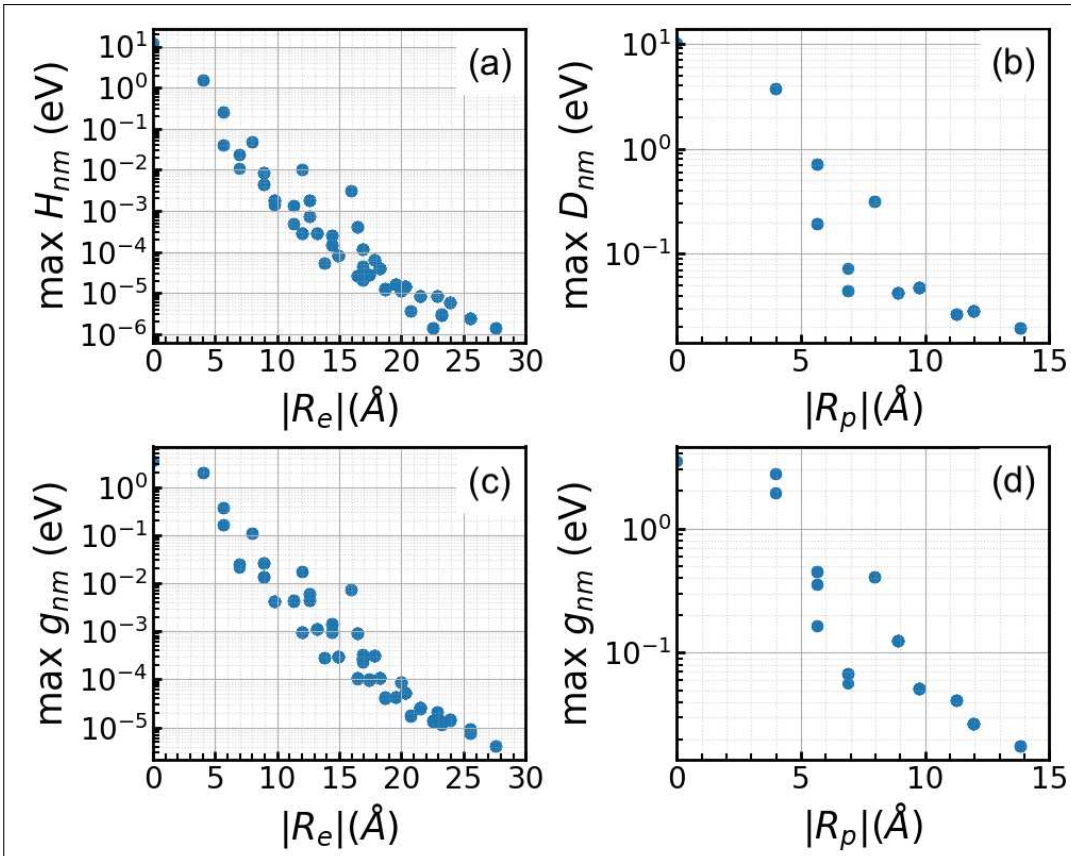


Figure 7.5. Decay of the real space tensors on the commensurate 4×4×4 supercell of $SrTiO_3$, as a function of the distance of the Wannier center from the origin R_e or as a function of the distancd of the atoms from the origin R_p. In particular, the electronic term H_{nm} (a), the DM D_{nm} (b) and the electron-phonon matrix elements g_{nm} (c, d). Just the highest tensor element is plotted, for each distance

mann transport equation (IBTE) approaches to the BTE. For both materials, the interpolation of the electron-phonon matrix elements is performed on a fine 100×100×100 **k**- and **q**-grid to ensure convergence of the mobility calculations. The convergence tests for both systems are presented in Fig. 7.6.

To match the doping concentrations observed in experimental samples [130, 131], a carrier concentration of $n = 0.8 \times 10^{17}$ is used for $SrTiO_3$, while for $KTaO_3$, a doping concentration of $n = 2.4 \times 10^{18}\,\mathrm{cm}^{-3}$ is adopted. It is worth noting that in the temperature range of 150–300 K, the experimental mobility is largely independent of doping concentration. Furthermore, the Hall mobility is calculated by introducing a magnetic field of 10^{-10} T.

The DFT and DFPT calculations are carried out for the cubic phases of $KTaO_3$ and $SrTiO_3$ using their experimental lattice constants of 3.9842 Å and 3.900 Å, respectively. This approach neglects the effects of lattice expansion with temperature. The calculations employ the PBE [72] functional along with fully

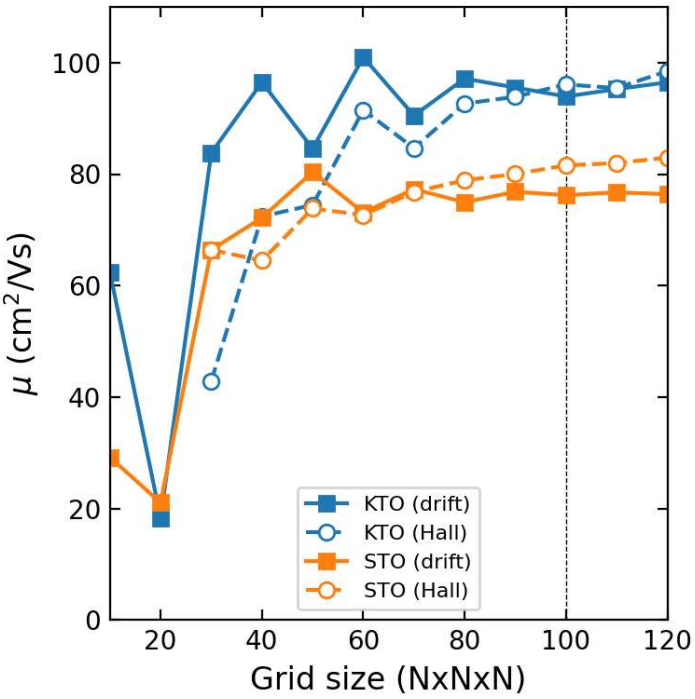


Figure 7.6. Convergence of the drift and Hall mobilities in $KTaO_3$ and $SrTO_3$ without SOC at 300 K. The dashed vertical line highlights the 100×100×100 reciprocal grid employed for all mobility calculations.

relativistic norm-conserving pseudopotentials sourced from PseudoDojo [142].

The computational setup includes an 8×8×8 Monkhorst-Pack **k**-point mesh, a plane-wave cutoff of 140 Ry, and an electronic convergence threshold of 10^{-16} Ry. The PBE functional is chosen for both $KTaO_3$ and $SrTiO_3$ due to the current lack of DFPT formalism implementation at the more accurate RPA and meta-GGA levels. However, RPA and meta-GGA calculations are still employed to obtain precise anharmonic dynamical matrices, as discussed in Section 7.2.2.

7.2.4 Mass Enhancement and Inclusion of Local Disorder

Local disorder or polymorphism plays a crucial role in shaping the electronic structure of many perovskite materials [133, 143], which is expected to significantly influence their mobilities. To incorporate the effects of local disorder into our calculations, we adopt the approach outlined in Refs. [133, 144], implemented via the ZG special displacement package within the EPW code [138].

For $SrTiO_3$ and $KTaO_3$, we use 2×2×2 supercells and introduce atomic displacements along the soft phonon modes, starting from their high-symmetry cubic structures. The magnitude of these displacements is set to match the zero-point displacement by assigning $\omega_{\mathbf{q}\nu}$ to its absolute value. Following this, we perform a geometry optimization in which the atomic positions are allowed to relax while the lattice constants are kept fixed. In this 2×2×2 supercell, a locally disordered network is observed for $SrTiO_3$, leading to an energy reduction of 9 meV per UC. Conversely, no energetically favorable disordered ground-state structure is found for $KTaO_3$, highlighting the significant presence of local disorder in $SrTiO_3$.

To visualize the impact of local disorder on the electronic structure of $SrTiO_3$ within the first BZ, we compute the electron spectral function using a band structure unfolding method based on plane waves [68, 145]. This calculation is carried out using the ZG package [138], enabling a detailed representation of how disorder affects the electronic structure.

For the calculation of band gap renormalization and effective mass enhancements at finite temperatures, we use the SDM approach [68], employing 6×6×6 supercells. These calculations rely on the anharmonic dynamical matrices obtained from SSCHA (as described in Section 6.2). The effective mobility mass within the SDM is computed as the harmonic mean, following the formalism proposed in Ref. [108]:

$$m = \frac{3m_x m_y m_z}{m_x m_y + m_x m_z + m_y m_z}. \tag{7.3}$$

Here, $m_{x,y,z}$ are determined using finite differences of the energy at the Γ-point, taking the average of the three lowest eigenvalues at the CBM. The effective masses presented in Table 7.2 are calculated using Eq. (7.3).

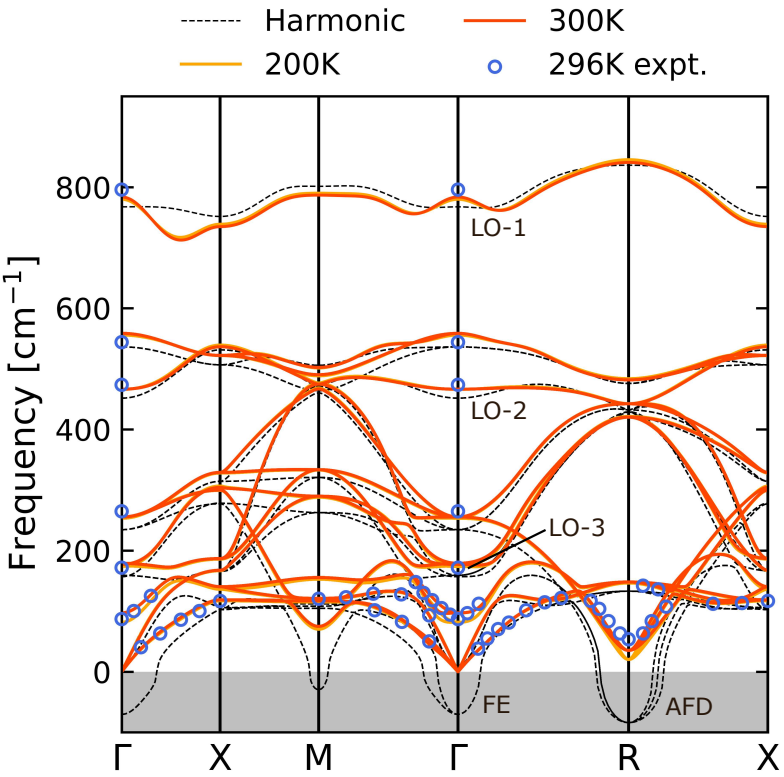


Figure 7.7. Temperature-dependent anharmonic phonon dispersion (solid lines) and the harmonic phonon dispersion obtained using PBE (dashed lines) in $SrTiO_3$. Experimental data 296 K are also shown (circles) [146, 147].

7.3 Results and discussion

$SrTiO_3$

The anharmonic phonon dispersion near room temperature as calculated through MLFF+SSCHA shown in Fig. 7.7 is in excellent agreement with the experimental dispersion measured at 296 K [146, 147]. At the harmonic level, $SrTiO_3$ exhibits imaginary frequencies for the FE and AFD lowest energy modes, which lead to spurious divergencies of the electron-phonon matrix elements, as shown in Figure 7.9a.

To ensure accurate mobility calculations within the HA, a phonon cut-off frequency ω_{cut} is introduced. This approach involves setting $g_{mn\nu}(\mathbf{k}, \mathbf{q}) = 0$ for phonon modes ν and wavevectors $\mathbf{q}$ that satisfy $\omega_{\mathbf{q}\nu} \leq \omega_{\text{cut}}$. A cut-off value of 10 meV is selected, as the mobility stabilizes to converged values around this threshold. Under this configuration, an overestimation of electron mobility is

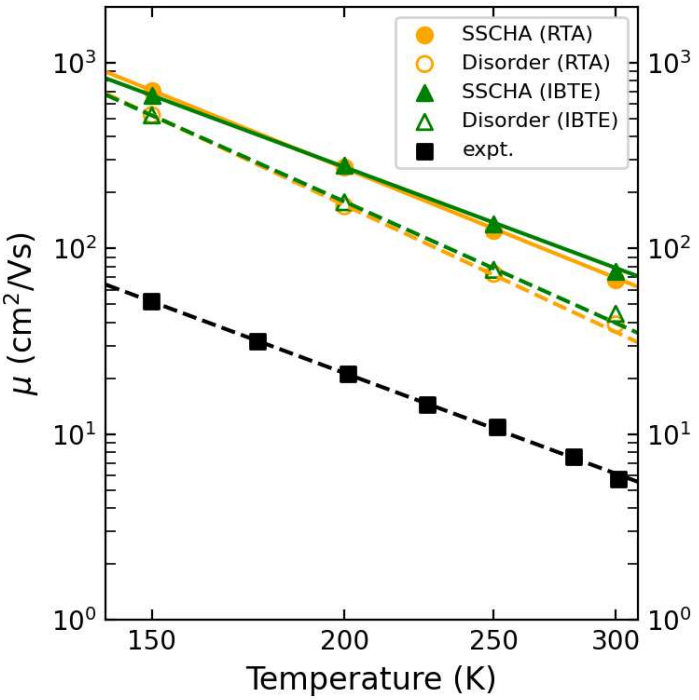


Figure 7.8. Electron mobility calculations in $SrTiO_3$ using SSCHA temperature-dependent dynamical matrices substitution. The BTE is solved via RTA (orange filled circles) and IBTE (green filled triangles). Local disorder is included by further substitution of the high-symmetry unit cell electronic eigenvalues with those of the disordered supercell at RTA (orange empty triangles) and IBTE (green empty triangles) level. Both the calculated and the experimental mobilities [130] are fitted using Eq. (7.4). All the computed mobilities are rescaled by Eq. (7.5).

observed at the lower end of the 150–300 K temperature range, where these low-energy modes exhibit non-negligible interaction with charge carriers, as depicted in Figure 7.10.

In addition to the relatively weak interaction with the FE and AFD modes, the primary scattering channels are the less temperature-sensitive LO-1, LO-2, and LO-3 modes. The LO-1 mode interacts throughout the entire BZ (BZ), while the LO-3 mode exhibits strong interaction only near the Γ-point, as displayed in Figure 7.9a and Figure 7.9b.

At low temperatures, charge carriers are predominantly scattered by lattice impurities, while at higher temperatures, electron-phonon scattering becomes the dominant scattering mechanism. In this high-temperature regime, the Hall mobility is expected to follow a power-law relationship given by:

$$\mu_H = A \times T^{-\gamma}. \tag{7.4}$$

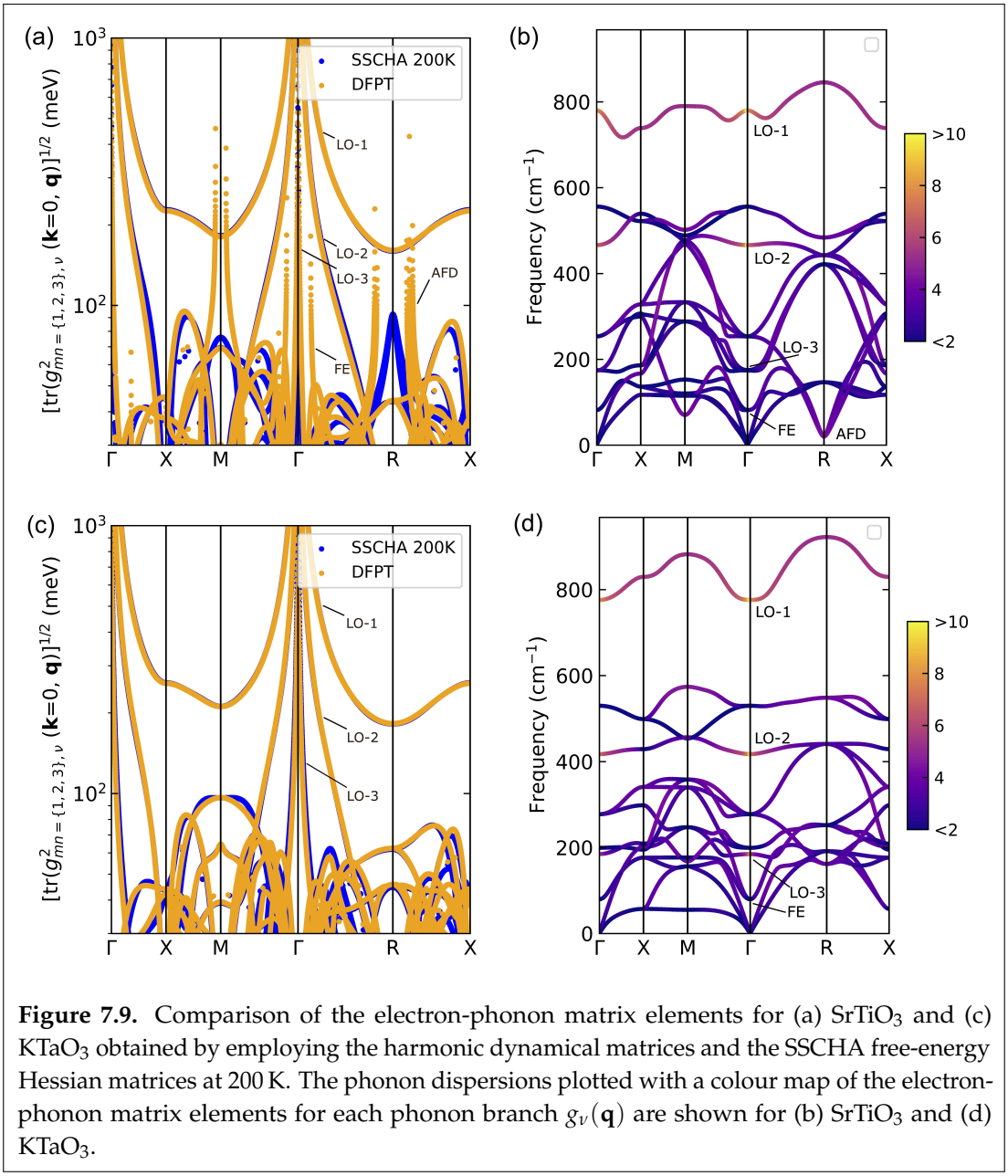


Figure 7.9. Comparison of the electron-phonon matrix elements for (a) $SrTiO_3$ and (c) $KTaO_3$ obtained by employing the harmonic dynamical matrices and the SSCHA free-energy Hessian matrices at 200 K. The phonon dispersions plotted with a colour map of the electron-phonon matrix elements for each phonon branch $g_\nu(\mathbf{q})$ are shown for (b) $SrTiO_3$ and (d) $KTaO_3$.

A fit to the experimental data shown in Fig. 7.8 gives a temperature exponent of $\gamma = 3.08$. When using the HA, the computed data deviates from this power-law behavior, as illustrated in Figure 7.10. However, employing anharmonic SSCHA dynamical matrices restores the expected temperature dependence, as seen in Fig. 7.8.

The IBTE calculations produce a value of $\gamma = 3.07$, which aligns very closely with the experimental value. In contrast, the RTA approximation yields a slightly higher exponent of $\gamma = 3.34$. Interestingly, $SrTiO_3$ follows a universal scaling law $\mu \propto T^{-3.3}$, similar to that found for halide perovskites, where the LO-1 mode serves as the primary scattering channel [148]. These results are consistent with

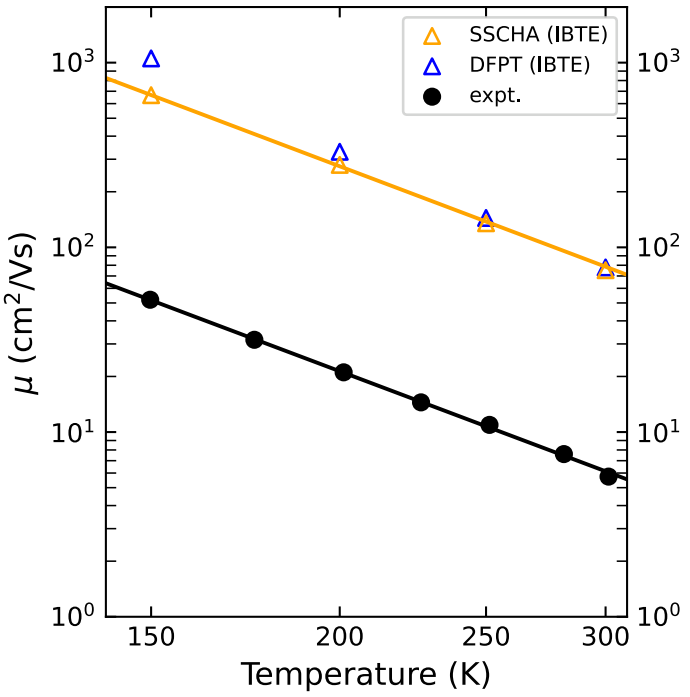


Figure 7.10. Mobility in $SrTiO_3$ as computed from harmonic dynamical matrices with imaginary frequencies (blue markers) and from the SSCHA matrices (orange markers). The experimental data are in black.

prior computational studies [121].

It is important to note the significant role of the temperature dependence of the anharmonic dynamical matrices. If these matrices are fixed to their values at 150 K, rather than allowing them to evolve with temperature, the computed mobility is underestimated. This underestimation, illustrated in Fig. 7.11, arises from the failure to account for the hardening of the FE and AFD modes at higher temperatures, which results in an overestimation of the scattering as predicted by Eq. (7.2).

The overestimation of the calculated electron mobility for $SrTiO_3$ relative to experimental values is significantly more pronounced than what is typically observed in previous BTE calculations for standard semiconductors [95]. To address this discrepancy, we investigate several potential factors that could contribute to the overestimation.

One key factor is the inclusion of SOC. As illustrated in Figure 7.12, incorporating SOC results in a 28 meV splitting of the conduction bands near the CBM, along with slight modifications to the electronic effective masses. The effective masses with and without SOC are summarized in Table 7.1.

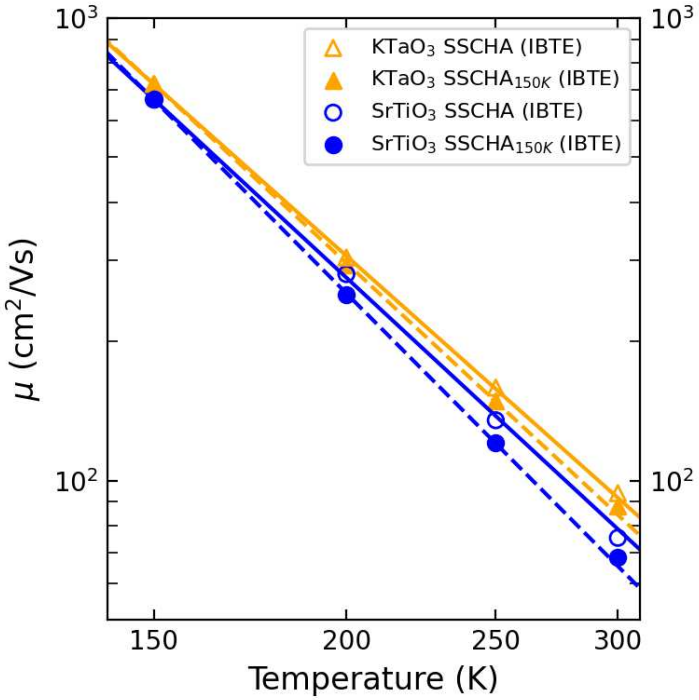


Figure 7.11. Comparison of the mobilities obtained employing the correct SSCHA matrices at each temperature in $SrTiO_3$ (blue empty circles) and $KTaO_3$ (orange empty triangles) and the respective results using the SSCHA matrices calculated at 150 K (blue and orange filled markers).

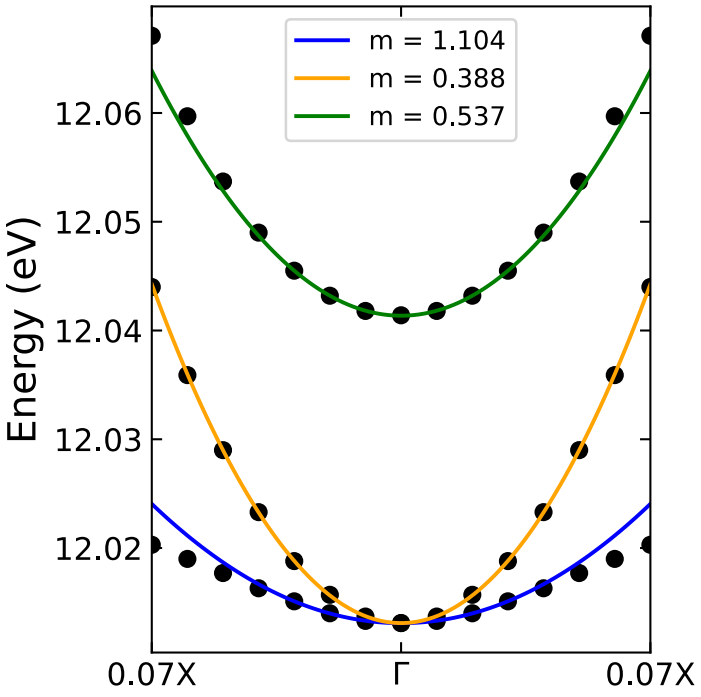


Figure 7.12. Parabolic fit of the three bottom conduction bands in $SrTiO_3$, calculated with SOC. Each band is doubly degenerate. The electron effective masses are in units of the free electron mass.

Table 7.1. Conduction-band effective masses with|without SOC coupling for $SrTiO_3$ in the ordered (cubic) and disordered structure, and for $KTaO_3$ in the ground-state cubic structure. m^*_{he} stands for the heavy electron mass, $m^*_{le_1}$ and $m^*_{le_2}$ for the light electron masses.

	Path	m^*_{he}	$m^*_{le_1}$	$m^*_{le_2}$
$SrTiO_3$	$\Gamma - R$	0.62|0.67	0.53|0.53	0.57|0.53
	$\Gamma - X$	1.10|6.37	0.39|0.39	0.54|0.39
	$\Gamma - M$	0.74|0.88	0.47|0.64	0.54|0.39
$KTaO_3$	$\Gamma - R$	0.46|0.50	0.38|0.41	0.44|0.41
	$\Gamma - X$	0.78|5.30	0.28|0.30	0.45|0.30
	$\Gamma - M$	0.55|0.65	0.33|0.50	0.44|0.30

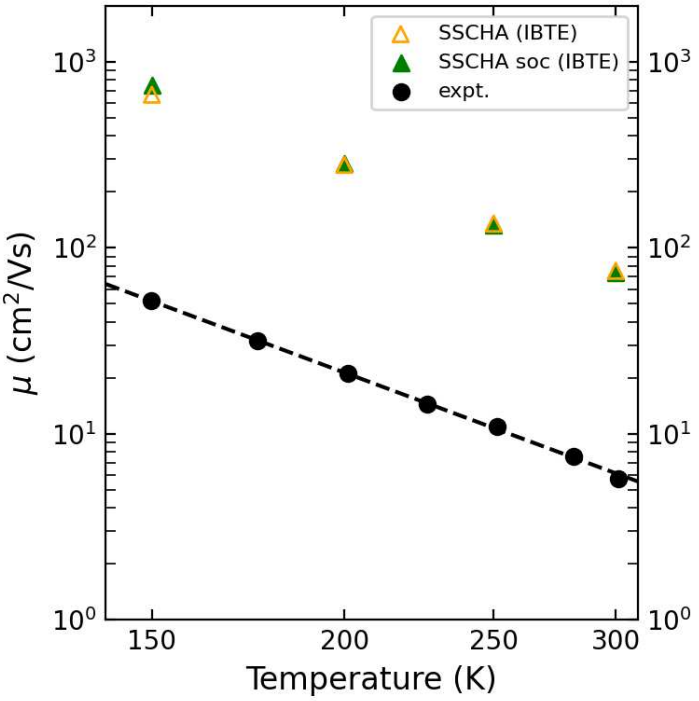


Figure 7.13. Mobility in $SrTiO_3$ as computed from the SSCHA matrices including (green filled triangles) and neglecting (orange empty triangles) SOC. In black markers, the experimental data.

Hence, the inclusion of SOC has minimal impact on the electron mobility, as suggested by a simplified transport model [149] and further confirmed by our calculations, which are displayed in Figure 7.13. This result indicates that the observed overestimation of mobility cannot be attributed to SOC effects.

Utilizing a more accurate treatment of electronic correlation effects via the HSE06 hybrid functional results in little to no change in the effective masses [150].

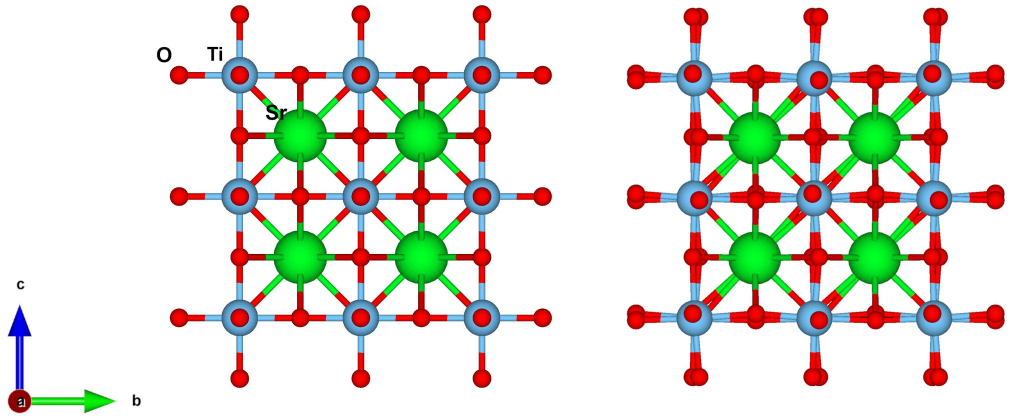


Figure 7.14. Comparison between the $SrTiO_3$ symmetric cubic structure (left) and the disordered one (right).

However, our computed electronic dielectric constant of 6.17 overestimates the experimental value of 5.62 [151], a well-known limitation of DFT calculations. By rescaling the mobility as [108]:

$$\mu^{\text{screen}} = \mu \times (\epsilon^{\text{DFT}}/\epsilon^{\text{exp}})^2, \tag{7.5}$$

Although a 17% reduction is accomplished, it remains insufficient to resolve the substantial overestimation, which exceeds 800% relative to the experimental measurement at 300 K.

A key aspect that has thus far been overlooked is the impact of local disorder, which shifts the equilibrium atomic positions within each UC while preserving the overall lattice symmetry. Upon relaxing a $2\times2\times2$ supercell of $SrTiO_3$ with broken symmetry, as elaborated in Section 7.2.4, a novel ground state emerges, characterized by an energy reduction of 9 meV per UC. This result aligns with the findings of Ref.[133]. The resulting relaxed structure is depicted in Figure 7.14.

The unfolded band structure depicted in Fig. 7.15 reveals low-weight features at energies notably higher than the CBM. However, since only electronic states within a 0.2 eV range from the CBM actively contribute to conduction, these features are irrelevant for our mobility calculations. A significant increase in the curvature of the CBM is observed, leading to an average electronic effective mass of $m^*_{\text{dis}} = 0.58\, m_e$, which is 1.22 times larger than the $m_0 = 0.49\, m_e$ obtained for the symmetric UC. The resulting mobility decrease estimated through [108]:

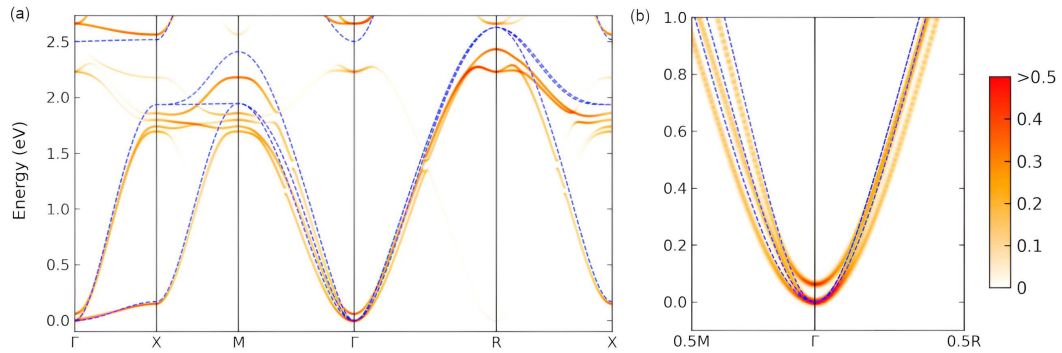


Figure 7.15. (a) Electron spectral function (colour map) of $SrTiO_3$ resulting from unfolding the bands of the 2×2×2 disordered supercell onto the high-symmetry path of the cubic unit cell. The band structure for the symmetric UC is shown as dashed blue line. Both CBMs have been shifted to zero. (b) Zoom on the 0.5M-Γ-0.5R path, where only energies close to the CBM are shown.

$$\mu^* = \mu \times (m^*/m_0)^{-1}. \tag{7.6}$$

This results in a 22% decrease in mobility. the electronic band gap undergoes a significant increase of 0.31 eV relative to the 1.92 eV of the symmetric UC. Table 7.2 provides a summary of the overall mobility overestimation with respect to experimental data at 300K, considering both the discussed and subsequent levels of approximation, along with the corresponding band-gap corrections. Moreover, a 62 meV splitting is observed near the CBM, which is twice the magnitude of the splitting induced by the inclusion of SOC.

To compare the approximate mobility rescaling via Eq. (7.6) with a full mobility calculation for the disordered structure, we Wannierize the new electronic eigenvalues obtained for the disordered configuration and incorporate them into the BTE, along with the previously computed SSCHA matrices. The construction of Wannier functions for the 3 lowest conduction bands begins with the KS wavefunctions and energies calculated on a 4×4×4 k-point grid, consistent with the 8×8×8 grid used for the UC. For each k-point, we select the well-defined eigenvalues with substantial spectral weight, ensuring the identification of 3 eigenvalues per k-point, mirroring the procedure used for the UC. The accuracy of the Wannier interpolation of the unfolded bands, illustrated in Fig. 7.16, confirms the reliability of this approach.

We observe a mobility reduction of 28% at 150 K and 43% at 300 K relative

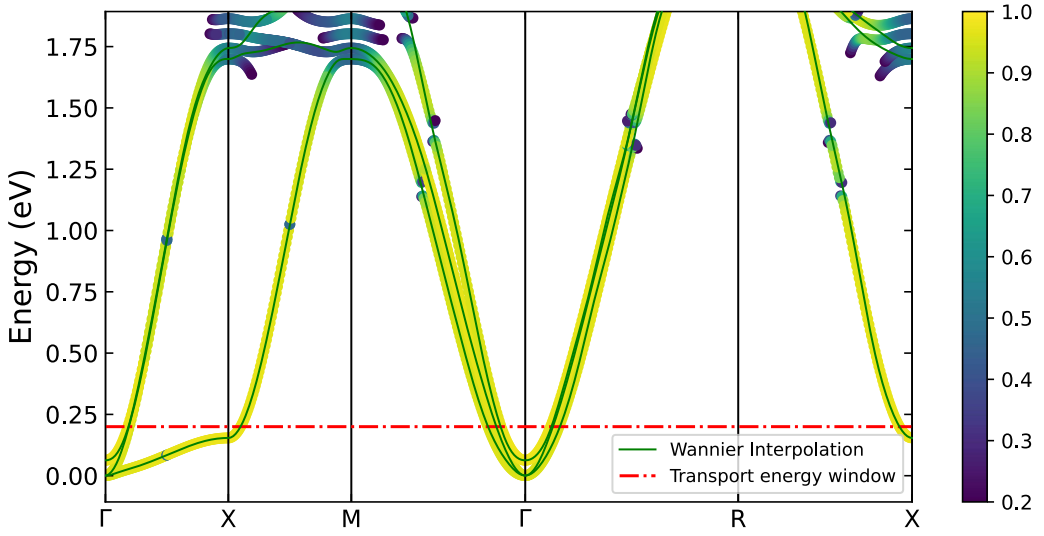


Figure 7.16. Spectral function of disordered $SrTiO_3$ calculated using a $2 \times 2 \times 2$ supercell and unfolded. Only the peaks with spectral weight larger than 0.2 are shown. The Wannier interpolation on the high-symmetry path accurately reproduces the unfolded band structure around the energy window contributing to electronic transport, validating the eigenvalue extraction and Wannier interpolation procedure.

to the previous estimate for the symmetric UC, as illustrated in Fig. 7.8. The trend continues to follow the power-law relationship described by Eq. (7.4) with $\gamma = 3.71$. Notably, the reduction in computed mobility surpasses the decrease predicted by Eq. (7.5), underscoring the significant impact of local disorder on carrier transport, beyond a simple mass rescaling effect.

A crucial correction arises from incorporating the influence of electron-phonon coupling on carrier effective masses. Using the SDM approach [68], we calculated the band gap and mass renormalization at 300 K. This was achieved by employing the ZG configuration, paired with its antithetic counterpart [133], within a $6\times6\times6$ supercell of the symmetric UC. The 300 K SSCHA DM was used to generate the ZG displacements. This approach yielded a 165 meV reduction in the band gap relative to the clamped-ion value in the primitive cell, consistent with the renormalization reported in Ref. [133]. The resulting effective mass, $m^*_{\text{el-ph}} = 2.21\, m_0$, aligns with the QP curvature obtained through the cumulant Green's function approach [122].

When considering the 300 K ZG displacements applied to the locally disordered structure, the combined effects of disorder and electron-phonon coupling are captured. The renormalization of the electronic structure becomes even more

pronounced, with a 236 meV reduction in the band gap relative to the disordered structure and a net increase of 74 meV compared to the symmetric UC. The renormalized effective mass reaches $m^*_{\text{dis+el-ph}} = 2.89\, m_0$, equivalent to $1.38\, m_e$, in agreement with experimental data [126, 127]. The electron-phonon renormalization of both the band gap and the effective mass is therefore more substantial in the disordered structure than in the symmetric one. Importantly, by incorporating the combined effects of local disorder, electron-phonon coupling, and dielectric rescaling on the effective mass, a more reasonable mobility overestimation of 290% is obtained for $SrTiO_3$ at 300 K relative to the experimental value.

Table 7.2. Band-gap renormalization (ΔE_{gap}), electron effective mass enhancement (m^*/m_0) and mobility overestimation at 300 K with respect to the experimental value, after dielectric rescaling. m_0 is the electron effective mass obtained in the UC (sym). The other calculations correspond to the inclusion of local disorder (dis), electron-phonon coupling (el-ph), and the combination of both effects (dis+el-ph).

		ΔE_{gap} (meV)	m^*/m_0	μ^*/μ^{exp}
$SrTiO_3$	sym	-	1	838%
	dis	310	1.22	686%
	el-ph	-165	2.21	378%
	dis+el-ph	74	2.89	290%
$KTaO_3$	sym	-	1	345%
	el-ph	-193	1.39	248%

$KTaO_3$

We begin by presenting the temperature-dependent anharmonic phonon dispersions of $KTaO_3$, displayed in Fig. 7.17, which show excellent agreement with inelastic neutron scattering measurements [152]. The emergence of the incipient FE instability is found to be strongly influenced by the choice of the exchange-correlation functional. The harmonic phonon dispersion computed using the PBE functional predicts a stable Γ-point FE mode. Conversely, the dispersion obtained with the SCAN functional for a 4×4×4 supercell (consistent with the q-grid used for PBE) reveals a strongly unstable FE distortion. However, stability

is restored when zero-point quantum energy and anharmonic phonon effects are incorporated via the MLFF+SSCHA approach, as illustrated in Fig. 7.17. This result significantly improves upon the findings discussed in Section 4.3 for the temperature evolution of the soft FE mode. The improved agreement with experimental data is attributed to the adoption of more accurate pseudopotentials and the use of a larger 4×4×4 supercell.

Similar to $SrTiO_3$, the temperature-insensitive LO-1, LO-2, and LO-3 modes dominate the scattering processes, while the temperature-dependent contribution is driven by the FE mode, as displayed in Fig. 7.9c and Fig. 7.9d. By fitting the experimental data [131] in Fig. 7.18 using the power law from Eq. (7.4), a value of $\gamma = 2.96$ is obtained, closely matching the temperature-dependent behavior observed for $SrTiO_3$. The calculated mobility using the IBTE yields a similar value of $\gamma = 2.97$, while the RTA approach gives $\gamma = 3.17$. As observed in $SrTiO_3$, fixing the 150 K dynamical matrices results in an underestimation of electron mobility at room temperature due to the omission of the hardening of the FE mode, as demonstrated in Fig. 7.11.

As with $SrTiO_3$, we investigate the potential causes of the mobility overestimation relative to experimental data. The SOC-induced splitting of 314 meV near the CBM results in only minor changes to the electron effective masses, as detailed in Table 7.1. However, as shown in Fig. 7.18, the mobility experiences a significant increase compared to non-relativistic calculations. The power-law exponent shifts to $\gamma = 3.36$ for IBTE and $\gamma = 3.48$ for RTA. This pronounced mobility enhancement caused by SOC is therefore attributed to the splitting of the 5*d* manifold of the heavier Ta ion.

The computed dielectric constant of 5.07 slightly exceeds the experimental value of 4.6 [153]. Applying the dielectric rescaling according to Eq. (7.5), the mobility is reduced by 18%, mirroring the behavior observed in $SrTiO_3$. Consequently, at 300 K, the mobility is overestimated by 345% relative to the experimental data, which is significantly lower than the overestimation seen for $SrTiO_3$, as summarized in Table 7.2.

Unlike $SrTiO_3$, no local disorder is found in the ground state of $KTaO_3$ when calculated using DFT-PBE within a 2×2×2 supercell. Similar to the approach

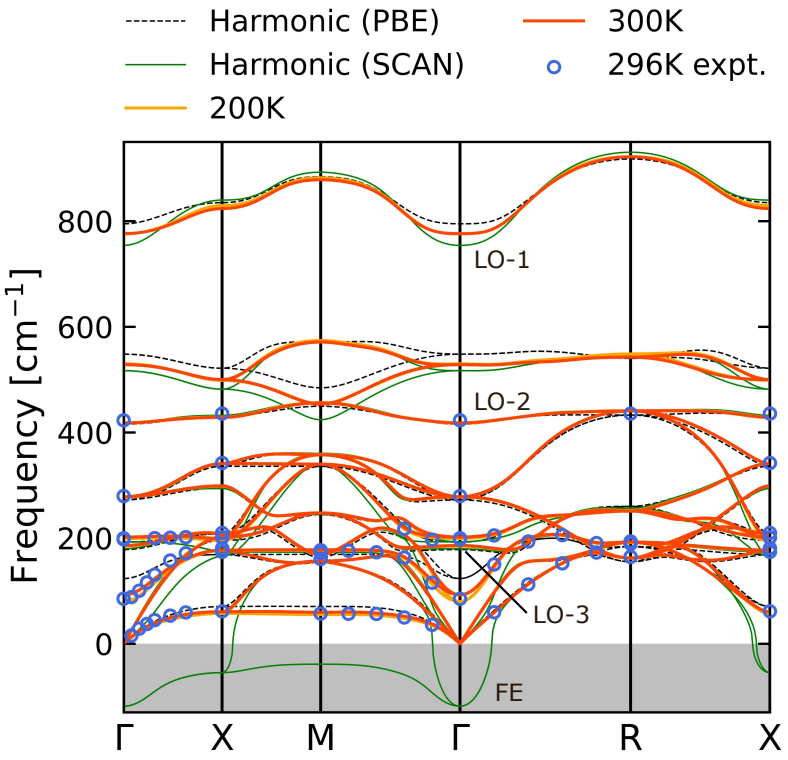


Figure 7.17. Stable harmonic phonon dispersion of $KTaO_3$ obtained using PBE (dashed black lines), unstable harmonic dispersion through the SCAN-based MLFF (solid green lines) and the temperature-dependent anharmonic dispersion using the SCAN-based MLFF in SSCHA (solid orange and red lines). Experimental data at 296 K are also shown [152].

for $SrTiO_3$, we compute the band gap renormalization and the electron effective mass enhancement induced by the electron-phonon interaction using the SDM method. At 300 K, the band gap renormalization is found to be -0.193 meV, comparable to the result obtained for $SrTiO_3$. However, in stark contrast to this result, the effective mass is renormalized to $m^*_{\text{el-ph}} = 0.57\, m_e$, representing a 1.4-fold increase over the clamped nuclei value of $m_0 = 0.41\, m_e$. As a result, the total mass renormalization in $KTaO_3$ is considerably smaller than that observed in the locally disordered $SrTiO_3$.

After incorporating the effects of dielectric screening and mobility rescaling due to effective mass renormalization, the final mobility overestimation is reduced to 248% relative to the experimental value at 300 K. This result is in close alignment with the analogous overestimation of 290% observed for $SrTiO_3$.

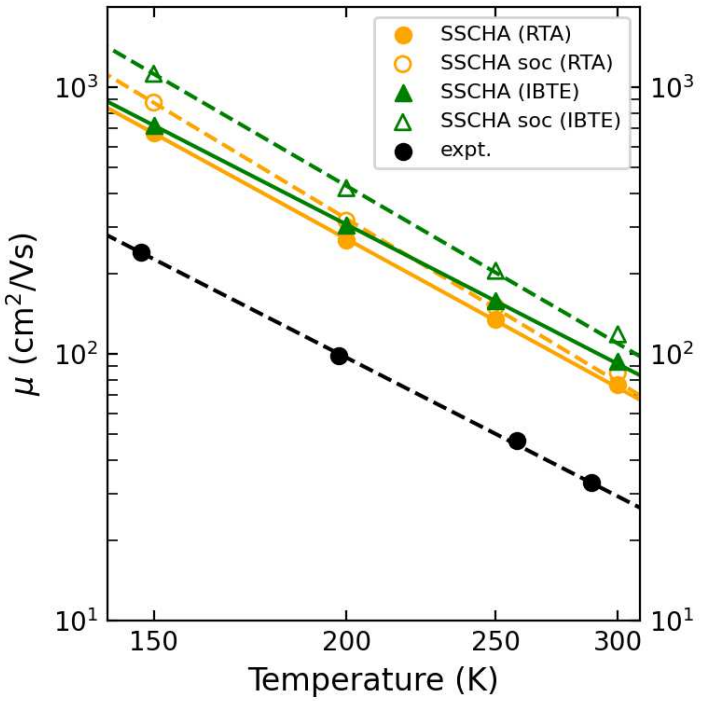


Figure 7.18. Electron mobility calculations in $KTaO_3$ using SSCHA temperature-dependent dynamical matrices at RTA (orange filled circles) and IBTE (green filled triangles) level. The same calculations are repeated including SOC (empty symbols). Both the IBTE and the experimental mobilities [131] are fitted using Eq. (7.4). All the computed mobilities are rescaled by Eq. (7.5).

CHAPTER 8

Polarons in $KTaO_3$ and $SrTiO_3$

In this Chapter, we analyze the possibility of polaron formation in $KTaO_3$ and $SrTiO_3$ at 0 K and at different strain conditions in the case of $KTaO_3$. In Chapter 7 we have underlined the occurrence of a QP peak in the experimental ARPES spectra of $SrTiO_3$ due to the presence of an electron-polaron. We hypothesize a similar phenomenon may occur in $KTaO_3$, due to due the analogies between the two materials, as our results obtained for the electron mobility showed.

In Section 8.1, we introduce the concept of polaron, its experimental evidences, and the available computational methods for modeling polarons.

In Section 8.2, we describe the setup adopted in order to predict the polaron formation energy in $KTaO_3$ and $SrTiO_3$, following the theory summed up in Section 5.4.

In Section 8.2.1 and Section 8.2.2, we discuss the electron and hole polaron formation mechanisms in both materials and highlight the occurrence of a more favorable small hole polaron in uniaxially strained FE $KTaO_3$, when compared to the cubic PE case.

8.1 Introduction

A polaron is a QP formed due to the interaction between an electron (or hole) and lattice vibrations (phonons), where the charge carrier becomes "dressed" with a cloud of phonons [154–157]. In other words, the interaction with the lattice vibrations may result in a distortion of the lattice and a localization of the electron (hole). In certain compounds, the polaron solution comes as a more favorable ground state than the delocalized carrier picture. Polarons play a significant role in determining the electronic, optical, and transport properties of materials, especially in systems where electron-phonon coupling is strong, such as perovskites, organic semiconductors, and transition metal oxides.

Experimentally, the presence of a polaronic state can be inferred by using several techniques that directly or indirectly probe the interactions between charge carriers and the lattice or by observing direct traces of carrier localization in doped semiconductors. A summary of the available experimental techniques can be found in the review in Ref. [158], as well as a comprehensive summary of the computational techniques for polaron modeling.

The main limitation of many computational approaches for polaron modeling lies in the necessity of adopting effective Hamiltonians, where the electron-phonon interaction is either averaged or simplified to the contribution of a specific phonon. When resorting to DFT, it is the use of large supercells [159]. The former approaches often struggle in numerical comparisons with experiments, while the latter is not viable when dealing with large polarons. This limitation can be overcome by the DFPT UC methods recently developed by Sio et al.[69, 70], which was review in Section 5.4. In the next section, we calculate the electron and hole polaron formation energies in $KTaO_3$ and $SrTiO_3$ using precisely this method. This allows for the direct assessment of both the wavefunction localization and associated lattice distortions, while leveraging standard ground state calculations of the KS Hamiltonian, phonon vibrational spectrum and electron-phonon matrix elements.

8.2 Methods

The computational setup adopted for the DFPT calculations is the same as the one adopted in Section 7.2.3 for both $KTaO_3$ and $SrTiO_3$. In the case of the electron polaron, we consider the lowest three conduction bands of $KTaO_3$ and $SrTiO_3$ in the evaluation of Eq. (5.28), and the 9 highest valence bands in the case of the hole polaron. In $KTaO_3$ and $SrTiO_3$, the conduction bands are characterized by Ta 5*d* orbitals and Ti 3*d* orbitals respectively, while the valence bands predominantly exhibit O 2*p* orbital character. When including SOC in the case of $KTaO_3$, the number of bands needs to be doubled, and Eqs. 5.28 and 5.29 become computationally more expensive.

The calculations have been performed for the cubic QPE phases of $KTaO_3$ and $SrTiO_3$, while the FE phase of $KTaO_3$ has been created by applying a 1% uniaxial strain and relaxing the internal degrees of freedom by the use of SSCHA. This is the 0 K strained structure reported in Figure 4.9a. For the electron polaron calculations, we adopt the DFPT HA DMs as described in 7.2.3, while in the hole polaron case we consider also anharmonic effects by employing the SSCHA at 0 K as computed through the MLFF+SSCHA workflow (see Section 4.2), thus renormalizing the electron-phonon matrix elements. The DFPT DMs matrices are employed to the higher numerical stability, which is relevant for the barely stable large polaron in $KTaO_3$ and $SrTiO_3$.

8.2.1 Electron Polaron

The electron polaron localization as a function of the supercell size in cubic $KTaO_3$ and $SrTiO_3$ is presented in Figure 8.1a, showing an analogous behavior for the two materials. Up to a supercell size of $30\times30\times30$, the polaron appears to be delocalized on a 2D plane and localized in one direction, as shown in the $KTaO_3$ case in Figure 8.2. By increasing the supercell size, the spurious unidirectional constraint falls and the polaron likely becomes localized in all three directions. This is seen as a linear regime for the formation energy, as expected for a localized polaron [69, 70] (this interpretation of the convergence process needs to be investigated further). The extrapolated formation energy for

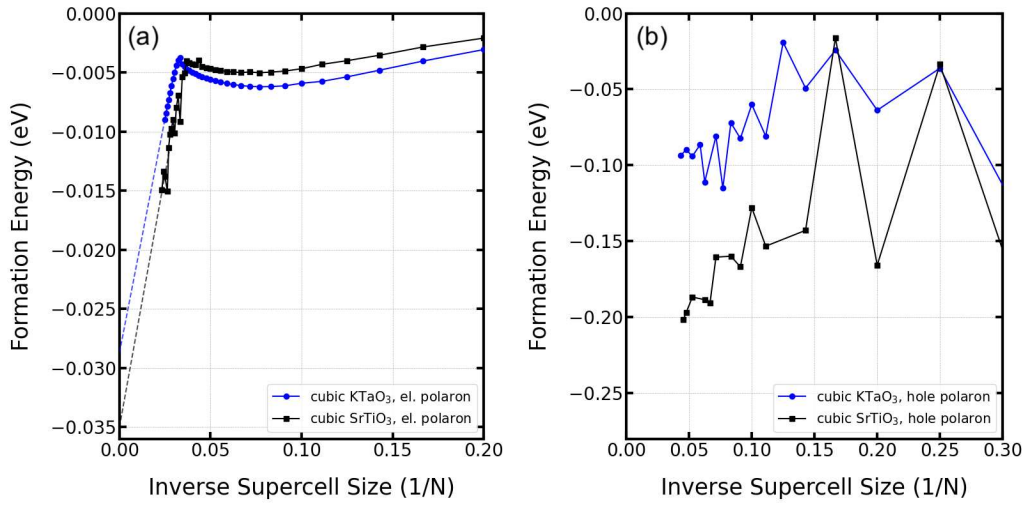


Figure 8.1. on the left, the formation energy of the electron polaron as a function of the supercell size in cubic $KTaO_3$ (blue markers) and $SrTiO_3$ (black markers). A linear fit of the points in the localized polaron regime is performed. On the right, the formation energy of the hole polaron in cubic $KTaO_3$ (blue markers) and $SrTiO_3$ (black markers).

$KTaO_3$ in the limit of infinite supercell size is of 0.029 eV, close to the value of 0.035 eV found for $SrTiO_3$. These values are small and signal a polaron solution which is just slightly more favorable than the delocalized electron solution. The main contributions come from the eigenstates at the bottom of the conduction band near Γ, as can be observed from the distribution of the $A_{n\mathbf{k}}$ coefficients (Eq. (5.28)) in Figure 8.2c. The lattice distortion is driven mostly by the LO modes near the Γ point, with marginal contributions coming from the acoustic modes and lowest TO soft mode, as can be seen in the distribution of the $B_{\mathbf{q}\nu}$ coefficients (Eq. (5.29)) in Figure 8.2d. Totally analogous results are obtained for $SrTiO_3$, here skipped for sake of brevity.

The electron-phonon matrix elements are the central quantities of this methodology, and in Chapter 7, Figure 7.9, we have shown the almost identical intensity of the electron-phonon coupling for the conduction bands around Γ in $KTaO_3$ and $SrTiO_3$. This reflects in very similar computed electron mobilities, and it likewise reflects in very similar polaronic localization energies.

We expect a very similar polaronic behavior for the AFD phase of $SrTiO_3$, since the lattice distortions are of around four orders of magniutude smaller than the lattice parameter. These results show that both $SrTiO_3$ and $KTaO_3$ can indeed host Fröhlich-type polarons, which can explain the overestimation of the electron mobility as calculated through the BTE method in Chapter 7.

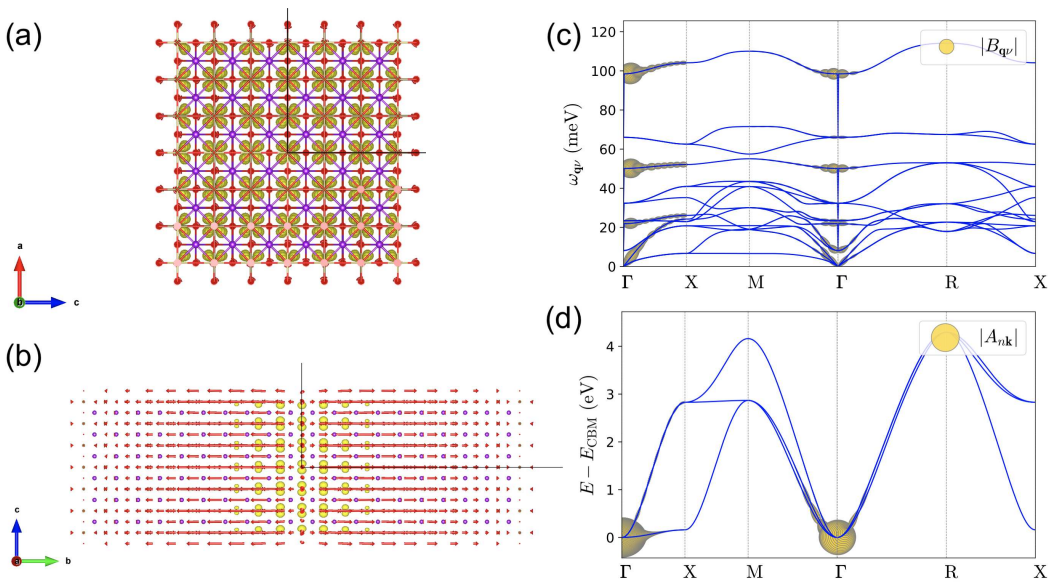


Figure 8.2. Large electron polaron features in $KTaO_3$. (a,b) Before complete localization, if a supercell size smaller than 30×30×30 is considered, the electron polaron is confined in one direction while being delocalized along the other two axes. The (c) $B_{\mathbf{q}\nu}$ and (d) $A_{\mathbf{k}m}$ coefficients are plotted, respectively, over the phonon dispersion and electronic bandstructure as yellow circles. The radii of the circles are proportional to the value of the coefficients.

Intuitively, the localization of a charge carrier is associated to "band narrowing" in reciprocal space, thus an increased opportunity for scattering events with phonons. From a similar perspective, band narrowing is associated to a higher carrier effective mass, with respect to the free carrier. Introducing SOC in $KTaO_3$ is computationally very expensive, especially for supercells larger than 30×30×30. From our preliminary calculations, the convergence behavior of the formation energy appears analogous to the one without SOC shown in Figure 8.1a, but no conclusions can be drawn on the effect of SOC.

We also performed preliminary calculations for the electron polaron in FE $KTaO_3$ at 1% strain. From these calculations, we conclude that the electron polaron in strained FE $KTaO_3$ is similar to the case of unstrained $KTaO_3$. These observations are in line with the observation of a prominent long-range electron phonon interaction, which couples electrons and phonons in close proximity of the Γ-point. Indeed, the phonon dispersions and conduction bands of FE and PE $KTaO_3$ are similar near the Γ-point, while being generally different in the rest of the BZ.

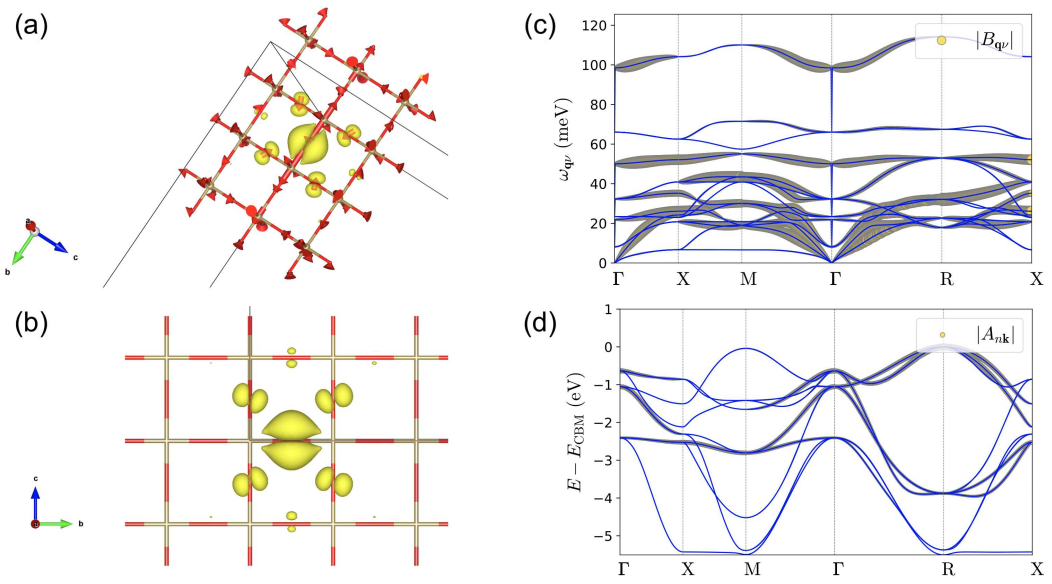


Figure 8.3. (a,b) View of the small hole polaron wavefunction in $KTaO_3$. The (c) $B_{\mathbf{q}\nu}$ and (d) $A_{\mathbf{k}m}$ coefficients are plotted, respectively, over the phonon dispersion and electronic bandstructure as yellow circles. The radii of the circles are proportional to the value of the coefficients.

8.2.2 Hole Polaron

In the case of hole doping, $KTaO_3$ and $SrTiO_3$ develop a small hole polaron. The formation energy in $SrTiO_3$ is lower than in the case of $KTaO_3$, as shown in Figure 8.1b. This marked difference, not seen for the electron polaron, can be explained by observing the distribution of the $A_{n\mathbf{k}}$ and $B_{\mathbf{q}\nu}$ coefficients in reciprocal space, shown in Figure 8.3(c-d). The coefficients are widely distributed both in the reciprocal space and on the phonon branches. This means that the small polaron formation energy is more susceptible to fine differences in the vibrational and electronic spectra of the two materials, throughout the whole BZ. In the case of the large electron polaron, on the other hand, the long-range features around the Γ point dominate.

Preliminary results for PE $KTaO_3$ suggest that the hole formation energy is affected very little by the inclusion of SOC, as shown in Figure 8.4. Not surprisingly, the hole polaron in FE $KTaO_3$ has a lower formation energy than observed in the PE phase. The small polaron is indeed more susceptible of small differences in the vibrational behavior and UC volume, even at uniaxial strains as small as 1% of the cubic lattice vector. The differing hole polaron formation energies in $KTaO_3$ compared to $SrTiO_3$, and in PE $KTaO_3$ compared to FE $KTaO_3$,

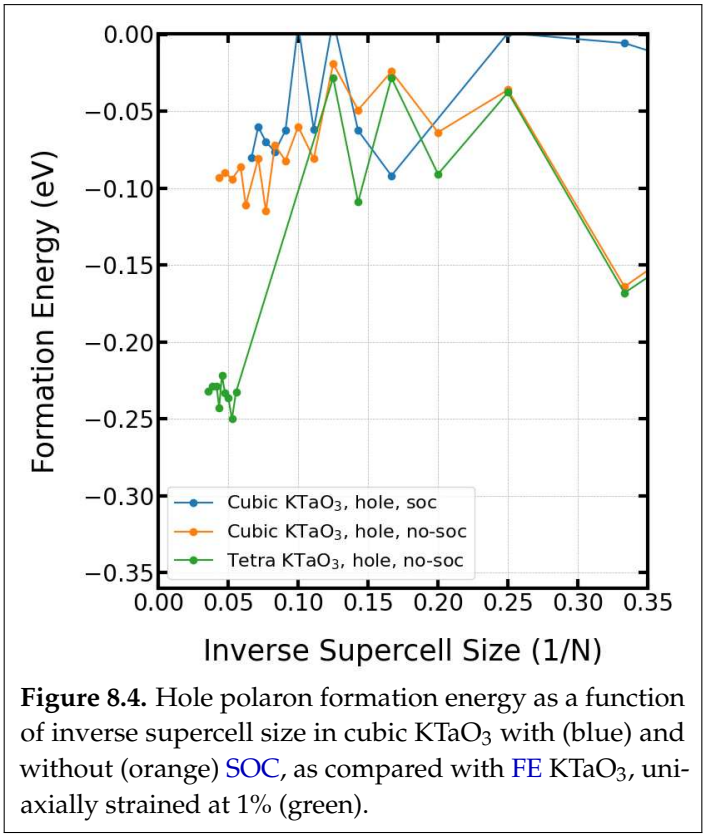


Figure 8.4. Hole polaron formation energy as a function of inverse supercell size in cubic $KTaO_3$ with (blue) and without (orange) SOC, as compared with FE $KTaO_3$, uniaxially strained at 1% (green).

ultimately highlight the importance of accurately modeling lattice dynamics when modeling small of polarons.

CHAPTER 9

Summary and Outlook

9.1 Summary

In this dissertation we investigated the phenomenon of phonon anharmonicity from first principles and with the aid of machine-learned force fields, in order to offer a computational scheme that is efficient, accurate, applicable to any compound, and easy to be powered by any other energy/force engine (Chapter 3). In particular, we have described the QPE state in $KTaO_3$ in terms of the softening of the TO mode. We have shown how phonon anharmonicity can be seamlessly integrated in the calculation of renormalized electron-phonon matrix elements (Chapter 5), thus offering reliable results for carrier mobilities (Chapter 7) and polaron localization (Chapter 8). Furthemore, we have shown how the "special displacements method", a supercell-based approach can be adopted starting from anharmonic rather than harmonic dynamical matrices. This generates more accurate estimates of the temperature-dependent bandgap renormalization in diamond (Chapter 6) and non trivial conduction band eigenvalue renormalization in $KTaO_3$ and $SrTiO_3$.

In particular, we explain the mechanism behind the anharmonically mediated QPE state in $KTaO_3$ and $SrTiO_3$, and their FE and AFD phase transitions with varying external forcings and different temperatures (Chapter 4). We show that the integration of phonon anharmonicity does not dramatically affect electron mobility in both compounds. However, it makes robust calculations possible through the estimate of well defined, stable phonons which match the

experiment, avoiding the introduction of ad-hoc cutoff frequencies to eliminate spurious divergencies arising from the unstable phonon modes. We also estimate the effect of $SrTiO_3$ lattice disorder on the electron mobility, by interpolating the unfolded band structure of the disordered supercell to integrate it in the BTE. Finally, we show how taking into account $SrTiO_3$ lattice disorder and the electron-phonon renormalization of the carrier effective masses in both $KTaO_3$ and $SrTiO_3$ through anharmonic ZG displacements, we obtain electron mobilities which overestimate the respective experimental values of around 300%, thus establishing a stark similarity between the two compounds (Chapter 5).

At this point, we show how both materials can host large electron polarons of comparable formation energies, thus hinting at a possible polaronic regime for electronic transport, which would explain the mobility overestimation obtained through the BTE. The large polaron localization is to be attributed to the electrons at the conduction band bottom near Γ, and mostly by long-range LO phonons. Furthermore, we showed how both compounds can host small hole polarons with different formation energies. The more favorable formation energy seems to be attributed to the fact that the electron-phonon interaction covers the whole Brillouine one, instead of being strongly localized as in the large electron polaron case. Fine-grain differences in the vibrational and electronic properties of the O_p orbitals of $KTaO_3$ and $SrTiO_3$ have thus a remarkable effect in the small polaron localization (Chapter 8).

9.2 Outlook

We trust that the work presented in this thesis has shown the possibility of an affordable and accurate modeling of phonon anharmonicity, and its implementation in electron-phonon calculations. The workflow devised for the integration of MLFF in the SSCHA has indeed been already extended to other oxide perovskites [160]. Another interesting line of research that could benefit from our approach is the modeling anharmonic effects in hydrogen-based superconductors [161–163], which has gathered notable interest in recent years. The use of MLFFs can indeed be beneficial for molecular dynamics simulations, as we

proved in a recent paper on superconductivity LuH_3 [164].

The advent of MLFF and neural networks for ground state energy predictions has generated a great interest in the search of novel functional compounds, in order to inform experimentalists on viable candidates for synthesis, and to draw correlations between compound similarities and properties of interest [20, 165–167]. Usually, these massively automatized searches are limited to the HA approximation, while we now understand how important quantum effects and anharmonic lattice dynamics are in predicting compound stability. We want to point out here that our workflow is particularly suitable for such high-throughput searches, since it is fully automated with the use of ASE [134].

Finally, we hope that our deep analysis of electron mobility and charge carrier localization in $KTaO_3$ and $SrTiO_3$ via the combined calculation of polaronic ground states and BTE shines a light on the deep similarities in these two materials and that it could offer a strategy for deducing the occurrence of a polaronic transport regime in novel materials, with the addition of anharmonic lattice dynamics both in the ZG displacements algorithm and in the electron-phonon coupling elements. On a final note, our work calls for affordable methods for estimating the intensity of the electron-phonon interactions beyond the linear order [168–170], to be numerically compared with the complete calculations offered in this dissertation.

Bibliography

[1] M. Born and R. Oppenheimer, Annalen der Physik **389**, 457 (1927).

[2] P. Hohenberg and W. Kohn, Phys. Rev. **136**, B864 (1964).

[3] W. Kohn and L. J. Sham, Phys. Rev. **140**, A1133 (1965).

[4] H. Hellman, Einführung in die Quantenchemie. Deuticke, Leipzig (1937).

[5] R. P. Feynman, Phys. Rev. **56**, 340 (1939).

[6] M. Born and K. Huang, Dynamical Theory of Crystal Lattices (1954).

[7] R. M. Pick, M. H. Cohen, and R. M. Martin, Phys. Rev. B **1**, 910 (1970).

[8] S. Baroni, S. D. Gironcoli, A. D. Corso, and P. Giannozzi, Rev. Mod. Phys. **73**, 515 (2001).

[9] K. Parlinski, Z. Q. Li, and Y. Kawazoe, Phys. Rev. Lett. **78**, 4063 (1997).

[10] J. H. Lloyd-Williams and B. Monserrat, Phys. Rev. B **92**, 184301 (2015).

[11] P. Giannozzi, S. de Gironcoli, P. Pavone, and S. Baroni, Phys. Rev. B **43**, 7231 (1991).

[12] X. Gonze, J.-C. Charlier, D. Allan, and M. Teter, Phys. Rev. B **50**, 13035 (1994).

[13] X. Gonze and C. Lee, Phys. Rev. B **55**, 10355 (1997).

[14] L. Monacelli, R. Bianco, M. Cherubini, M. Calandra, I. Errea, and F. Mauri, J. Condens. Matter Phys **33**, 363001 (2021).

[15] I. Errea, M. Calandra, and F. Mauri, Phys. Rev. Lett. **111**, 177002 (2013).

[16] I. Errea, M. Calandra, and F. Mauri, Phys. Rev. B **89**, 064302 (2014).

[17] R. Bianco, I. Errea, L. Paulatto, M. Calandra, and F. Mauri, Phys. Rev. B **96**, 014111 (2017).

[18] L. Monacelli, I. Errea, M. Calandra, and F. Mauri, Phys. Rev. B **98**, 024106 (2018).

[19] A. Isihara, J. Phys. A: Gen. Phys. **1**, 539 (1968).

[20] J. Schmidt, M. R. G. Marques, S. Botti, and M. A. L. Marques, npj Computational Materials **5**, 83 (2019).

[21] V. L. Deringer, M. A. Caro, and G. Csányi, Advanced Materials **31**, 1902765 (2019).

[22] O. T. Unke, S. Chmiela, H. E. Sauceda, M. Gastegger, I. Poltavsky, K. T. Schütt, A. Tkatchenko, and K.-R. Müller, Chemical Reviews **121**, 10142 (2021).

[23] R. Jinnouchi, J. Lahnsteiner, F. Karsai, G. Kresse, and M. Bokdam, Phys. Rev. Lett. **122**, 225701 (2019).

[24] R. Jinnouchi, F. Karsai, and G. Kresse, Phys. Rev. B **100**, 014105 (2019).

[25] R. Jinnouchi, F. Karsai, C. Verdi, R. Asahi, and G. Kresse, The Journal of Chemical Physics **152**, 234102 (2020).

[26] L. Ranalli, C. Verdi, L. Monacelli, G. Kresse, M. Calandra, and C. Franchini, Adv. Quantum Technol. **6**, 2200131 (2023).

[27] C. Verdi, L. Ranalli, C. Franchini, and G. Kresse, Phys. Rev. Mater. **7**, L030801 (2023).

[28] R. A. Cowley, Phys. Rev. Lett. **9**, 159 (1962).

[29] R. Migoni, H. Bilz, and D. Bäuerle, Phys. Rev. Lett. **37**, 1155 (1976).

[30] G. V. Belokopytov, Ferroelectrics **168**, 69 (1995).

[31] F. Hideshi, K. Shou, S. Masahiro, I. Ryosuke, O. Hiroyuki, and Y. Toshihisa, Journal of the Physical Society of Japan **85**, 74703 (2016).

[32] S. E. Rowley, L. J. Spalek, R. P. Smith, M. P. M. Dean, M. Itoh, J. F. Scott, G. G. Lonzarich, and S. S. Saxena, Nat. Phys. **10**, 367 (2014).

[33] S. Sachdev, *Quantum Phase Transitions* (Cambridge University Press, 2000).

[34] M. Tyunina, J. Narkilahti, M. Plekh, R. Oja, R. M. Nieminen, A. Dejneka, and V. Trepakov, Phys. Rev. Lett. **104**, 227601 (2010).

[35] G. A. Samara, Phys. Rev. **151**, 378 (1966).

[36] H. Uwe and T. Sakudo, Phys. Rev. B **13**, 271 (1976).

[37] M. Itoh, R. Wang, Y. Inaguma, T. Yamaguchi, Y.-J. Shan, and T. Nakamura, Phys. Rev. Lett. **82**, 3540 (1999).

[38] T. Esswein and N. A. Spaldin, Phys. Rev. Research **4**, 033020 (2022).

[39] J. H. Barrett, Phys. Rev. **86**, 118 (1952).

[40] W. Cochran, Advances in Physics **9**, 387 (1960).

[41] G. A. Samara and B. Morosin, Phys. Rev. B **8**, 1256 (1973).

[42] R. P. Lowndes and A. Rastogi, Journal of Physics C: Solid State Physics **6**, 932 (1973).

[43] C. H. Perry, R. Currat, H. Buhay, R. M. Migoni, W. G. Stirling, and J. D. Axe, Phys. Rev. B **39**, 8666 (1989).

[44] J. C. Slater, Phys. Rev. **78**, 748 (1950).

[45] O. G. Vendik, Sov. Phys. Solid State **14**, 849 (1972).

[46] A. B. Rechester, Sov. Phys. JETP **33**, 423 (1971).

[47] D. E. Khmelnitskii and V. L. Shneerson, Sov. Phys. JETP **37**, 164 (1973).

[48] R. Martoňák and E. Tosatti, Phys. Rev. B **49**, 12596 (1994).

[49] W. Zhong and D. Vanderbilt, Phys. Rev. B **53**, 5047 (1996).

[50] R. Martoňák and E. Tosatti, Phys. Rev. B **54**, 15714 (1996).

[51] O. Hellman, I. A. Abrikosov, and S. I. Simak, Physical Review B - Condensed Matter and Materials Physics **84**, 180301 (2011).

[52] W. G. Hoover, A. J. C. Ladd, and B. Moran, Phys. Rev. Lett. **48**, 1818 (1982).

[53] G. Kresse and J. Hafner, Phys. Rev. B **47**, 558 (1993).

[54] G. Kresse and J. Furthmüller, Phys. Rev. B **54**, 11169 (1996).

[55] A. Togo *et al.*, Journal of Physics: Condensed Matter **35**, 353001 (2023).

[56] A. Togo, Journal of the Physical Society of Japan **92**, 012001 (2023).

[57] J. Sun, A. Ruzsinszky, and J. Perdew, Phys. Rev. Lett. **115**, 036402 (2015).

[58] G. Kresse and D. Joubert, Phys. Rev. B **59**, 1758 (1999).

[59] H. Vogt, Phys. Rev. B **51**, 8046 (1995).

[60] R. H. Lyddane, R. G. Sachs, and E. Teller, Phys. Rev. **59**, 673 (1941).

[61] G. D. Mahan, *Many-Particle Physics*, 2nd ed. (Plenum, New York, 1993).

[62] G. H. Wannier, Phys. Rev. **52**, 191 (1937).

[63] N. Marzari and D. Vanderbilt, Phys. Rev. B **56**, 12847 (1997).

[64] J. Ziman, Oxford University Press (1960).

[65] F. Giustino, Rev. Mod. Phys. **89**, 015003 (2017).

[66] P. B. Allen and M. Cardona, Phys. Rev. B **23**, 1495 (1981).

[67] M. Zacharias and F. Giustino, Phys. Rev. B **94**, 075125 (2016).

[68] M. Zacharias and F. Giustino, Phys. Rev. Res. **2**, 13357 (2020).

[69] W. H. Sio, C. Verdi, S. Poncé, and F. Giustino, Phys. Rev. Lett. **122**, 246403 (2019).

[70] W. H. Sio, C. Verdi, S. Poncé, and F. Giustino, Phys. Rev. B **99**, 235139 (2019).

[71] F. Karsai, M. Engel, E. Flage-Larsen, and G. Kresse, New Journal of Physics **20**, 123008 (2018).

[72] J. P. Perdew, K. Burke, and M. Ernzerhof, Phys. Rev. Lett. **78**, 1396 (1997).

[73] A. Togo, F. Oba, and I. Tanaka, Phys. Rev. B **78**, 134106 (2008).

[74] P. Jacobson and S. Stoupin, Diam. Relat. Mater. **97**, 107469 (2019).

[75] S. Stoupin and Y. V. Shvyd'ko, Phys. Rev. Lett. **104**, 085901 (2010).

[76] K. P. O'Donnell and X. Chen, Applied Physics Letters **58**, 2924 (1991).

[77] L. Ranalli, C. Verdi, M. Zacharias, J. Even, F. Giustino, and C. Franchini, Phys. Rev. Mater. **8**, 104603 (2024).

[78] J. G. Bednorz and K. A. Müller, Rev. Mod. Phys. **60**, 585 (1988).

[79] N. Reyren, S. Thiel, A. D. Caviglia, L. F. Kourkoutis, G. Hammerl, C. Richter, C. W. Schneider, T. Kopp, A. S. Rüetschi, D. Jaccard, M. Gabay, D. A. Muller, J. M. Triscone, and J. Mannhart, Science **317**, 1196 (2007).

[80] S. Jin, T. H. Tiefel, M. McCormack, R. A. Fastnacht, R. Ramesh, and L. H. Chen, Science **264**, 413 (1994).

[81] R. E. Cohen, Nature **358**, 136 (1992).

[82] J.-M. L. K.F. Wang and Z. Ren, Adv. Phys. **58**, 321 (2009).

[83] A. Narayan, A. Cano, A. V. Balatsky, and N. A. Spaldin, Nat. Mat. **18**, 223 (2018).

[84] F. Li, D. Lin, Z. Chen, Z. Cheng, J. Wang, C. Li, Z. Xu, Q. Huang, X. Liao, L. Q. Chen, T. R. Shrout, and S. Zhang, Nat. Mater. **17**, 349 (2018).

[85] M. Imada, A. Fujimori, and Y. Tokura, Rev. Mod. Phys. **70**, 1039 (1998).

[86] J. He and C. Franchini, Phys. Rev. B **86**, 235117 (2012).

[87] Z. Ergönenc, B. Kim, P. Liu, G. Kresse, and C. Franchini, Phys. Rev. Mater. **2**, 024601 (2018).

[88] L. Varrassi, P. Liu, Z. E. Yavas, M. Bokdam, G. Kresse, and C. Franchini, Phys. Rev. Mater. **5**, 074601 (2021).

[89] C.-Y. Liu, L. Celiberti, R. Decker, K. Ruotsalainen, K. Siewierska, M. Kusch, R.-P. Wang, D. J. Kim, I. I. Olaniyan, D. Di Castro, K. Tomiyasu, E. van der Minne, Y. A. Birkhölzer, E. M. Kiens, I. C. G. van den Bosch, K. N. Patil, C. Baeumer, G. Koster, M. Lazemi, F. M. F. de Groot, C. Dubourdieu, C. Franchini, and A. Föhlisch, Commun. Phys. **7**, 156 (2024).

[90] M. G.-V. Fatih Dogan, Hong Lin and O. Peña, Sci. Technol. Adv. Mater. **16**, 020301 (2015).

[91] A. Sawa, Mater. Today **11**, 28 (2008).

[92] B. Sun, G. Zhou, L. Sun, H. Zhao, Y. Chen, F. Yang, Y. Zhao, and Q. Song, Nanoscale Horiz **6**, 939 (2021).

[93] M. Kim, J. Im, A. J. Freeman, J. Ihm, and H. Jin, Proc. Natl. Acad. Sci. U. S. A. **111**, 6900 (2014).

[94] J. Suntivich, H. A. Gasteiger, N. Yabuuchi, H. Nakanishi, J. B. Goodenough, and Y. Shao-Horn, Nat. Chem. **3**, 546 (2011).

[95] S. Poncé, E. R. Margine, and F. Giustino, Phys. Rev. B **97**, 121201 (2018).

[96] N. H. Protik and D. A. Broido, Phys. Rev. B **101**, 075202 (2020).

[97] J. Park, J.-J. Zhou, V. A. Jhalani, C. E. Dreyer, and M. Bernardi, Phys. Rev. B **102**, 125203 (2020).

[98] J. J. Zhou, J. Park, I. T. Lu, I. Maliyov, X. Tong, and M. Bernardi, Comput. Phys. Commun. **264**, 107970 (2021).

[99] X. Gonze, B. Amadon, G. Antonius, F. Arnardi, L. Baguet, J. M. Beuken, J. Bieder, F. Bottin, J. Bouchet, E. Bousquet, N. Brouwer, F. Bruneval, G. Brunin, T. Cavignac, J. B. Charraud, W. Chen, M. Côté, S. Cottenier, J. Denier, G. Geneste, P. Ghosez, M. Giantomassi, Y. Gillet, O. Gingras, D. R. Hamann, G. Hautier, X. He, N. Helbig, N. Holzwarth, Y. Jia, F. Jollet, W. Lafargue-Dit-Hauret, K. Lejaeghere, M. A. Marques, A. Martin,

C. Martins, H. P. Miranda, F. Naccarato, K. Persson, G. Petretto, V. Planes, Y. Pouillon, S. Prokhorenko, F. Ricci, G. M. Rignanese, A. H. Romero, M. M. Schmitt, M. Torrent, M. J. van Setten, B. V. Troeye, M. J. Verstraete, G. Zérah, and J. W. Zwanziger, Comput. Phys. Comm. **248**, 107042 (2020).

[100] O. D. Restrepo, K. Varga, and S. T. Pantelides, Appl. Phys. Lett. **94**, 212103 (2009).

[101] J.-J. Zhou and M. Bernardi, Phys. Rev. B **94**, 201201 (2016).

[102] Y. Zhao, C. Lian, S. Zeng, Z. Dai, S. Meng, and J. Ni, Phys. Rev. B **102**, 094314 (2020).

[103] N. H. Protik and B. Kozinsky, Phys. Rev. B **102**, 245202 (2020).

[104] S. Poncé, D. Jena, and F. Giustino, Phys. Rev. B **100**, 085204 (2019).

[105] S. Poncé, D. Jena, and F. Giustino, Phys. Rev. Lett. **123**, 096602 (2019).

[106] S. Poncé and F. Giustino, Phys. Rev. Res. **2**, 033102 (2020).

[107] S. Poncé, W. Li, S. Reichardt, and F. Giustino, Rep. Prog. Phys. **83**, 036501 (2020).

[108] S. Poncé, F. Macheda, E. R. Margine, N. Marzari, N. Bonini, and F. Giustino, Phys. Rev. Res. **3**, 043022 (2021).

[109] F. Macheda and N. Bonini, Phys. Rev. B **98**, 201201 (2018).

[110] J. Ma, A. S. Nissimagoudar, and W. Li, Phys. Rev. B **97**, 045201 (2018).

[111] J. Ma, Y. Chen, and W. Li, Phys. Rev. B **97**, 205207 (2018).

[112] T.-H. Liu, J. Zhou, B. Liao, D. J. Singh, and G. Chen, Phys. Rev. B **95**, 075206 (2017).

[113] T.-H. Liu, B. Song, L. Meroueh, Z. Ding, Q. Song, J. Zhou, M. Li, and G. Chen, Phys. Rev. B **98**, 081203 (2018).

[114] W. Li, Phys. Rev. B **92**, 075405 (2015).

[115] N.-E. Lee, J.-J. Zhou, L. A. Agapito, and M. Bernardi, Phys. Rev. B **97**, 115203 (2018).

[116] N. E. Lee, J. J. Zhou, H. Y. Chen, and M. Bernardi, Nat. Commun. **11**, 1 (2020).

[117] Y. Kang, H. Peelaers, and C. G. Van de Walle, Phys. Rev. B **100**, 121113 (2019).

[118] V. A. Jhalani, J.-J. Zhou, J. Park, C. E. Dreyer, and M. Bernardi, Phys. Rev. Lett. **125**, 136602 (2020).

[119] J. Cao, J. D. Querales-Flores, A. R. Murphy, S. Fahy, and I. Savić, Phys. Rev. B **98**, 205202 (2018).

[120] G. Brunin, H. P. C. Miranda, M. Giantomassi, M. Royo, M. Stengel, M. J. Verstraete, X. Gonze, G.-M. Rignanese, and G. Hautier, Phys. Rev. B **102**, 094308 (2020).

[121] J. J. Zhou, O. Hellman, and M. Bernardi, Phys. Rev. Lett. **121**, 226603 (2018).

[122] J. J. Zhou and M. Bernardi, Phys. Rev. Res. **1**, 033138 (2019).

[123] J. Ma, W. Li, and X. Luo, Phys. Rev. B **106**, 045201 (2022).

[124] Q. Wang, C. Wang, C. Chi, N. Ouyang, R. Guo, N. Yang, and Y. Chen, Phys. Rev. B **108**, 115435 (2023).

[125] C. Shen, M. Dai, X. Xiao, N. Hadaeghi, W. Xie, A. Weidenkaff, T. Tadano, and H. Zhang, Mater. Today Phys. **34**, 101059 (2023).

[126] Z. Wang, S. M. Walker, A. Tamai, Y. Wang, Z. Ristic, F. Y. Bruno, A. D. L. Torre, S. Riccò, N. C. Plumb, M. Shi, P. Hlawenka, J. Sánchez-Barriga, A. Varykhalov, T. K. Kim, M. Hoesch, P. D. King, W. Meevasana, U. Diebold, J. Mesot, B. Moritz, T. P. Devereaux, M. Radovic, and F. Baumberger, Nat. Mater. **15**, 835 (2016).

[127] J. L. M. van Mechelen, D. van der Marel, C. Grimaldi, A. B. Kuzmenko, N. P. Armitage, N. Reyren, H. Hagemann, and I. I. Mazin, Phys. Rev. Lett. **100**, 226403 (2008).

[128] S. Klimin, J. Tempere, J. T. Devreese, C. Franchini, and G. Kresse, Applied Sciences **10** (2020), 10.3390/app10062059.

[129] A. F. Santander-Syro, C. Bareille, F. Fortuna, O. Copie, M. Gabay, F. Bertran, A. Taleb-Ibrahimi, P. Le Fèvre, G. Herranz, N. Reyren, M. Bibes, A. Barthélémy, P. Lecoeur, J. Guevara, and M. J. Rozenberg, Phys. Rev. B **86**, 121107 (2012).

[130] T. A. Cain, A. P. Kajdos, and S. Stemmer, Appl. Phys. Lett. **102**, 182101 (2013).

[131] S. H. Wemple, Phys. Rev. **137**, A1575 (1965).

[132] D. Hooton, London Edinburgh Philos. Mag. & J. Sci. **46**, 422 (1955).

[133] M. Zacharias, G. Volonakis, F. Giustino, and J. Even, Npj Comput. Mater. **9**, 1 (2023).

[134] A. H. Larsen, J. J. Mortensen, J. Blomqvist, I. E. Castelli, R. Christensen, M. Dułak, J. Friis, M. N. Groves, B. Hammer, C. Hargus, E. D. Hermes, P. C. Jennings, P. B. Jensen, J. Kermode, J. R. Kitchin, E. L. Kolsbjerg, J. Kubal, K. Kaasbjerg, S. Lysgaard, J. B. Maronsson, T. Maxson, T. Olsen, L. Pastewka, A. Peterson, C. Rostgaard, J. Schiøtz, O. Schütt, M. Strange, K. S. Thygesen, T. Vegge, L. Vilhelmsen, M. Walter, Z. Zeng, and K. W. Jacobsen, J. Condens. Matter Phys. **29**, 273002 (2017).

[135] S. Poncé, E. R. Margine, C. Verdi, and F. Giustino, Comput. Phys. Commun. **209**, 116 (2016).

[136] F. Giustino, M. L. Cohen, and S. G. Louie, Phys. Rev. B **76**, 165108 (2007).

[137] C. Verdi and F. Giustino, Phys. Rev. Lett. **115**, 176401 (2015).

[138] H. Lee, S. Poncé, K. Bushick, S. Hajinazar, J. Lafuente-Bartolome, J. Leveillee, C. Lian, J. M. Lihm, F. Macheda, H. Mori, H. Paudyal, W. H. Sio,

S. Tiwari, M. Zacharias, X. Zhang, N. Bonini, E. Kioupakis, E. R. Margine, and F. Giustino, Npj Comput. Mater. **9**, 1 (2023).

[139] P. Giannozzi, S. Baroni, N. Bonini, M. Calandra, R. Car, C. Cavazzoni, D. Ceresoli, G. L. Chiarotti, M. Cococcioni, I. Dabo, A. D. Corso, S. de Gironcoli, S. Fabris, G. Fratesi, R. Gebauer, U. Gerstmann, C. Gougoussis, A. Kokalj, M. Lazzeri, L. Martin-Samos, N. Marzari, F. Mauri, R. Mazzarello, S. Paolini, A. Pasquarello, L. Paulatto, C. Sbraccia, S. Scandolo, G. Sclauzero, A. P. Seitsonen, A. Smogunov, P. Umari, and R. M. Wentzcovitch, J. Phys.: Condens. Matter **21**, 395502 (2009).

[140] P. Giannozzi, O. Andreussi, T. Brumme, O. Bunau, M. B. Nardelli, M. Calandra, R. Car, C. Cavazzoni, D. Ceresoli, M. Cococcioni, N. Colonna, I. Carnimeo, A. D. Corso, S. de Gironcoli, P. Delugas, R. A. DiStasio, A. Ferretti, A. Floris, G. Fratesi, G. Fugallo, R. Gebauer, U. Gerstmann, F. Giustino, T. Gorni, J. Jia, M. Kawamura, H.-Y. Ko, A. Kokalj, E. Küçükbenli, M. Lazzeri, M. Marsili, N. Marzari, F. Mauri, N. L. Nguyen, H.-V. Nguyen, A. O. de-la Roza, L. Paulatto, S. Poncé, D. Rocca, R. Sabatini, B. Santra, M. Schlipf, A. P. Seitsonen, A. Smogunov, I. Timrov, T. Thonhauser, P. Umari, N. Vast, X. Wu, and S. Baroni, J. Phys.: Condens. Matter **29**, 465901 (2017).

[141] G. Pizzi, V. Vitale, R. Arita, S. Blügel, F. Freimuth, G. Géranton, M. Gibertini, D. Gresch, C. Johnson, T. Koretsune, J. Ibañez-Azpiroz, H. Lee, J.-M. Lihm, D. Marchand, A. Marrazzo, Y. Mokrousov, J. I. Mustafa, Y. Nohara, Y. Nomura, L. Paulatto, S. Poncé, T. Ponweiser, J. Qiao, F. Thöle, S. S. Tsirkin, M. Wierzbowska, N. Marzari, D. Vanderbilt, I. Souza, A. A. Mostofi, and J. R. Yates, J. Condens. Matter Phys. **32**, 165902 (2020).

[142] D. R. Hamann, Phys. Rev. B **88**, 85117 (2013).

[143] X.-G. Zhao, G. M. Dalpian, Z. Wang, and A. Zunger, Phys. Rev. B **101**, 155137 (2020).

[144] M. Zacharias, G. Volonakis, F. Giustino, and J. Even, Phys. Rev. B **108**, 035155 (2023).

[145] V. Popescu and A. Zunger, Phys. Rev. B **85**, 085201 (2012).

[146] J. L. Servoin, Y. Luspin, and F. Gervais, Phys. Rev. B **22**, 5501 (1980).

[147] W. G. Stirling, J. Phys. C: Solid State Phys. **5**, 2711 (1972).

[148] S. Poncé, M. Schlipf, and F. Giustino, ACS Energy Lett. **4**, 456 (2019).

[149] B. Himmetoglu and A. Janotti, J. Condens. Matter Phys. **28**, 065502 (2016).

[150] A. Janotti, D. Steiauf, and C. G. V. D. Walle, Phys. Rev. B **84**, 201304 (2011).

[151] L. Merker, F. M. Plock, S. B. Levin, and N. J. Field, J. Opt. Soc. Am. **45**, 737 (1955).

[152] C. H. Perry, J. H. Fertel, and T. F. McNelly, J. Chem. Phys **47**, 1619 (1967).

[153] Y. Fujii and T. Sakudo, J. Phys. Soc. Jpn. **41**, 888 (1976).

[154] L. D. Landau, Phys. Z. Sowjet. **3**, 664 (1933).

[155] L. Landau and S. Pekar, Zh. Eksp. Teor. Fiz **18**, 419 (1948).

[156] S. Pekar, Zh. Eksp. Teor. Fiz **16**, 335 (1946).

[157] H. Fröhlich, Adv. Phys. **3**, 325 (1954).

[158] C. Franchini, M. Reticcioli, M. Setvin, and U. Diebold, Nat. Rev. Mat. (2021), 10.1038/s41578-021-00289-w.

[159] M. Reticcioli, U. Diebold, and C. Franchini, J. Condens. Matter Phys. **34** (2022), 10.1088/1361-648X/ac58d7.

[160] F. Bernhardt, L. M. Verhoff, N. A. Schäfer, A. Kapp, C. Fink, W. A. Nachwati, U. Bashir, D. Klimm, F. E. Azzouzi, U. Yakhnevych, Y. Suhak, H. Schmidt, K.-D. Becker, S. Ganschow, H. Fritze, and S. Sanna, Phys. Rev. Mater. **8**, 054406 (2024).

[161] Dangić, L. Monacelli, and R. e. a. Bianco, Commun Phys **7**, 150 (2024).

[162] I. Errea, M. Calandra, and F. Mauri, physica status solidi (b) **251**, 2556 (2014).

[163] I. Errea, F. Belli, and L. e. a. Monacelli, Nature **578**, 66 (2020).

[164] C. Tresca, P. M. Forcella, A. Angeletti, L. Ranalli, C. Franchini, M. Reticcioli, and G. Profeta, Nat. Commun. **15**, 7283 (2024).

[165] Y. Zhang, D. A. Kitchaev, J. Yang, T. Chen, S. T. Dacek, R. A. Sarmiento-Pérez, M. A. L. Marques, H. Peng, G. Ceder, J. P. Perdew, and J. Sun, npj Computational Materials **4**, 9 (2018).

[166] J. Schmidt, H.-C. Wang, T. F. T. Cerqueira, S. Botti, and M. A. L. Marques, Scientific Data **9**, 64 (2022).

[167] J. Schmidt, J. Shi, P. Borlido, L. Chen, S. Botti, and M. A. L. Marques, Chemistry of Materials **29**, 5090 (2017).

[168] S. Ragni, T. Hahn, Z. Zhang, N. Prokof'ev, A. Kuklov, S. Klimin, M. Houtput, B. Svistunov, J. Tempere, N. Nagaosa, C. Franchini, and A. S. Mishchenko, Phys. Rev. B **107**, L121109 (2023).

[169] M. Houtput, L. Ranalli, C. Verdi, S. Klimin, S. Ragni, C. Franchini, and J. Tempere, (2024), arXiv:2412.09470 [cond-mat.mtrl-sci] .

[170] M. Houtput, L. Ranalli, C. Verdi, S. Klimin, S. Ragni, J. Tempere, and C. Franchini, (2024), arXiv:2412.09456 [cond-mat.mtrl-sci] .

List Of Publications

Publications reported and discussed in this thesis:

1. **L. Ranalli**, C. Verdi, L. Monacelli, G. Kresse, M. Calendra, C. Franchini, "Temperature Dependent Anharmonic Phonons in Quantum Paraelectric $KTaO_3$ by First Principles and Machine Learned Force-Fields". Advanced Quantum Technologies, Advanced Quantum Technologies, 6, 2200131 (2023)

2. **L. Ranalli**, C. Verdi, M. Zacharias, J. Even, F. Giustino, C. Franchini, "Electron Mobilities in $SrTiO_3$ and $KTaO_3$: Role of Phonon Anharmonicity, Mass Renormalization and Disorder", Physical Review Materials, 8, 104603 (2024)

3. C. Verdi, **L. Ranalli**, C. Franchini, G. Kresse "Quantum paraelectricity and structural phase transitions in strontium titanate beyond density functional theory", Physical Review Materials, 7, L030801 (2024)

Publications not reported in this thesis:

4. M. Houtput, **L. Ranalli**, C. Verdi, S. Klimin, S. Ragni, J. Tempere, C. Franchini, "Anharmonic long-range electron-phonon interaction: analytic formalism", arXiv:2412.09456 (2025)

5. M. Houtput, **L. Ranalli**, C. Verdi, S. Klimin, S. Ragni, J. Tempere, C. Franchini, "First-principles theory of nonlinear long-range electron-phonon interaction", arXiv:2412.09470 (2025)

6. C. Tresca, P. M. Forcella, A. Angeletti, **L. Ranalli**, C. Franchini, M. Reticcioli, G. Profeta. "Evidence of Molecular Hydrogen in the N-doped LuH3 System: a Possible Path to Superconductivity?", Nature Communications 15, 7283 (2024)